REPORT DOCUMENTATION PAGE

Form Approved OMB NO. 0704-0188

1. REPORT DATE (DD-MM-YYYY)	2. REPORT TYPE	3. DATES COVERED (From - To)
31-08-2007	Final Report	1-May-2003 - 31-May-2007

4. TITLE AND SUBTITLE
Experimental Analysis of the Vorticity and Turbulent Flow Dynamics of a Pitching Airfoil at Realistic Flight Conditions

5a. CONTRACT NUMBER
DAAD19-03-1-0045

5b. GRANT NUMBER

5c. PROGRAM ELEMENT NUMBER
611102

6. AUTHORS
Rodney D. W. Bowersox, Dipankar Sahoo

5d. PROJECT NUMBER

5e. TASK NUMBER

5f. WORK UNIT NUMBER

7. PERFORMING ORGANIZATION NAMES AND ADDRESSES
Texas A&M University-College Station
Administration Building, Room113
3578 TAMU
College Station, TX   77843   -3578

8. PERFORMING ORGANIZATION REPORT NUMBER

9. SPONSORING/MONITORING AGENCY NAME(S) AND ADDRESS(ES)
U.S. Army Research Office
P.O. Box 12211
Research Triangle Park, NC 27709-2211

10. SPONSOR/MONITOR'S ACRONYM(S)
ARO

11. SPONSOR/MONITOR'S REPORT NUMBER(S)
44371-EG.1

12. DISTRIBUTION AVAILIBILITY STATEMENT
Distribution authorized to U.S. Government Agencies Only, Contains Proprietary information

14. ABSTRACT
The primary objective of this research proposal was improved understanding of the fundamental vorticity and turbulent flow physics for a dynamically stalling airfoil at realistic helicopter flight conditions. To meet this objective, an experimental program using high-resolution particle image velocimetry was performed. High-resolution planar contours of the instantaneous and mean velocity field on a dynamically pitching NACA 0012 airfoil operating in the Texas A&M University large-scale wind tunnel are planned. For the present study, the Mach number, chord Reynolds number, and reduced frequency were selected as 0.2/0.3, 2.0/2.8x106 and 0.1/0.18, respectively. The test matrix included static attached, static

15. SUBJECT TERMS
Dynamic Stall, PIV, Vorticity, Turbulence, Leading-Edge Flow

16. SECURITY CLASSIFICATION OF:			17. LIMITATION OF ABSTRACT	15. NUMBER OF PAGES	19a. NAME OF RESPONSIBLE PERSON
a. REPORT	b. ABSTRACT	c. THIS PAGE	SAR		Rodney Bowersox
S	U	U			**19b. TELEPHONE NUMBER** 979-845-1669

Standard Form 298 (Rev 8/98)
Prescribed by ANSI Std. Z39.18

EXPERIMENTAL ANALYSIS OF THE VORTICITY AND TURBULENT FLOW DYNAMICS OF A PITCHING AIRFOIL AT REALISTIC FLIGHT CONDITIONS: FINAL PROGRESS REPORT

ABSTRACT

The primary objective of this research proposal was improved understanding of the fundamental vorticity and turbulent flow physics for a dynamically stalling airfoil at realistic helicopter flight conditions. To meet this objective, an experimental program using high-resolution particle image velocimetry was performed. High-resolution planar contours of the instantaneous and mean velocity field on a dynamically pitching NACA 0012 airfoil operating in the Texas A&M University large-scale wind tunnel are planned. For the present study, the Mach number, chord Reynolds number, and reduced frequency were selected as 0.2/0.3, 2.0/2.8x106 and 0.1/0.18, respectively. The test matrix included static attached, static stall, light dynamic stall and deep dynamic stall. The goal of these analyses was improved understanding of the dynamic stall processes at realistic flight conditions. The velocity data was processed to examine the vorticity and turbulent transport near the leading edge during stall. The data from this study are summarized in this report.

List of papers submitted or published that acknowledge ARO support during this reporting period. List the papers, including journal references, in the following categories:

(a) Papers published in peer-reviewed journals (N/A for none)

Number of Papers published in peer-reviewed journals: 0.00

(b) Papers published in non-peer-reviewed journals or in conference proceedings (N/A for none)

Number of Papers published in non peer-reviewed journals: 0.00

(c) Presentations

Number of Presentations: 0.00

Non Peer-Reviewed Conference Proceeding publications (other than abstracts):

Number of Non Peer-Reviewed Conference Proceeding publications (other than abstracts):   0

Peer-Reviewed Conference Proceeding publications (other than abstracts):

Number of Peer-Reviewed Conference Proceeding publications (other than abstracts):   0

(d) Manuscripts

Number of Manuscripts: 0.00

Number of Inventions:

Graduate Students

NAME	PERCENT_SUPPORTED
Dipankar Sahoo	0.50
FTE Equivalent:	**0.50**
Total Number:	**1**

Names of Post Doctorates

NAME	PERCENT_SUPPORTED
FTE Equivalent:	
Total Number:	

Names of Faculty Supported

NAME	PERCENT_SUPPORTED	National Academy Member
Rodney Bowersox	0.08	No
FTE Equivalent:	**0.08**	
Total Number:	**1**	

Names of Under Graduate students supported

NAME	PERCENT_SUPPORTED
FTE Equivalent:	
Total Number:	

Student Metrics
This section only applies to graduating undergraduates supported by this agreement in this reporting period

The number of undergraduates funded by this agreement who graduated during this period: 0.00

The number of undergraduates funded by this agreement who graduated during this period with a degree in science, mathematics, engineering, or technology fields:...... 0.00

The number of undergraduates funded by your agreement who graduated during this period and will continue to pursue a graduate or Ph.D. degree in science, mathematics, engineering, or technology fields:...... 0.00

Number of graduating undergraduates who achieved a 3.5 GPA to 4.0 (4.0 max scale):...... 0.00

Number of graduating undergraduates funded by a DoD funded Center of Excellence grant for Education, Research and Engineering:...... 0.00

The number of undergraduates funded by your agreement who graduated during this period and intend to work for the Department of Defense 0.00

The number of undergraduates funded by your agreement who graduated during this period and will receive scholarships or fellowships for further studies in science, mathematics, engineering or technology fields: 0.00

Names of Personnel receiving masters degrees

NAME
Total Number:

Names of personnel receiving PHDs

NAME
Total Number:

Names of other research staff

NAME	PERCENT_SUPPORTED
FTE Equivalent:	
Total Number:	

Sub Contractors (DD882)

Inventions (DD882)

Names of other research staff

NAME	PERCENT_SUPPORTED
FTE Equivalent:	
Total Number:	

EXPERIMENTAL ANALYSIS OF THE VORTICITY AND TURBULENT FLOW DYNAMICS OF A PITCHING AIRFOIL AT REALISTIC FLIGHT CONDITIONS

FINAL PROGRESS REPORT

To:

The Army Research Office

Principle Investigator:

Dr. Rodney D. W. Bowersox, Associate Professor
Aerospace Engineering Department
701 HR Bright Bldg., TAMU-3141
Texas A&M University, College Station TX
(bowersox@aero.tamu.edu)

Graduate Research Assistant

Mr. Dipankar Sahoo, PhD Candidate
Aerospace Engineering Department
Texas A&M University, College Station TX

REPORT DOCUMENTATION PAGE

Form Approved
OMB NO. 0704-0188

1. AGENCY USE ONLY (Leave Blank)	2. REPORT DATE 8/31/07	3. REPORT TYPE AND DATES COVERED Final, 4/1/2003 – 4/31/2007

4. TITLE AND SUBTITLE
Experimental Analysis of the Vorticity and Turbulent Flow Dynamics of a Pitching Airfoil at Realistic Flight Conditions

5. FUNDING NUMBERS
DAAD19-03-1-0045

6. AUTHOR(S)
Dr. Rodney D. W. Bowersox and Mr. Dipankar Sahoo

7. PERFORMING ORGANIZATION NAME(S) AND ADDRESS(ES)
Texas Engineering Experiment Station
332 Wisenbaker Engineering Research Center, 3000-TAMU
College Station, TX 77843-3000

8. PERFORMING ORGANIZATION

9. SPONSORING / MONITORING AGENCY NAME(S) AND ADDRESS(ES)

U. S. Army Research Office
P.O. Box 12211
Research Triangle Park, NC 27709-2211

10. SPONSORING / MONITORING AGENCY REPORT NUMBER
44371-EG

11. SUPPLEMENTARY NOTES
The views, opinions and/or findings contained in this report are those of the author(s) and should not be construed as an official Department of the Army position, policy or decision, unless so designated by other documentation.

12 a. DISTRIBUTION / AVAILABILITY STATEMENT

Approved for public release; distribution unlimited.

12 b. DISTRIBUTION CODE

13. ABSTRACT (Maximum 200 words)

The primary objective of this research proposal was improved understanding of the fundamental vorticity and turbulent flow physics for a dynamically stalling airfoil at realistic helicopter flight conditions. To meet this objective, an experimental program using high-resolution particle image velocimetry was performed. High-resolution planar contours of the instantaneous and mean velocity field on a dynamically pitching NACA 0012 airfoil operating in the Texas A&M University large-scale wind tunnel are planned. For the present study, the Mach number, chord Reynolds number, and reduced frequency were selected as 0.2/0.3, 2.0/2.8x10^6 and 0.1/0.18, respectively. The test matrix included static attached, static stall, light dynamic stall and deep dynamic stall. The goal of these analyses was improved understanding of the dynamic stall processes at realistic flight conditions. The velocity data was processed to examine the vorticity and turbulent transport near the leading edge during stall. The data from this study are summarized in this report.

14. SUBJECT TERMS
Dynamic Stall, PIV, Vorticity, Turbulence, Leading-Edge Flow

15. NUMBER OF PAGES

16. PRICE CODE

17. SECURITY CLASSIFICATION OR REPORT **UNCLASSIFIED**	18. SECURITY CLASSIFICATION ON THIS PAGE **UNCLASSIFIED**	19. SECURITY CLASSIFICATION OF ABSTRACT **UNCLASSIFIED**	20. LIMITATION OF ABSTRACT **UL**

GENERAL INSTRUCTIONS FOR COMPLETING SF 298

The Report Documentation Page (RDP) is used for announcing and cataloging reports. It is important that this information be consistent with the rest of the report, particularly the cover and title page. Instructions for filling in each block of the form follow. It is important to **stay within the lines** to meet ***optical scanning requirements.***

Block 1. Agency Use Only (Leave blank)

Block 2. Report Date. Full publication date including day, month, and year, if available (e.g. 1 Jan 88). Must cite at least year.

Block 3. Type of Report and Dates Covered. State whether report is interim, final, etc. If applicable enter inclusive report dates (e.g. 10 Jun 87 - 30 Jun 88).

Block 4. Title and Subtitle. A title is taken from the part of the report that provides the most meaningful and complete information. When a report is prepared in more than one volume, repeat the primary title, and volume number, and include subtitle for the specific volume. On classified documents enter the title classification in parentheses.

Block 5. Funding Numbers. To include contract and grant numbers; may include program element number(s) project number(s), task number(s), and work unit number(s). Use the following labels:

C	- Contract	**PR**	- Project
G	- Grant	**TA**	- Task
PE	- Program Element	**WU**	- Work Unit Accession No.

Block 6. Author(s). Name(s) of person(s) responsible for writing the report, performing the research, or credited with the content of the report. If editor or compiler, this should follow the name(s).

Block 7. Performing Organization Name(s) and Address(es). Self-explanatory.

Block 8. Performing Organization Report Number. Enter the unique alphanumeric report number(s) assigned by the organization performing the report.

Block 9. Sponsoring/Monitoring Agency Name(s) and Address(es) Self-explanatory.

Block 10. Sponsoring/Monitoring Agency Report Number. (*if known*)

Block 11. Supplementary Notes. Enter information not included elsewhere such as; prepared in cooperation with....; Trans. of...; To be published in.... When a report is revised, include a statement whether the new report supersedes or supplements the older report.

Block 12a. Distribution/Availability Statement. Denotes public availability or limitations. Cite any availability to the public. Enter additional limitations or special markings in all capitals (e.g. NORFORN, REL, ITAR).

DOD	-	See DoDD 4230.25, "Distribution Statements on Technical Documents."
DOE	-	See authorities.
NASA	-	See Handbook NHB 2200.2.
NTIS	-	Leave blank.

Block 12b. Distribution Code.

DOD	-	Leave Blank
DOE	-	Enter DOE distribution categories from the Standard Distribution for unclassified Scientific and Technical Reports
NASA	-	Leave Blank.
NTIS	-	Leave Blank.

Block 13. Abstract. Include a brief (*Maximum 200 words)* factual summary of the most significant information contained in the report.

Block 14. Subject Terms. Keywords or phrases identifying major subject in the report.

Block 15. Number of Pages. Enter the total number of pages.

Block 16. Price Code. Enter appropriate price code (NTIS *only*).

Block 17. - 19. Security Classifications. Self-explanatory. Enter U.S. Security Regulations (i.e., UNCLASSIFIED). If form contains classified information, stamp classification on the top and bottom of the page.

Block 20. Limitation of Abstract. This block must be completed to assign a limitation to the abstract. Enter either UL (Unlimited) or SAR (same as report). An entry in this block is necessary if the abstract is to be limited. If blank, the abstract is assumed to be unlimited.

ABSTRACT

The Army Research Office identified improved understanding, predictability and controllability of vortex-dominated and unsteady aerodynamic flows as important for the development of future Army weapon systems. The primary objective of this research project was improved understanding of the fundamental vorticity and turbulent flow physics for a dynamically stalling airfoil at realistic helicopter flight conditions. An experimental program using high-resolution Particle Image Velocimetry (PIV) was performed on a dynamically pitching NACA 0012 wing operating in the Texas A&M University large-scale wind tunnel. The focus of the present study was the leading edge region, where high-resolution [measurement grid spacing of 0.25 mm (= 0.06% of the airfoil chord)] PIV data acquisition concentrated on the first 10-15% of the airfoil. Data were acquired to within 0.5 – 1.0 mm from the airfoil surface. The sample sizes consisted of nominally 1000 - 1300 phase locked image pairs to ensure statistical convergence of the measurements. This report summarized the experiments results for the following test conditions: Case 1 [$M = 0.2$, Re = 2.0 million, k = 0.1, $\alpha = 10 \pm 10 \sin(2\pi ft)$], Case 2 [$M = 0.28$, Re = 2.8 million, k = 0.1, $\alpha = 10 \pm 10 \sin(2\pi ft)$], Case 3 [$M = 0.2$, Re = 2.0 million, k = 0.18, $\alpha = 10 \pm 5 \sin(2\pi ft)$], Case 4 [$M = 0.2$, Re = 2.0 million, k = 0.18, $\alpha = 15 \pm 5 \sin(2\pi ft)$] and Case 5: [Static, $M = 0.2$, Re = 2.0 million]. Nominally, 3 TB of experimental data were acquired. The mean flow data consisted of 2-D planar measurements of the u and v velocity components, Mach number, vorticity, and strain rates. The following turbulence quantities were also measured: u and v components turbulence intensity, the Reynolds shear stress, and the production of the turbulent stresses (xx-, yy-, and xy-components).

TABLE OF CONTENTS

LIST OF SYMBOLS

C	Airfoil chord length (0.457 m)
f	Pitching Frequency (Hz)
k	Reduced Airfoil Pitching Frequency ($\pi f c / U_\infty$)
P_{xx}	Production of the xx-component of the Reynolds Axial Stress
P_{yy}	Production of the yy-component of the Reynolds Axial Stress
P_{xy}	Production of the xy-component of the Reynolds Shear Stress
M	Mach Number
S_{xy}	xy-component Shear Strain Rate
u, v	Instantaneous velocity Components
u', v'	Fluctuating velocity Components
U, V	Mean velocity Components
U_∞	Freestream Velocity
x, y, z	Cartesian Coordinates
α	Angle of Attack
$\Delta\alpha$	Amplitude of the Airfoil Pitching Motion about the ¼-chord
σ_u	$[\overline{u'^2}]^{1/2} / u_\infty$
σ_v	$[\overline{v'^2}]^{1/2} / u_\infty$
ω_z	*z-component of vorticity*
τ_{xy}^T	$-\overline{u'v'}$

LIST OF TABLES

LIST OF FIGURES

viii

Chapter 1

INTRODUCTION

1.1 The Problem of Helicopter Rotor Dynamic Stall

Dynamic stall is a complicated aerodynamic phenomenon. The complications include unsteady flow, separation, hysteresis, compressibility, shock-waves and non-equilibrium (mechanical) boundary layers. The dynamic stall problem has affected helicopters, fighter aircraft, jet engines and wind turbines, and has resulted in major research programs attempting to identify the mechanisms that combine to delay separation and stall on rapidly pitching aerodynamic surfaces. It has been a problem for helicopter designers, for which the abrupt pitching moment variations have forced restrictions on the flight envelope. It has been solution for fighter aircraft, where the dynamically induced lift offers an opportunity for enhancement of aircraft maneuverability.

Dynamic stall occurs on the 'retreating' side of the helicopter rotor (the side where the rotating helicopter blade is traveling away from the direction of flight). The retreating blade must produce sufficient lift to balance the lift produced by the advancing blade in order to maintain level flight. However, the maximum dynamic pressure on the retreating blade can be dramatically less than that found on the advancing blade.

Therefore the lift coefficient for the retreating blade must increase in order to maintain the required lift. This imbalance in dynamic pressure increases rapidly as the speed of the helicopter increases, ultimately requiring dynamic excursions of angle of attack of the rotating blade beyond the angle of attack at which the blade would stall in steady flow, thus leading to dynamic stall conditions.

The airfoil is subjected to two fundamental periodic oscillations: pitching and plunging. A plunging oscillation is a periodic translation of the airfoil in a direction normal to the free stream. A pitching motion is a periodic variation of the angle of attack. The most important parameters affecting the dynamic behavior of an airfoil under periodic variations of inflow conditions are: amplitude of the oscillation, mean angle of attack, reduced frequency, Reynolds and Mach numbers, airfoil shape (thickness, leading edge radius, etc.), surface roughness, and free stream turbulence. With so many factors affecting dynamic stall, the flow field is very complicated. Hence very limited data is available at true flight (helicopter) conditions.

A detailed background review is given in Chapter 2. A main theme that emerged from the literature review is the need for high fidelity experiments directed at improved flowfield understanding and predictability at realistically high Reynolds numbers ($\sim 10^6$) and Mach numbers ($\sim 0.2 - 0.4$). The importance of the flight conditions is highlighted in Chandrasekhara[33] (1998), where the dynamic separation processes were documented to change in fundamental manners with both Reynolds number and Mach number.

1.2 Army Research Office Interests

The Army Research Office [Dr. T. Doligalski, *DAAD19-00-R-0010*] identified improved understanding, predictability and controllability of vortex-dominated and unsteady aerodynamic flows as important for the development of future Army weapon systems. It was also noted that the physics of these flows are Mach and Reynolds numbers dependent, and hence research in this area needs to be performed at realistic flight conditions. Detailed experimental non-intrusive measurements of velocity were also listed as needed in the separating region to yield new phenomenological understanding.

In order to understand the Army research requirements, the Texas A&M University Researchers consulted with Drs. L. Carr and W. McCroskey from the U.S. Army Aeromechanics Laboratory and the NASA Ames Research Center. In summary, specific issues that limit the development of dynamic stall control strategies include (1) a lack of understanding of the basic vortex dynamics with large pressure gradients, (2) the uncertainties of applying quasi-steady turbulence models to dynamic stall problems, (3) the influence of strong adverse pressure gradients on the turbulence models, and (4) the quantification and prediction of transition from laminar to turbulence flow. The present research project was focused on the first three of these Army research requirements.

1.3 Research Objectives and Approach

The primary objective of this research project was improved understanding of the fundamental vorticity and turbulent flow physics for a dynamically stalling airfoil at realistic helicopter flight conditions.

In order to meet the objective, an experimental program using high-resolution Particle Image Velocimetry (PIV) was performed to provide an empirical characterization of the leading-edge (first 10-15% of the chord) flow structure. A dynamically pitching NACA 0012 wing operating in the Texas A&M University large-scale wind tunnel was studied. The region of interest is shown schematically in Fig. 1.1. The data resolution was approximately 0.25 mm (0.06% of the airfoil chord) between data points, and data were acquired to within 0.5 – 1.0 mm from the airfoil surface. The sample sizes consisted of nominally 1000 image pairs to ensure statistical convergence of the measurements. The test matrix is given in Table 1.1.

Table 1.1 Test Matrix

Case	Mach	Re_c (x10^6)	α(degree)	K	Meas. Angles
1[1]	0.20	2.0	$\alpha = 10 \pm 10 \sin(2\pi f t)$	0.10	10-18[2]
2[1]	0.28	2.8	$\alpha = 10 \pm 10 \sin(2\pi f t)$	0.10	10-18[2]
3	0.20	2.0	$\alpha = 10 \pm 5 \sin(2\pi f t)$	0.18	9.2, 11.1, 13.0
4	0.20	2.0	$\alpha = 15 \pm 5 \sin(2\pi f t)$	0.18	13.7, 16.9
5	0.20	2.0	Static	0.00	10, 18

[1]PIV movies were acquired for this flow condition. [2]2.0 degree increments

The measurements included planar contours of the mean velocity (*u-* and *v-*components), vorticity, strain rates, turbulence intensities (*u-* and *v-*components), the Reynolds shear stress, and production of the turbulent stresses (axial, transverse and shear). The vorticity and turbulent transport equations are described in Chapter 3.

1.4 Research Contributions and Scientific Impact

The research project was successfully completed. The specific research contributions include (1) the extensive and highly resolved dynamic stall experimental

database obtained under realistic flight conditions, (2) the subsequent vorticity dynamics analyses and (3) the analysis of the turbulence and the production thereof under the dynamic flow conditions. The primary scientific impact is documentation and improved understanding of the fundamental flowfield processes for a dynamically pitching airfoil at realistic helicopter flight conditions. The results of this research program will be disseminated to the US Army and aerospace industry through contractor reports, archival journal publications and presentations at national conferences.

1.6 Overview of the Contractor Report

Summarized in Chapter 2 are the results from a detailed literature review. Listed in Chapter 3 are the relevant transport equations. The facilities and instrumentation that were employed to perform the current research are presented in Chapter 4. Detailed in Chapter 5 are the experimental technique and data reduction techniques that were used and/or developed in this research. A repository of the acquired data is given in Chapter 6. Brief concluding remarks are given in Chapter 7. Additional data analyses are underway; the results of which will be reported to the ARO through reprints of archival journal papers.

Chapter 2

REVIEW OF DYNAMIC STALL LITERATURE

Unsteady airfoil aerodynamics has numerous military and civilian applications. Some examples include rotor blades, high-angle of attack aircraft and wind turbines. Hence, unsteady airfoils have been the subject of considerable theoretical, experimental and numerical research; most of which has occurred since the late 1940s. Presented in the first section of the review is a brief synopsis that highlights the current state of understanding and prediction of the dynamic stall problem. Given in the second section is a detailed chronological review of the progress in the field starting in 1948 and ending in 2007.

2.1 Overview of the Dynamic Stall Problem

2.1.1 Phenomenological Description

Dynamic stall occurs on the 'retreating side of the helicopter rotor (the side where the rotating helicopter blade is traveling away from the direction of flight). The retreating blade must produce sufficient lift to balance the lift produced by the advancing blade in order to maintain level flight. However, the maximum dynamic pressure on the retreating blade can be dramatically less than that found on the advancing blade. Therefore, the lift coefficient for the retreating blade must increase in order to maintain the required lift.

This imbalance in dynamic pressure increases rapidly as the speed of the helicopter increases, ultimately requiring dynamic excursions of angle of attack of the rotating blade beyond the angle of attack at which the blade would stall in steady flow, thus leading dynamic stall. The problem of dynamic stall has been a topic of great interest to aerodynamicists and scientists. This problem presents a unique combination of unsteady effects, flow non-linearity and strong viscous-inviscid interaction. These challenging and difficult features have stimulated coordinated effort in analytical, experimental and computational research areas. Review articles include McCroskey[1], Carr[2], Carr and McCroskey[3], and Ekaterinaris and Platzer[4]. Literally hundreds of articles are included in these reviews. A brief synopsis is given here.

McCroskey[1] points out that one of the reasons that dynamic stall is so difficult to analyze is that it depends on a large number of parameters. He listed airfoil shape, Mach number (> 0.2), reduced frequency, mean angle and oscillation amplitude as having large effects on dynamic stall. He also indicated that Reynolds number had an unknown effect at high Mach numbers. Two general stages of dynamic stall, light and deep, have been defined. Light and deep dynamic stall flows are compared in Figure 2.1. Light dynamic stall occurs for lower maximum angle of attacks than are typically associated with the deep stall. One of the distinguishing features of light dynamic stall is the relatively small vertical extent of the viscous region, as compared to deep stall, and the stall behavior is closely related to the boundary layer separation behavior. Deep stall occurs when the maximum angle-of-attack significantly exceeds the static stall angle, and the flow

separation is initiated with formation of a strong vortex-like structure in the leading-edge region of the flow.

Shown in Figure 2.2 are sketches (boxed images on the right-hand-side) of the canonical low-Mach flow deep stall events. Dynamic stall generally refers to complex unsteady flow processes that lead to dynamic delay of stall on aerodynamic bodies Carr[2]. Following Carr[2], Ekaterinaris and Platzer[4] and Greenblatt *et al.*[5], state (a) corresponds to the event where the airfoil dynamically pitches beyond the static stall. Stages (b)-(d) indicate initiation of the vortex formation starting with viscous disturbances. State (e) corresponds to the initial vortex development near the airfoil leading edge as the angle of attack is rapidly increased past the static stall angle. This vortex then convects downstream near the airfoil surface, which causes an increase in lift and strong pitching-moments due to suction created by the vortex [stages (f) through (i)]. The magnitude of the lift depends on the strength and location of the vortex. The streamwise movement of the vortex depends on the airfoil shape and pitch rate. Full dynamic stall occurs at stage (j) and continues until the airfoil angle-of-attack has reduced such that attached flow state re-occurs. As a result of this sequence of events, the unsteady lift, drag and moment coefficients show a large degree of flow hysteresis when plotted versus angle of attack (plot on the left-hand-side of Figure 2.2). The sequence of events, amount of hysteresis and the shape of the hysteresis loop depend nonlinearly on amplitude of oscillation, mean angle of attack, reduced frequency ($k = \omega c/2u_\infty$), Mach number and Reynolds number.

2.1.2 Prediction Methods and Limitations

Two basic methodologies exist for predicting dynamic stall. The first method uses semi-empirical relations founded in oscillating thin airfoil theory for the prediction of forces and moments McCroskey[1], Ekaterinaris and Platzer[4] and Leishman[6]]. The second, more modern, approach is founded in computational fluid dynamic (CFD) solutions of the Navier-Stokes equations. CFD methods have become increasing popular since the mid 1980's with the continual advancement of computational capabilities. These tools have provided very valuable insight into the flow processes [e.g., see Ekaterinaris and Platzer[4] and Choudhuri *et al.*[7]] especially for laminar flow. However, Ekaterinaris and Platzer[4] note that predictions of dynamic stall on helicopters and wings, involving realistically high Reynolds number turbulent flows, will only contribute toward improved flowfield understanding if progress is made toward improving the ability to numerically predict turbulent flow and transition.

The computational requirements for direct numerical simulation, or even large-eddy simulation, of realistic turbulence problems are prohibitive. Hence, engineers and scientists must rely on approximate averaged forms of the Navier-Stokes equations that involve turbulence modeling. Ekaterinaris and Platzer[4] summarize the performance of the available range of turbulence models (algebraic, half-equation, one-equation and two-equation) all of which invoke the Boussinesq[8] approximation. The results were found to strongly depend on the turbulence model. Hence, accurate models are required. Furthermore, the available models could not be tuned to produce accurate prediction of the lift, moment and drag loops; instead, the models could only be tuned to produce

accurate prediction of one. Barakos *et al.*[9] and Ko and McCroskey[10] also confirmed these general conclusions.

The poor performance of the available eddy-viscosity type models is not surprising. First, the deficiencies of the Boussinesq[8] approximation are well documented. Wilcox (2000)[11] reports that this approximation fails for (1) flows with sudden changes in the mean strain rates, (2) flow over curved surfaces, (3) flows in ducts with secondary motion, (4) rotating flow, (5) three-dimensional flow and (6) flows with boundary layer separation. Referring to flowfield in Figure 2.1, it is not surprising that the available models fail for the present class of flows. Second, Ekaterinaris and Platzer[4] reported that none of the current turbulence models were validated for dynamic stall.

The development and validation of turbulence models requires empirical information. Although quantitative flowfield studies have been performed [e.g., Carr *et al.* [12] and Shih *et al.*[13]], detailed turbulent field data for a dynamically stalling airfoil is lacking, as discussed in Ekaterinaris and Platzer[4].

2.2 Chronological Description of the Dynamic Stall (1948 To 2007)

The goal of this section is to present an overview of the chronology of progress in key focus areas. For more exhaustive reviews see McCroskey[1], Carr[2], Carr and McCroskey[3], and Ekaterinaris and Platzer.[4]

Harper and Flanigan[14] showed that the lift on an aircraft can be significantly increased if the aircraft is pitched at a rapid rate. Carta[15] was able to identify a pressure field on oscillating, two-dimensional airfoil that was indicative of the passage of a vortex. The importance of unsteady aerodynamics was considered by Harris and Pruyn[16]. It was

observed that the extra lift on the helicopter rotor could be explained if lift on the blade was greater than that predicted by steady flow during the time when the blade was moving opposite to the direction of flight (the retreating-blade condition). Ham and Garelick[17] observed that the extra lift could be created by rapid pitching of airfoils, and this extra lift was associated with a vortex formed on the airfoil during the unsteady motion. This was modeled by Ham[18] to reproduce the same form of dynamic overshoot that was observed in helicopter flight tests. Liiva and Davenport[19] also observed this vortex passage and the corresponding dynamic pressure distribution.

McCroskey and Fisher[20] explored dynamic stall on a model rotor and verified that the dynamic effects were indeed a result of a vortex dominated flow field that occurred during blade motion into the low-dynamic- pressure environment of the third and fourth quadrants of the helicopter rotor. This model rotor test, and further two-dimensional airfoil wind tunnel tests, then produced more quantitative information about dynamic stall.

Experiments were performed by Martin *et al.*[21] using flow-visualization techniques to again demonstrate the presence of vortex. These data reveal a number of interesting Reynolds number, amplitude, and reduced frequency effects on dynamic stall. They intended to point out the importance of testing under actual helicopter rotor operating conditions and that this approach can eventually describe the mechanism of dynamic stall. The angle for stall initiation decreases with increasing *Re*, while the angle for maximum lift increases with increasing *Re*. Hot-wire anemometry data indicated the occurrence of a short bubble during both the upstroke and down stroke. The angle of

bubble passage, for a given *x/c*, decreases as *Re* increases. They concluded that decrease in pressure at the leading-edge and peaking of leading-edge velocity is the surest indicator that the process of stall initiation has begun. Increasing reduced frequency increases the stall delay.

McCroskey, McAlister and Carr[22] performed dynamic stall experiments on oscillating airfoils. They studied dynamic stall and unsteady-boundary layer separation in incompressible flow at moderately large Reynolds numbers. By varying the leading-edge geometry of an NACA 0012 airfoil, three different types of stall were produced, and the vortex shedding phenomenon was found to be the predominant feature of each. In most cases, including the leading-edge stall on the basic NACA 0012 profile, dynamic stall was found not to originate with the bursting of a laminar separation bubble, as is commonly believed, but with a breakdown of the turbulent boundary layer. Results in this experimental investigation can be summarized as 1) trailing edge stall developing from a relatively gradual progression of boundary-layer flow reversal and separation, from the trailing edge toward the leading edge; 2) leading-edge stall caused by an abrupt breakdown of the turbulent flow on the forward portion of the airfoil, following an initial progression of flow reversal from the trailing edge, and 3) two forms of leading-edge stall due to the abrupt bursting of a leading-edge laminar separation bubble.

Sankar and Tassa[23] solved the unsteady two-dimensional Navier-Stokes equations for laminar compressible flow around a NACA 0012 airfoil. They presented the governing equations in a strong conservation form in a body-fitted coordinate system, and solved them using an alternating direction implicit procedure. The technique was

applied to the dynamic stall of a NACA 0012 airfoil, for several combinations of Mach number, Reynolds number and reduced frequency. They concluded compressibility has an inhibiting effect on the formation of the leading edge vortex. The decrease in reduced frequency increases the intensity of the dynamic stall vortex shedding, and a lower reduced frequency also leads to an earlier formation and growth of the leading-edge vortex. They found the Reynolds number to be a weak parameter.

Lorber and Carta[24] performed experiment to study the aerodynamics of dynamic stall penetration at constant pitch rate and high Reynolds number, in an attempt to model more accurately conditions during aircraft poststall maneuvers and during helicopter high-speed forward flight. The results demonstrate the influence of the leading-edge vorticity on the unsteady aerodynamic response during and after stall. The vortex is strengthened by increasing the pitch rate and is weakened by increasing the Mach number and by starting the motion close to the steady-state stall angle. The level of understanding required to make proper use of this effect has yet to be achieved. Consistent control of unsteady, separated flow will be required if fighter pilots are to make full use of the expanded aerodynamic boundaries that will be made available by unsteady aerodynamics; this emphasizes the need for basic research in three-dimensional dynamic-stall effects, compressibility effects on dynamic stall, and positive control of unsteady separated flow, as well as in other fundamental areas of unsteady aerodynamics.

Chandrasekhara and Carr[25] studied compressibility effects on dynamic stall of a NACA 0012 airfoil undergoing sinusoidal oscillatory motion using a stroboscopic schileren system. Their study showed that a dynamic stall vortex always forms and

13

convects over the airfoil upper surface at approximately 0.3 times the freestream velocity for all cases studied. The results also demonstrate that occurrence of deep stall is delayed to higher angles of attack with increased reduced frequency, even when compressibility effects are present, but increasing Mach number alone has the opposite effect. They concluded dynamic stall vortex is present at all Mach numbers and reduced frequencies. However, its strength and initiation angle appear to vary with Mach number. Increasing the reduced frequency helps in holding the dynamic stall vortex on the airfoil surface to higher angles of attack, for high Mach numbers as well. Compressibility effects are significant beyond $M = 0.3$. Dynamic stall occurs at lower angles of attack as the Mach number exceeds 0.3. However, the origin of the vortex was not clear from the tests. They were also not able to find out the shock near the leading edge.

Carr, Platzer, Chandrasekhara, and Ekaterinaris[26] performed experimental and computational studies on dynamic stall. The dynamic overshoot of lift that characterizes the dynamic stall process is the key characteristic that is of interest to the aircraft designer; the strong pitching moment is the reason why the helicopter designer avoids dynamic stall. Review of past studies of dynamic stall demonstrates that compressibility will play a major role in effective use of dynamic lift. In particular, it has been shown that as the free stream Mach number exceeds 0.2, local supersonic flow develops around the leading edge of airfoils that pitch rapidly past the static stall angle. This region of supersonic flow can dramatically change the way that airfoil stall develops, changing a trailing-edge stall at low Mach number to a leading-edge stall at higher Mach number $(M \approx 0.3)$. They concluded 1) the dynamic stall vortex appeared for all cases

studied experimentally, but its initiation occurred at significantly lower angles of attack as the Mach number increased. The vortex could be delayed by increasing the oscillation frequency across the full Mach number range of the experiment, 2) the stroboscopic schlieren offers the first truly instantaneous visualization of the dynamic stall vortex, since it is sensitive only to density gradients at the time of the photograph, 3) the Navier-Stokes model of dynamic stall initiation shows good agreement with lift and pitching moment magnitudes, but requires prior knowledge of the state of the flow turbulence in order to model the details of the flow field after stall begins, 4) viscous-inviscid interaction techniques offer a way to analyze the dynamic stall onset at a computational cost which could be practical for design purposes.

Shih, Lourenco, Van Dommelen, and K Rothapalli[13] investigated unsteady flow past a NACA 0012 airfoil in pitching-up motion in a water towing tank using the particle image displacement velocimetry (PIDV) technique. The Reynolds number based on the free stream velocity and the chord length is 5000. The airfoil pitching motion was from 0 to 30 deg angle of attack at a dimensionless pitch rate of 0.131. They observed boundary-layer separation near the airfoil leading edge leads to the formation of a vertical structure. The evolution of this vortex along the upper surface dominates the aerodynamic performance of the airfoil. Complete stall emerges when the boundary layer near the leading edge detaches from the airfoil, under the influence of the vortex. This vortex triggers the shedding of a counter-rotating vortex near the trailing edge.

Wilder, Chandrasekhara, Carr[27] studied transition effects on compressible dynamic stall of transiently pitching airfoils. They concluded the laminar separation

bubble present in the untripped flow was found to have a beneficial effect on dynamic stall delay. Dynamic stall onset moves closer to the leading edge in the presence of a trip, which eventually leads to stall at lower angles of attack (by about 1 – 1.5 degrees) than observed in untripped airfoil dynamic stall. The leading-edge adverse pressure gradient and the peak suction pressure coefficient were lower in value on the tripped airfoil. The behavior of the flow is grossly different under compressibility conditions with a trip. The shock/boundary layer interactions are modified by the trip, as also is the leading edge pressure gradient. The sensitivity of the flow to the state of the boundary layer turbulence points to a need for highly refined computational flow modeling.

Knight and Chowdhury[28] studied 2-D unsteady leading edge separation on a pitching airfoil. The Reynolds number considered was 10000, Mach number 0.2 and the dimensionless pitching rate as 0.2. They performed computations using two separate algorithms for the compressible laminar Navier-Stokes equations. Their results revealed that the appearance of the primary recirculating region has been traced to the emergence of a pair of critical points (saddle and center) in the flow at approximately the 18% chord location at an angle of attack close to 15 degrees. The primary recirculating region (center) has a clockwise sense of fluid rotation, and grows with increasing angle of attack. Secondary and tertiary recirculating regions form after the appearance of the primary recirculating region. The sense of fluid rotation is counter-clockwise and clockwise respectively. Subsequent to the formation of secondary and tertiary recirculating regions, the boundary layer erupts due to the interaction of the recirculating regions. The primary recirculating region detaches from the airfoil surface and forms the

16

dynamic stall vortex. The appearance of the primary recirculating region does not signify separation. For higher Mach number compressibility affects the process of stalling. Compressibility effects can and do play a significant role in the development of the unsteady flowfield on rapidly pitching airfoils.

Carr, Chandrasekhara, and Broke[12] performed a quantitative study of unsteady compressible flow on an oscillating airfoil. Point diffraction interferometry permitted the detailed study of the complex unsteady flow near the leading edge of an oscillating airfoil, and quantitative flow information has been obtained both on the surface and in the surrounding flowfield for a range of frequencies and Mach numbers. A laminar separation bubble was observed in most of the higher angle conditions, although the occurrence of the bubble can be delayed by unsteadiness. Locally supersonic flow was observed near the leading edge, but the region of supersonic flow was quite small. Unsteadiness significantly relieves the pressure gradient that occurs in this region. The performance limitation of a helicopter stemmed from the leading-edge flow separation causing dynamic stall on the retreating blade of the helicopter during the pitch up stroke. The flow eventually reattached during the pitch down cycle. Depending on the mean angle of attack, amplitude, and frequency of oscillations, a hysteresis loop of varying size developed. This loop determines aerodynamic damping. An understanding of this reattachment process may help in modifying flow. For example, if the process can be completed rapidly, the airfoil will be able to generate more lift through the cycle, thus altering its performance. The damping can be negative during certain parts of the cycle, resulting in an increase in the amplitude of oscillation causing stall flutter. An

understanding of the reattachment process is therefore essential to alleviate the stall flutter and to improve the dynamic lift characteristic of an oscillating airfoil.

Niven, Galbraith, and David[29] made the first attempt to analyze the reattachment of separated flow of a two-dimensional wing undergoing ramp down motion through surface pressure measurements. This study showed that the reattachment process occurs over a finite length of time and the airfoil incidence at reattachment was found to be close to the static stall angle. However, no flowfield measurements were available to understand the physics of the flow field.

Ahmed and Chandrasekhara[30] studied the reattachment of an oscillating airfoil dynamic stall flow field using the techniques of stroboscopic schlieren, two-component laser Doppler velocimetry, and point diffraction interferometry, for a freestream Mach number 0.3 and reduced frequency 0.05. The major conclusions from their studies were as follows. Reattachment of the dynamic stall flow is a continuous process, unlike that in a steady flow. The process includes development of larger than freestream velocities near the airfoil surface as the process advances over it. Reattachment begins at or near the static stall angle even in unsteady flow. As the flow begins to reattach, the suction pressure coefficient rises rapidly, but its values are different from those in the steady flow and the unsteady flow during the upstroke at the same angle of attack. For the Reynolds number of the experiment, reattachment process progresses through a separation bubble, which changes size during the process and disappears at a low angle of attack. Reasonable agreement was found between LDV and PDI studies, enhancing the confidence level of the measurements. Lift enhancement by unsteady airfoil motion

18

through the production of coherent vorticity is a problem of both fundamental and practical interest. The potential benefits of dynamically delaying stall of an airfoil offers possibilities for expanding the flight envelope of full-scale aircraft systems. The dynamic stall of an oscillating (or a transiently pitching) airfoil originates from the failure of the laminar separated flow to reattach as the angle of attack increases, resulting in the formation of the dynamic stall vortex from the bursting of a separation bubble. Since the separation bubble is a consequence of transition of the laminar separated shear layer, it can be concluded that transition physics plays a major role in the dynamic stall process. Additional complexity is introduced by the ever-changing transition behavior such as reduction of transition length with increasing pressure gradient (as the airfoil pitches to a higher angle of attack). Thus, it is desirable to remove the transition effects by predetermining the transition point and fixing it so that the effects of compressibility due to the large local fluid velocities around the leading edge can be clearly isolated. Traditionally, fluid dynamicists have tripped the boundary layer in the hope of achieving Reynolds number similarity and removing transition effects as a parameter in low-Reynolds number studies.

Chandrasekhara, Wilder, and Carr[31] presented results of boundary-layer tripping studies of compressible dynamic stall flow. The criteria for successful tripping were established as the elimination of the laminar separation bubble that otherwise forms, delay of dynamic stall onset angle, and production of larger suction peaks at corresponding angles of attack when compared with an untripped airfoil dynamic stall flow. The results showed that the dynamic stall flow was extremely sensitive to the trip

19

used and hence to the state of turbulence in the flow immediately downstream of the trip. The optimum trip was determined to consist of a distributed roughness whose height was comparable to (but less than) the boundary-layer thickness in the adverse pressure gradient region and upstream of the point where the dynamic stall vortex forms over untripped airfoil. The large variability in the details of the dynamic stall process of an untripped airfoil was removed by fixing the transition point. The data generated thus are believed to be useful in validating compressible dynamic stall flow computations.

Ko and McCroskey[10] studied computations of unsteady separating flows over an oscillating airfoil. The primary objective of their study was to identify the most accurate, robust and economic turbulence model for dynamic stall computations. In dynamic stall computations, a two-dimensional, body-fitted C-type computational grid moves in a sinusoidal pitching motion about an airfoil's quarter chord in the inertial reference frame. They selected Baldwin-Lomax (B-L) model because of its popularity as a zero-equation model. The Spalart-Allmaras (S-A) model is chosen among one-equation model because of its excellent performance. Finally, the $\kappa - \varepsilon$ model is selected because it is the most popular two equation model. The predictions by S-A and the $\kappa - \varepsilon$ models agree very well with the measured data for all three force coefficients C_l, C_d, and C_m. The B-L model shows fairly good agreement with the measurements for C_l, C_d but not for C_m.

Geissler, Carr, Chandrasekhara, Wilder, and Sobieczky[32] performed a computational study of compressible dynamic stall flow which includes the role of boundary layer transition. They also considered variable geometry airfoils. The study addressed the inadequacies of modeling the dynamic stall flow without incorporating the

20

effects of transition. Fairly good agreement was obtained between the experiments and calculations for the NACA 0012 airfoil at a Reynolds number of 1.1×10^6 despite the fact the flow experienced the large scale flow separation associated with deep dynamic stall. This prompted the extension of the model to the DDLE airfoil where the nose radius is very large. In this case, both experiment and calculation shows the negative pressure peak on the airfoil upper surface continues to increase as the angle of attack increases to 17^0. This is in strong contrast to the NACA 0012 results, where bubble bursting and dynamic stall onset occur at 14^0 angle of attack. Earlier experiments have documented the onset of compressible dynamic stall either from the bursting of a leading-edge laminar separation bubble or from a leading-edge shock, depending on the Reynolds number and Mach number. However, for certain combinations of conditions, the supersonic flow and the bubble dynamics compete with each other. The consequent complex interactions lead to a newly discovered mechanism of dynamic stall onset.

Details of these various mechanisms were discussed by Chandrasekhara, Wilder, and Carr[33]. They concluded that compressible dynamic stall is influenced by three different, competing factors at low and moderate Reynolds numbers. Dynamic stall is caused by the bursting of the laminar separation bubble at low Reynolds numbers and moderate Mach numbers. As the Mach number is increased, the interaction between the supersonic flow and the bubble can initiate the dynamic stall process. At still higher Mach numbers, shock induced boundary-layer is the cause of dynamic stall process. The dynamic stall flow and vortex evolve under a supersonic external flow. Depending on local flow conditions, the fluid dynamic interactions vary, thus strongly influencing the

dynamic stall onset process. All of these aspects need to be modeled properly if attempts to compute the flow are to be successful. The strong pitching moment that accompanies dynamic stall is well known to be highly detrimental to helicopter performance. Furthermore, compressibility effects induce a premature onset of dynamic stall at freestream Mach numbers as low as 0.3, which greatly limits the performance of a rotor. The phenomenon of unsteady flow separation also limits the operational envelope of fixed-wing aircraft when it is encountered during airfoil flutter, buffet, etc. control of both steady and unsteady flow will expand the flight envelopes of future aircraft designs. Recent studies have shown that compressible dynamic stall can be caused either by an extremely strong adverse pressure gradient in the flow near the leading edge or by a shock-induced separation occurring in this region. Because both phenomena are a consequence of the fixed-airfoil geometry, there appears no simple way to significantly alter these conditions. However, the use of smart materials and actuator offers the possibility of designing wings that can continuously and rapidly adapt to changes in local flow conditions, thereby enabling these wings to deliver optimum performance at each instantaneous flow condition.

Upon recognizing that dynamic stall at practical Mach numbers is induced by rapid flow acceleration followed by abrupt deceleration around the leading edge, Chandrasekhara, Wilder, and Carr[34] developed a control strategy to modify the flow gradients by suitably shaping the airfoil leading edge. The goal was to reduce the local Mach number in the leading-edge region and to favorably alter the leading-edge pressure distribution, thereby introducing possible delays or elimination of the onset and effects of

dynamic stall. In other words the aim was to achieve control of flow separation and to eliminate dynamic stall vortex through dynamic airfoil leading-edge curvature change and, thus, effect vorticity management in the flow. This approach in turn leads to the concept of dynamically deforming leading edge. Dynamically changing the airfoil curvature showed that it is preferable to change the curvature slowly for the flow to adjust to the instantaneous geometry if control is to be effective. DDLE airfoils with shape 8.5 at M=0.3 and shape 6 at M=0.4 both were dynamic stall free, and the leading edge flow was always attached, even though there was some trailing-edge separation present in the flow. This remarkable result, thus, validated the use of the DDLE airfoil concept for achieving dynamic stall control. Changing the leading-edge curvature of an NACA 0012 airfoil was effective in producing significant stall delay (about 5 deg at M=0.3) through decreasing leading-edge flow acceleration. The extreme sensitivity of the airfoil peak suction pressure to the flow acceleration around the airfoil leading edge resulted in reduced peak suction levels when the nose radius was increased. Rounding the leading-edge also distributed the low pressure region over a wider extent on the airfoil upper surface, reducing the leading edge adverse pressure gradient, thus making it possible for the airfoil to reach higher angles of attack before stalling, in both steady and unsteady flows.

Greenbalt, Nishri, Darabi, and Wygnanski[35] presented some recent developments in separation control. Specifically, the effects of net mass-flux superposition, curvature, large flap deflection and extended reduced frequency range were considered on static configurations. Additionally, the bases of dynamic stall, as well as the means to affect its

23

control, were emphasized. The superposition of blowing, together with periodic excitation, was found to detrimental to separation control, while suction was beneficial. Specifically, the length and transverse height of the ubiquitous separation bubble were increased while suction initiated the bubble formation closer to the slot and shortened its length. Considerations of streamline curvature confirmed the effectiveness of these reduced frequencies but emphasized the importance of actuator location on separation control with curvature. Due to the nature of momentum transfer by the large eddies, under certain conditions, form drag was found to exceed total drag- indicating negative net skin friction. The effect of reduced frequency on lift enhancement indicated that the most effective frequencies for separation control are in the approximate range $0.3 \leq F^+ \leq 4$, confirming the findings of many in-house and other investigations. Small amplitude excitation in this range dramatically reduces the lift and moment oscillations resulting from unsteady separation and vortex shedding. Simulated dynamic stall on a stationary flap, compared with an airfoil undergoing dynamic stall at rotorcraft reduced frequencies, demonstrated the principle of time-scale disparity between the destructive dynamic stall vortex (DSV) and the controlling large coherent structures (LCS).

A study of the mechanisms of dynamic stall control on an airfoil revealed that excitation effectively removed the DSV and rendered the aerodynamic coefficients independent of airfoil oscillation rate, k. moreover, the generation and advection of LCS's over the airfoil surface at maximum incidence was similar for both dynamic and static cases. Consequently, the resultant oscillations in aerodynamic coefficients were

negligibly small and large instantaneous post-stall excursions, typical of the baseline data, were all but eliminated.

Chandrasekhara, Wilder, and Carr[36] performed experiments focusing on controlling the flow over a sinusoidally oscillating airfoil by determining the dynamic shape variations that produced the right nose curvature at each instantaneous flow condition, thus producing the most attached flow over the range of angles of attack interest. They chose a sharp to round shape profile, while always maintaining the airfoil shapes within the range of a previously determined attached flow envelope, to achieve the desired flow control effect. They concluded compressible dynamic stall can successfully be controlled using dynamic shape adaptation. This required a very small (0.6 mm) change in the chord length of a dynamically adaptive airfoil that produced a nearly 150% change in the leading-edge radius of curvature. The flow was found to be dynamic stall vortex free for $M = 0.3$, $k = 0.5$ and $\alpha(deg) = 10 + 10 \sin(\omega t)$. The favorable effects of dynamic shape adaptation realized through changes in the instantaneous potential flow resulted in broader pressure distributions with lower peak suction values and led to a redistribution of the unsteady flow vorticity. The vorticity level decreased to values where the dynamic stall vortex did not form. The peak suction variation loop over the oscillation cycle was found to be the smallest for the adapting airfoil. The deformation rate, the initial angle of attack, and the amount of nose curvature change affect the success of the approach significantly. The most benefit is produced while remaining within the attached flow envelope for a given Mach number during dynamic shape adaptation.

Greenbalt, Nishri, Darabi, and Wygnanski[37] discussed the parameters governing steady separation control and the time resolved mechanisms that affect the control. They also described the classical DSV development and the analogy between dynamic stall simulation (and its control) on a stationary deflected flap with classical aerodynamic stall. This characterization illustrates the pivotal importance of the different time scales associated with dynamic stall vs. those of the controlling LCSs. The principal objective of their work was to study the mechanisms that affect dynamic stall and its control. They concluded excitation effectively removed the DSV and significantly attenuated trailing-edge separation. Phase-averaged dynamic pressure distributions at maximum incidence were almost identical to static under the same excitation conditions. The comparisons improved further with increasing excitation frequency. The generation and advection of LCSs over the airfoil surface at maximum incidence were similar, with differences in amplitude and phase velocity diminishing with increasing excitation frequency. Excitation rendered the aerodynamic coefficients effectively independent of airfoil oscillation rate k. Oscillations in the aerodynamic coefficients induced by the excitation were insignificantly smaller when compared to the phase-averaged quantities. Excitation effectively eliminated the large instantaneous post-stall excursions, typical of the baseline aerodynamic coefficients, resulting in small differences between instantaneous and phase averaged data.

Greenbalt and Wygnanski[5] performed a parametric study to investigate the effect of periodic excitation (with zero net mass flux) on a NACA 0015 airfoil undergoing pitch oscillations at rotorcraft reduced frequencies under incompressible conditions. The

primary objective of the study was to maximize airfoil performance while limiting moment excursions to typical pre-stalled conditions. Their study yielded following principal conclusions. Light stalls, as well as deep stall, were effectively controlled by oscillatory excitation. The beneficial effects of excitation were more pronounced at higher airfoil oscillation rates and effectively independent of Reynolds number. Flap-shoulder excitation, in conjunction with pre-stall pitch excursions, was more aerodynamically efficient than excitation employed in the post-stall regime. As more information about and greater understanding of the dynamic stall process has been developed, efforts have focused on ways to delay formation of the dynamic stall vortex to higher angles of attack, or even to eliminate it from the operating environment of the helicopter. The dynamic stall study of slotted airfoil configuration demonstrated that there is indeed a way to suppress the dynamic stall vortex. Suppression of the dynamic stall vortex resulted in elimination of the pitching moment excursions that are the primary reason that dynamic stall conditions must be avoided.

Carr, Chandrasekhara, Wilder, and Noonan[38] tested a multi-element airfoil designed for helicopter applications for compressible dynamic stall behavior and proved to be a robust dynamic stall-free concept. This slotted airfoil has operated into post-stall areas without the dynamic stall vortex that is normally present whenever airfoils are tested beyond their static stall boundary. One of these slotted airfoils, operated throughout the range of Mach numbers representative of helicopter flight without experiencing a dynamic stall vortex at any condition tested, thus demonstrating the value of such a configuration for application to future helicopters. A detailed discussion of the

flow on the optimum slot design showed that the design was effective in suppressing the dynamic stall vortex, even at the high Mach numbers that have negated the effectiveness of many flow control concepts. Significant compressibility effects were observed, including a strong shock appearing in the slot for certain dynamic conditions. This shock played an important role in the development of the flow at high angle of attack and shows the type of flow condition that only occurs during dynamic motion at compressible flow conditions. Flow separation on the slat and main airfoil element progressively increased as the Mach number increased, but no dynamic stall vortex was observed at any of the conditions tested. A comparison with the basic single-element airfoil, as well as a second slat design, showed the improvements that can be attained through effective slat design. The slot-jet continued to energize the main element boundary layer even after the slat stalled. This suggests the possibility that there may be some special slot geometries that are the most efficient for this task. However, the many conflicting requirements of the main element leading-edge geometry for the wide ranging conditions of the rotor need to be considered carefully if this effort is to succeed. Instantaneous pressure distributions were presented showing the influence of slat design on the suction peak that occurs in the pressure distribution. A discussion of Reynolds number effects was presented that indicated that the dynamic stall suppression resulting from use of the slat concept also seems to be insensitive to changes in Reynolds number.

Chapter 3

VORTICITY AND TURBULENCE TRANSPORT EQUATIONS

3.1 Vorticity Transport Dynamics

   The mean vorticity (Helmoholtz) transport equation is written for Reynolds averaged turbulent flow following Bowersox[22] as

$$\frac{D\bar{\omega}}{Dt} = -\bar{\omega}(\nabla \cdot \bar{V}) + (\bar{\omega} \cdot \nabla)\bar{V} + \frac{1}{\bar{\rho}}\nabla x(\nabla \cdot \Pi) - \nabla x\left(\frac{1}{\bar{\rho}}\nabla\bar{p}\right) + \nabla\left(\frac{1}{\bar{\rho}}\right)x(\nabla \cdot \Pi) \qquad (3.1)$$

The left-hand side of Eq. (1) contains the local unsteady and convective vorticity transport. The first two terms on the right-hand side depict the familiar compressibility and three-dimensional vortex stretching. The third term denotes the molecular diffusion and anisotropic turbulent transport, where the tensor Π includes both the molecular and turbulent (Reynolds or Favre averaged) shear stresses. The fourth term is the baroclinic torque, and the last term represents an anisosteric (i.e., variable density) molecular and turbulent diffusion. Direct calculation of ensemble-averaged contours of the vorticity (z-component), convection, compressibility, and vortex stretching terms are possible with the acquired data.

3.2 Turbulence Transport Equation

The turbulent shear stress transport is given by [Wilcox[11]]:

$$\tau_{ij,t}^T + (\overline{u}_j \tau_{ij}^T)_{,j} = -\tau_{ik}^T \overline{u}_{j,k} - \tau_{jk}^T \overline{u}_{i,k} + \overline{u_j'' \overline{p}_{,i}} + \overline{u_i'' \overline{p}_{,j}} - \overline{\tau_{ik,k} u_j''} - \overline{\tau_{jk,k} u_i''} - \overline{p'(u_{i,j}'' + u_{j,i}'')}$$
$$- [\overline{(\rho u_i'' u_j'' u_k'')} - \overline{p' u_i'' \delta_{jk}} - \overline{p' u_j'' \delta_{ik}} + \overline{(\tau_{ik}' u_j'' + \tau_{jk}' u_i'')}]_{,k} + \overline{\tau_{ik}' u_{j,k}''} + \overline{\tau_{jk}' u_{i,k}''} \quad (3.2)$$

The left-hand side of Eq. (2) contains the local unsteady and convective turbulent shear stress transport. The first two terms on the right-hand side are the turbulent shear stress production; the third and fourth are the pressure-work; the fifth and sixth are the "viscous-work;" the seventh term is the pressure-strain redistribution; the eight term is diffusion, and the last is the dissipation. Direct measurement of the production was achieved.

Chapter 4

EXPERIMENTAL FACILITIES

To accomplish the dynamic stall measurements, a Dynamic Stall Facility (DSF) was constructed. The DSF included the combination of area reducing inserts to the Oran Nicks Low-Speed Wind Tunnel and a hydraulic actuation apparatus to dynamically move the wing. The inserts were designed to increase the flow velocity and to transfer the wing loads to the tunnel support structure. A large-scale NACA 0012 wing was constructed for the present study. A detailed description of the facilities is given below.

4.1 Oran Nicks Low-Speed Wind Tunnel

The Oran W. Nicks Low Speed Wind Tunnel at Texas A&M University (TAMU) is a self-contained research facility. It is a closed circuit tunnel with a rectangular test 2.1 m high, 3.0 m wide and 3.7 m long (7 ft x 10 ft x 12 ft) fabricated of structural steel lined with marine plywood. The corners have 0.3 m (12 in) fillets. The maximum Mach number is 0.25, which corresponds to a velocity of 85 m/s (200 mph). Three inch wide vertical venting slots in the side walls at the test section exit maintain near atmospheric static pressure. The test section side walls diverge about 0.083 m per meter distance in along the stream wise direction to account for boundary layer growth. Figure 4.1 shows the facility schematic and photographs of the test section.

4.2 The DSF Inserts

The DSF consisted of inserts to increase the flow velocity in the Orin Nicks Tunnel and to support the loads during dynamic actuation of the wind tunnel model (described in the next section). A Mach number of 0.3 was achieved in the present test. However, with additional modifications to the diffuser, Mach 0.4 is believed possible. The inserts were designed to reduce the test section to 2.1 m x 2.1 m (7 ft x 7 ft). The flow conditions are listed in Table 1.1. A detailed description of the insert design is given below.

4.1.1 Tunnel Flow

Computation Fluid Dynamics (CFD) was employed to design the inserts to achieve uniform flow in the reduced area test section. Preliminary CFD analysis was done on the current wind tunnel (Oran W Nicks Low Speed Wind Tunnel) to validate the design methods. The physical dimension of the tunnel was measured and incorporated into SolidWorks. The SolidWorks drawing was used to generate the grid in GAMBIT. The physical dimension of the tunnel that was simulated was divided into 3 sections: a 1.83 m (6 ft) inlet, a 4.87 m (16 ft) test section, and a 12.2 m (40 ft) long diffuser. Total length of the wind tunnel simulated was 18.9 m (62 ft). The CFD code FLUENT was used to compute the flow. Due to the symmetric nature of the wind tunnel only one-quarter of the grid was simulated. This feature helped in reducing the computational time. The boundary conditions were as follows:

1. Inlet

2. Outflow

3. Wall

4. X – Symmetry

5. Y – Symmetry

Figure 4.2 shows the drawings of the current tunnel with the test section. Figure 4.3 shows the grid for the current tunnel along with the boundary conditions.

Above flow problem was solved to get the pressure data on the wall and the floor. The goal was to compare the results obtained by CFD to pressure data obtained by experimental methods. To record pressure data on the floor and wall of the tunnel following procedure was employed.

Pressure data was obtained at every 15.24 cm (6 in) of the tunnel wall and floor starting from the inlet. Data was recorded for a length of almost 18.3 m. A pin hole was made on the vinyl tubing (0.04 mm. diameter) with one end connected to the pressure sensor and the other end was a closed end. To keep the tubes together they were taped on to the thin aluminum sheet which in turn was taped to the wind tunnel wall/floor. Sample images with the vinyl tubes taped to the floor are shown in Figure 4.4. Figure 4.4 (a) shows vinyl tubes taped on to the floor and Figure 4.4 (b) shows vinyl tubes taped on to the wall of the modified wind tunnel.

A comparison of experimental pressure data (Pexp) to the computations (Pcompu.) is given in Fig. 4.5 Also shown are the simple 1-D theoretical results, both incompressible (Pincomp.) and compressible (Pcomp.)]. The 1-D incompressible theory was based on conservation of mass and Bernoulli's equation given by:

$$p_1 + \frac{1}{2}\rho v_1^2 = p_2 + \frac{1}{2}\rho v_2^2 \qquad (4.1)$$

The 1-D compressible is given by the equation:

$$\frac{p_0}{p} = \left(1 + \frac{\gamma-1}{2} M^2\right)^{\frac{\gamma}{(\gamma-1)}} \tag{4.2}$$

Figure 4.6 shows the comparison of pressure data on the wind tunnel floor. The dip in the plot is the test section region where the pressure is almost constant as expected. The pressure decreased in the inlet, remained constant in the test section and finally increased in the diffuser section. The pressure data for all methods fell on top of each other as shown. This exercise ensured that the boundary conditions used in FLUENT gave right results.

Presented in Fig. 4.7 is a comparison of the CFD results and the 1-D theory for the reduced 2.1 m x 2.1 m (7 ft x 7 ft) test section. As shown in the plot, they agreed very well. Figure 4.8 shows the pressure data on the wall as obtained by CFD (Pcomp) and the compressible 1-D calculations (Pcompr). As shown in the plot they both match well. These results demonstrated that the test section flow was uniform and the static pressure was expected to be 50 psf, which was used for structural design.

4.1.2 Mechanical Design

In a similar test section reduction of the Orin Nicks Wind Tunnel, Noak and Norton[39] constructed a set of inserts from wood. However, for the present DSF facility, large loads static pressure loads, as well as large unsteady wing loads (described later) were expected. Hence, the wind tunnel inserts were made from a steel frame and aluminum plate skin structure. Type 5052 AL was chosen for cost reasons. Detailed load analyses were performed using the stress analysis program CosmosX, which is part of the

autocad program SolidWorks program. A factor of safety of 5.0 was chosen for all designs. Thus, the design load was set to 12,000 Pa (250 psf). The dynamic loads are described in Section 4.2.

Looking up stream, the left side of the wind tunnel insert consisted of six panel structures. All of the panels were made from steel frames with AL 5052 sheets screwed (10-32 steel screws) to them to from the wall. Shown in Fig. 4.9 is a drawing of a panel. The frame for each panel was made from 5.08 cm x 2.54 cm (2 in x 1 in) C-channels. The exception being the middle panel (3rd) frame which was made out of 12.70 cm x 4.45 cm (5 in x 1.75 in) C-channel. This frame was the primary support for the wing. The aluminum plate thickness was 4.8 mm (3/16 in), which was selected to withstand the test section suction pressure with minimal displacements.

The 3rd panel holds the wing and encounters the large unsteady load. Hence, to transfer this load to the wind tunnel structures and eventually to the concrete structure underneath, the 3rd panel was made stronger. The panels were inserted into the tunnel one at a time. The panels were then all bolted together using 1.27 cm (½ in) steel bolts. The hole-pattern of the C-channel is shown in Fig. 4.9. The 3rd panel C-channel (Figure 4.10) had more holes as this frame is bolstered by additional structures (Figure 4.11).

Special care was taken to design the additional structures shown in Figure 4.11. There was an 20.32 cm x 20.32 cm x 10.16 cm (8 in x 8 in x 4 in) block used to hold top structure (NDSP3-Ti)[1] and the bottom structure (NDSP3-Bi) together. The block acts as a bearing housing. The shaft of the wing went through this bearing as shown in Figure

---

[1] Structure identification number defined during the design construction of the facility.

35

4.12. The design of the wing along with the shaft is described later in the chapter. In the structures NDSP3-Ti and NDSP3-Bi, the smaller I-beams were welded to the larger I-beam at angle of 45° as shown. The bottom structure (NDSP3-Bi) was welded to the steel frame of the 3rd panel as shown in Figure 4.12. The top structure (NDSP3-Bi) was screwed to the steel frame so that it can slide up and down for the convenience of installing the wing. The bearing was set in place in the bearing housing. Depending on the load acting on the shaft of the wing due to lift and drag, the bearing was chosen to have a minimum factor of safety of 5. Taper roller bearing was chosen as it could handle the maximum load for the fixed inner diameter (ID) of 3.05 cm (1.5 in). Once the block was set in place between NDSP3-Bi and NDSP3-Ti and bolted, 4 threaded rods [2.54 cm (1 in) diameter and 60.1 cm (2 ft long)] were used to further secure them as shown in Fig. 4.12. The right wall was built exactly the same as left wall except for optical access. Presented in Fig. 4.13 is a view of the additional structures from inside of the modified wind tunnel.

Provisions were made on the left wall of the modified wind tunnel to have glass windows in order to perform Stereo Particle Image Velocimetry (SPIV) experiments in the future. A door was made on the 6th. panel of the left wall. Adjustable vents were included on both the walls to control the pressure inside the wind tunnel. Figure 4.14 shows the glass windows, structures to hold the wing, vent and the door. A circular section was cut to make an optical glass window on the right wall to perform 2D Particle Image Velocimtery (PIV) experiments, which was used in the present experiments.

Figure 4.15 shows the optical glass window for 2D PIV experiment. Figure 4.16 shows the optical glass window with the camera acquiring images during the experiment.

A new steel frame of roof was made of 7.62 cm x 6.35 cm (3 in x 2.5 in) steel I-beams. This roof was designed to transfer the tunnel loads to the support structure. The design of the roof is shown in Figure 4.17. The 5052 AL sheets were bolted to the roof using 10-32 screws. A section of the roof was fit with a Plexiglas window. The PIV laser was directed through this window on to the wing. The grey frame around the Plexiglas was made out of AL 5052. The roof was bolted to the side walls of the modified wind tunnel. Thus the roof was set in place as shown in Figure 4.18.

The inlet of the wind tunnel insert was a curved section that mated the reduced test section width to the original tunnel contraction. Templates were constructed to define the shape as shown in Figure 4.19. The actual structure was constructed from a formed steel frame and 1/8th thick aluminum plate. The steel frames were made from 2.54 cm x 1.27 cm (1 in x ½ in) C-channel. The frame was anchored to the concrete contraction of the current wind tunnel. Figure 4.19 – 4.23 show the sequence of building the inlet. For inlet section 8-32 screws were used to attach aluminum sheet to the frame in stead of 10-32 screws as the sheet was thinner. All of the screws were countersunk.

The final section of the modified wind tunnel was the diffuser section. As was done for inlet section, the diffuser section mated the end of the test section to the existing diffuser. The diffuser was anchored to the concrete diffuser. Unlike the inlet section, the diffuser walls were straight. The diffuser was arbitrarily selected to be 3.05 m (10 ft) long. The frame was fabricated from 2.54 x 1.27 cm (1 in x ½ in) thick steel C-channels

with 3.18 mm (1/8 in) aluminum sheet screwed on to the frame. Figure 4.24 shows the left diffuser wall.

Vortex generators were used at the end of the test section to help minimize diffuser separation. The Vortex generators help in mixing the high momentum fluid away from the wall with the low momentum fluid near the wall. The present vortex generators were built to the shape of NACA 0012 profile and screwed to the test section as shown in Figure 4.25.

The next step was to run the tunnel and verify the test section Mach number. Figures 4.26 (a) and (b) show the plots of Mach number and static pressure in the modified 7 ft x 7 ft tunnel. With this configuration, the peak Mach number was 0.28. This was limited by both diffuser performance and tunnel power.

The original goal was a freestream Mach number of 0.4. Power calculations (Fig. 4.27) demonstrated that a smaller test section was required to achieve this speed with the available 1200 kW of propeller power. Furthermore, the diffuser included divergence angle also needed to be reduced to approximately 10°, which translates into 10 – 12 m long achieve efficient diffusion at mach 0.4. A second reduced area test section (5 ft x 7ft) was constructed, and the diffuser will be installed during the follow-on project.

To achieve a 1.5 m x 2.1 m (5 ft x 7 ft) test section, inserts were designed to lower roof and raise the floor each by 1.0 ft. The design included detailed load calculations to size roof and ceiling inserts. As shown in the Figure 4.28, 7.62 cm x 7.62 cm (3 in x 3 in) C-channels were bolted to the steel frames of the 7 ft x 7 ft modified wind tunnel test section. For the floor, 4 panels were designed and fabricated. These panels were bolted

together. Each panel had a steel frame made out of 5.08 cm x 2.54 cm (2 in x 1 in) C-channel. Aluminum 5052 sheets [4.8 mm (3/16 in)] thick were screwed on to them as was done for the wall. These 4 panels were slid through the gap between the C-channels shown in Figure 4.29. The floor of the 5 ft x 7 ft test section is shown in Fig. 4.30. The roof was designed and fabricated as was done for the floor. The only difference was the roof was designed to have a glass window through which the laser can be shot on the test section model. Figures 4.30 – 4.33 show the floor, roof, right side view and left side view of the 5 ft x 7 ft test section, respectively. Figures 4.34 – 4.40 show images of the modified wind tunnel insert (7 ft x 7ft). After the installation of the modified wind tunnel all the seams were taped.

4.2 NACA 0012 Wind Tunnel Model

A NACA 0012 airfoil was selected for the current research. This airfoil is a good compromise between high maximum lift, low pitching moment and high drag divergence Mach number, and this airfoil has been the subject of numerous previous studies. The choice of this airfoil was driven by the fact that numerous researchers have used this profile, which translates into an available database for comparison.

4.2.1 Mechanical Design

The airfoil chord length was selected as 18 in and the model spanned the wind tunnel. A clearance of 3.2 mm (1/8 in) was maintained between the wing and the wind tunnel wall on both sides. Hence the wing was designed to have a span of 2.1 m (6 ft 11¾ in). The maximum flow blockage at the highest planned angle of attack with this arrangement was approximately 7.3%. An 11.4 cm (4.5 in) section of the airfoil was

machined from Plexiglas. The Plexiglas piece was 2.54 (1 in) wide. Plexiglas is an optically transmitting material. Hence the laser sheet passes through the Plexiglas piece and minimizes any reflection issue during Particle Image Velocimetry (PIV) experiments. A shaft ran through the quarter chord of the wing. One end of the shaft was held by the hydraulic actuator to flap the wing at the desired frequency. Quarter chord point was the choice because the coefficient of aerodynamic moment C_m created at this point is of the order of $0 \sim 0.1$. Hence the wing was flapped with minimum power requirement.

As mentioned in the above paragraph, a shaft was designed to run through the quarter chord of the wing, which was supported by bearings at both the ends. Stainless steel was chosen due to its high strength. The following calculation procedure was used to design the shaft:

$$L = C_L Qcb \qquad (4.3)$$

where, C_L = Lift Coefficient = 1.6 (for a dynamically stalled NACA 0012); L = Lift acting on the airfoil, Q = Dynamic Pressure [= 13,400 Pa (280 psf)]; c = Chord length of the airfoil [= 0.457 m (1.5 ft.)], and b = Width of the airfoil [=2.1 m (6 ft 11 ¾ in)]. With these values, L = 20,200 N (4540 lbf). A factor of safety 4 was chosen for all design purposes. Hence, the design load was estimated as $F = 4L$ [= 80,800 N (18,200 lbf)]. The minimum shaft diameter was based on the allowable shear stress of stainless steel of 2.3 x 10^8 Pa (33,000 psi). The shear stress is given by $\tau = F/A$, where $A = \pi d_s^2 /4$ and the d_s is the shaft diameter. For the present design the minimum shaft diameter for failure was 2.1 cm (0.84 in). However, the shaft diameter was set at 3.81 cm (1.5 in) to maintain the maximum deflection to less than 6.35 mm (¼ in).

The thickness distribution for the NACA 0012 is given by the following equation.

$$\pm y_t = \frac{t}{0.2}\left(0.29690\sqrt{x} - 0.12600x - 0.35160x^2 + 0.28430x^3 - 0.10150x^4\right) \qquad (4.4)$$

where y_t is the thickness of the airfoil, t = maximum thickness expressed as a fraction of the chord, x is the axial coordinate along the airfoil center line per c.

The numbering system for NACA wing sections of the four digit series is based on the section geometry. The first integer indicates the maximum value of the mean-line ordinate y_t in percent of the chord. The second integer indicates the distance from the leading edge to the location of the maximum camber in tenths of the chord. The last two integers indicate the section thickness in percent of the chord. Thus the NACA 0012 wing section has 0 percent camber at 0.0 of the chord from the leading edge and is 12 percent thick.

Airfoil stress analysis was performed with the finite elements program ABAQUS. The airfoil cross-section was created using the profile equation 4.4 and then was extruded to the full span. The points on the profile were joined by 18 straight lines so that the airfoil surface had 18 regions both on the upper and lower surface to apply the varying pressure as the load. The loading[40] (varying pressure) is shown in Figure 4.41. Table 4.1 shows the other input parameters used in ABAQUS.

In terms of boundary condition, the shaft was pinned at the ends and was constrained from having any movement with respect to the airfoil by using tie constraint condition.

Figure 4.42 – 4.44 show the contour plots of deflection, reaction forces and stress acting on the wing and shaft. As can be seen in these plots, the deflection, stress and reaction force acting were well within the design limits.

Table 4.1 Input parameters in ABAQUS[1]

Input Parameters	Wing	Shaft
Material	Aluminum	Stainless Steel
Density	5.28 slug/in^3	14.74 slug/in^3
Poisson's ratio	0.33	0.30
Young's Modulus	1.0×10^7 Psi	2.1×10^7 Psi
Element type	Hex, independent meshing, Linear 3D stress	Hex, independent meshing, Linear 3D stress

[1]English Units were used in ABAQUS

The NACA 0012 wing used in the current research was built in two halves. Dowels pins [11.43 cm (4.5 in) long and 4.8 mm (3/16 in) diameter) were used to prevent any axial motion of the shaft as shown in Figure 4.45. The detailed drawing of the wing with the screws and the shaft attachment dowel pins is given Fig. 4.45. The cross sectional drawing of bottom half of the wing is shown in Figure 4.46. The two halves are screwed on to each other using 53 screws. Stress analysis was done on these screws (3/8 in diameter). The wing was counter sunk to accommodate the nuts and the bolt heads. The empty area in the counter sunk portion is filled with putty. Finally the wing surface was polished to have a smooth surface as any unevenness on the surface would trip the boundary layer and eventually affect the flow field. The length of the shaft was 3.05 m (10 ft). Approximately 0.55 m (1.813 ft) of the shaft extends out on both sides of the wing. The shaft is concentric with the quarter chord of the wing as mentioned earlier. Figure 4.47 shows the wing with the shaft and the Plexiglas piece.

The final NACA 0012 wing used in the present research is summarized below:

Chord of the wing	=	0.457 m (18 in)
Span of the wing	=	2.13 m (83.75 in)
Weight of the wing	=	104 kg (230 lb)
Mass Moment of Inertia of the wing =		1.79 N-m (1.32 ft-lb)

4.3 DSF Hydraulic Actuation Apparatus

A hydraulic actuation apparatus was designed to pitch the airfoil about ¼-line. The advantage of hydraulic system over the originally proposed electric motor system was safety, where the electric motor system would require a large flywheel. A Parker Hannifin system was purchased from TEX A DRAULICS.

The hydraulic pump was driven by a 29.8 kW (40 HP) electric motor. The flow was 36.1 GPM @ 1800 rpm. The hydraulic reservoir held 80 gallons of *Chevron Rykon aw ISO 46* hydraulic fluid. The maximum pressure of the system was 20.67 MPa (3000 psi). A suction strainer/filter was used to keep the oil free of impurities before it goes to the accumulator bladder. The unit also has an oil level gauge with thermometer. The accumulator had a 9.46 liter (2.5 gallon) storage capacity, and was connected to the main pump reservoir with high pressure hoses [29.3 MPa (4250 psi). The accumulator maximum pressure was 20.67 MPa (3000 psi). During operation, the accumulator supplied the required amount of hydraulic fluid through the servo valve. During downward movement of the piston, oil returned to the accumulator through a similar high pressure hose.

A Parker Hannifin servo valve controlled the amount of hydraulic fluid required for the pitching of the airfoil. Hence, one end of the valve was connected to the inlet of the hydraulic actuator and the other end to the outlet of the actuator as shown in Figure 4.49. An algorithm was developed to control the opening/closing of the valve to allow required flow rate of hydraulic fluid in order to move the actuator.

The hydraulic valve was operated by a PID controller program implemented in RMCWin software. RMCWin software is RMC100 motion controller software by Delta computer systems. The RMC100 is a modular, high performance motion controller appropriate for a wide range of industrial applications for position and velocity control. Judicial choice of the Proportional, Integral, Differential gains, extended feed forward/backward and acceleration feed forward/backward make sure that the target command follows the actual command. An algorithm was developed to control the opening/closing of the valve to allow required flow rate of hydraulic fluid in order to move the actuator.

The final major component of the actuation system was the hydraulic cylinder with actuator as shown in Figure 4.50. The inlet port, which was connected to the servo valve, was on the bottom of the cylinder. The outlet of the cylinder, which was also connected to the servo valve, was on the top of the cylinder.

A moment arm acted as a link between the wing and the hydraulic actuator. Hence, the linear motion of the actuator was converted to the pitching motion of the wing. The linear motion of the hydraulic actuator was then converted to sinusoidal motion of the airfoil.

The hydraulic cylinder actuator was connected to a moment arm by a clevis as shown in Figure 4.51. The wing shaft was connected to the other side of the moment arm by a power lock. The power lock is a keyless locking device used to transfer torque. The inner diameter of the power lock matched the 3.81 cm (1.5 in) diameter of the stainless steel shaft. With this configuration of hydraulic system a range of 0° - 20° of the airfoil

motion can be achieved at a maximum frequency of 12-15 Hz. The hydraulic cylinder had a bore of 6.35 cm (2.5 in). The actuator diameter was 2.54 cm (1 in). The range of linear motion of hydraulic actuator was 3.81 cm (1.5 in). However for the current test matrix the actuator was operated within a distance of 1.27 cm (0.5 in). A linear position sensor (MTS temposonics sensor) was mounted to the bottom end of the actuator as shown in Figure 4.52. This sensor provided accurate non-contact position sensing in a wide array of output configurations. With this specification, the hydraulic actuator could sustain 6000 lbs of force.

To work out the algorithms used to operate hydraulic valve, it was decided to simulate the pitching of the wing without the wind load. Hence, a stand was made as shown in Figure 4.53. As a first step, only the shaft was loaded. Once the program worked well with that the wing was loaded and the program was tweaked to produce the right result. This exercise helped to build experience with the general dependence of gains on loads acting on the piston. Hence, with the wind load, it was an easy task to tweak the gains so actual command precisely followed the target command. This simulation also helped in building some additional structures required to prevent vibration in the wing and also in designing the stand for the hydraulic cylinder as shown in Figure 4.54.

One of the major advantages of simulating the pitching experiment without wind load was the discovery of a vibration issue of the shaft. This vibration propagated to the wing and could have caused a failure of the wing. Hence, an additional support was built to hold the actuating end of the shaft as shown in Figure 4.55. The shaft

goes through the center steel block as shown. A lock collar was used at the end of the shaft to prevent any axial movement. The top and bottom I-beam structures were bolted to the modified wind tunnel steel frame. Thus, the load was transferred to the structure. This additional structure eliminated vibration in the shaft and also bolstered the support. Also, an additional structure was designed and built to bolt the hydraulic actuator support as shown in Figure 4.56. This structure helped in transmitting the unsteady load to the large C-channels supporting the 7 ft x 10 ft low speed wind tunnel as shown. Figure 4.57 shows the additional structures explained above. Given in Fig. 4.58 is an image of the hydraulic actuator drive system placed in the ready room along with the computer that was used to control the program. Presented in Fig. 4.59 is a comparison of the target sine wave to that measured during operation with the above mentioned LVDT. As indicated, the system worked very well.

4.4 Wing Angle Calibration and Coordinate System

The wing position (angle-of-attack) was related to the hydraulic piston motion through a linear calibration (see Fig. 4.60). The average variance between the calibration and the measured angle was 0.2 deg. The angle resolution for the control system was 55 counts per degree, which translates into steps of 0.018 deg.

The wing coordinate system for the experiments was defined as follows. The origin was fixed at the wing ¼-chord; x was defined as pointing in the upstream direction parallel to the tunnel floor; y was defined as vertically up, and z completed the right hand system.

Chapter 5

EXPERIMENTAL APPARATUS AND DATA REDUCTION TECHINIQUES

The leading-edge region of the flowfield was documented using Particle Image Velocimetry (PIV). A detailed description of the PIV system is presented below. This is followed by a summary of the remaining instrumentation used to provide the tunnel flow conditions. The uncertainty analysis results are presented in the last section.

A new film, developed by ISSI, Inc., was tested to measure the surface shear stress and pressure. The S3F methods are proprietary to ISSI. The S3F data were too preliminary to draw conclusions. Hence, only a brief overview of the system with example results for the flapping wing is described in the last section of this Chapter.

5.1 Particle Image Velocimetry

5.1.1 Overview of the Operating Principles

Particle Image Velocimetry (PIV) is a non-intrusive diagnostic technique to measure the velocity in a plane. The technique has emerged into one of the most popular methods to quantify fluid flow. The primary reason is that PIV provides detailed instantaneous velocity measurements on plane. Both 2-D and 3-D measurements are possible on the measurement plane. For the present study, PIV was used to document the

field near the leading edge during dynamic stall of a NACA 0012 airfoil operating the Dynamic Stall Facility described in the previous Chapter.

In summary, the PIV technique measures the velocity of a fluid element indirectly by measuring the velocity of tracer particles seeded into the flow. A schematic of a typical wind tunnel application is shown in Fig. 5.1. The tracer (or seed) particles are usually illuminated by a series of two short pulse lasers, separated by a specified time increment. The light scattered by the particles from the two pulses is recorded. Charge-Coupled Devices (CCD) cameras are generally used to record the two images. For most applications, interline transfer cameras are used, where both pulses are independently recorded on two separate images acquired on the same CCD in succession. The displacement of particles between the two images and the time increment between the light pulses determine the velocity of the flow.

Qualitatively three different types of image density can be distinguished. Low image density (Fig. 5.2 a) is used for Particle Tracking Velocimetry (PTV), where individual particles are tracked. In the case of a medium density image (Fig.5.2b), the individual particles can be detected. However, it is not possible to identify image pairs by visual inspection of the recording. For this case statistical correlation methods are used. This case has been termed PIV. The advantage of PIV over PTV is the better spatial resolution per image. In the case of high particle density (Fig. 5.2 c) it is not even possible to detect individual images as they overlap in most cases and form speckles. This is called Laser Speckle Velocimetry (LSV). LSV requires large seed volumes, which was not available for the present study. Hence, PIV was used.

To evaluate the velocity, a digital PIV recording is divided in small sub-areas called interrogation areas. The local displacement vector for the images of the tracer particles of the first and second illumination is determined for each interrogation area by means of statistical auto- or cross-correlation methods. The underlying assumption is that all of the particles within one interrogation area have moved homogeneously between the two illuminations. The projection of the vector of the local flow velocity into the plane of the light sheet (2-component velocity vector) is calculated taking into account the time delay between the two illuminations and the magnifications at imaging. The process is usually performed in a sequence starting with relatively large interrogation windows and then subsequently reducing the size of the window. The larger windows contain more samples and thus have higher correlation coefficients.

5.1.2 Texas A&M University PIV System

The PIV system used in the present experiment is an in-house designed system. A description of the system is given below.

A New Wave Solo 120 XT Dual Head Nd:YAG Laser (frequency doubled to $\lambda = 532\,\text{nm}$) provide the two laser pulses. The available repetition rate is 15 Hz. Each laser head has a maximum energy output of 120 mJ at 532 nm. The pulse width is 4 ns with an $\pm 1\,\text{ns}$ jitter. The beams emerge with parallel polarization. The polarization for one of the beams was rotated 90 degrees with a ½-wave plate. The plate is crystal quartz optic designed to differentially retard the phase of polarized beam. The beams were them overlapped in space with a high energy polarizing cube beam splitter that provides efficient narrow band polarization. The polarizer consists of a pair of precision right-

angle prisms optically contacted together and has a damage threshold up to 10 J/cm^2. This process provided two coincident beams; one with parallel polarization and the other with perpendicular polarization.

The laser system and corresponding optics were mounted onto the roof of the wind tunnel as shown in Fig. 5.3. The laser beams were guided into the test section using 90^0 prisms constructed of BK7 glass with AR coatings. A laser sheet (1.5 to 2 cm wide) was formed on the model using a BK7 Plano-concave cylindrical lens. A BK7 focusing lens with a focal length of 900 – 1000 mm is used to focus the beam so that the waist is located just above the test section model, precisely just above the Plexiglas portion of the NACA 0012 wing. The thickness of the laser sheet was less than 1.0 mm.

Vibrations were present when the wind tunnel ran at high-speeds. To stabilize the beans, two 10.2 cm x 10.2 cm (4in x 4 in) I-beams were used as shown in Fig. 5.3. The two I-beams run perpendicular to the direction of freestream and spanned across the wind tunnel test section. They were supported onto the current wind tunnel concrete roof. Vibration isolation material (rubber pads) was used between the I-beams and the concrete. Four sand bags were placed on the I-beams for further isolation of vibration. This setup proved to be effective to obtain a stable laser beam.

Data were were acquired with two cameras: a Cooke Corporation PCO 1600 Camera, and LaVision Flowmaster Camera. This was a high dynamic range (14bit), thermoelectrically cooled (to -20 deg C) interline transfer CCD camera with a 1600 x 1200 pixel array resolution. The camera has a Nikon f-mount for lenses. For the present set of experiments an exposure time of $5\mu s$ and trigger delay time of $10\mu s$ was used. The

interline transfer rate is sufficient for delays down to 300 nsec. The camera frame grabbing software was Camware version 2.13. A Nikon 70 – 300 mm lens was used to focus the camera onto the illuminated particles. The LaVision PIV camera was UltraSpeedStar Camera. This camera had a 12 bit, 1280x1024 pixel array. This camera was control with the LaVision DaVis software package.

The camera was mounted to an H-shaped stand was that made from aluminum rails (Fig. 5.4). The camera was mounted on an extension bar which in turn was attached to the middle rail using a mounting plate. The camera was supported by cylindrical posts which in turn were attached to the extension bar as shown in the Fig. 5.5. Mounting camera on the extension bar helped in moving it in the direction perpendicular to the flow depending on the requirement. For example, for a wide angle view the camera was moved away from the test section, and on the other hand for the zoomed in high resolution data, it moved in close to the test section wall as shown in Figure 5.5. The mounting plate can be slid on the middle rail thus providing movement of the camera in the direction of flow. Two cylinders were inserted into the middle rails at both ends. The middle rail was attached to the cylinders (running inside the rail) and to the side rails with the help of set screws and mounting plates respectively. This arrangement in turn provided rotational degree of freedom for the camera. Thus, the camera had three degrees of freedom for alignment.

The synchronization of the camera trigger, laser Q-switch, laser flash lamps to the wing motion as indicated from the signal from the hydraulic actuator were all controlled by a Quantum Composer Model 9618 pulse generator. The program ensured the flapping

motion of the airfoil, laser sheet and the camera were phase locked to acquire images at a particular angle of attack. The pulse generator had 8 channels with 100 ns resolution (jitter < 5 ns).

The tunnel was seeded by MDG Max 5000 Fog generator using MDG neutral fluid. This has a fog output of 10000 ft^3/min. Fluid consumption was 2.5 liter/hr. at 40 PSI at full volume. The reservoir capacity was 0.66 US gallons. It produced pure white particle diameter of 0.5 to 0.7 μm. The 3 dB frequency response of these particles was estimated at 200 kHz.

5.1.3 Surface Reflections

Bright laser reflections from a solid (reflective) surface masks the Mie scattering signal from the small seed particles (0.5 – 0.7 μm, here). An additional complication associated with the laser reflection from the surface is image blooming, which a situation where neighboring pixels are saturated with excess charges producing a white band in the image. A balance in the laser power is required optimize scattering from the particles while minimizing blooming.

To address the reflection challenge, a 10.2 cm (4.0 inch section) of the airfoil leading edge was machined from Plexiglas (optically transmitting material). The notch for the Plexiglas insert is visible near the center of the airfoil Fig. 4.47. The Plexiglas was polished to a clear transmitting surface with Buehler Brand polishing compound (20 micro-inch, followed by 5 micro-inch). This Plexiglas insert transmitted approximately 92% of the laser energy. The purpose of this section was to minimize laser sheet reflections. To that end, the portion of the wing underneath the Plexiglas was painted

black so that laser sheet would not reflect back. The remaining 8% still masked the data below approximately 1.5 mm. Thus, the Plexiglas was coated with a fluorescent (Rhodamine) paint capable of absorbing up to 99% of the incoming light at 532 nm and emitting the light at approximately 690 nm (see Fig. 5.3). The second benefit was that the emitted light was diffuse, compared to the specular laser reflection. Lastly, the airfoil was painted black approximately one foot on each side of the Plexiglas (see Fig. 5.3) to minimize additional light reflections. This combination of measures significantly reduced the reflections, and data were acquired as close as 0.5 – 1.0 mm from the wall.

5.1.4 Data Reduction

Each PIV sample consisted of two images; these were labeled image A and image B. For present study, 1000 to 1300 image pairs (samples) were acquired at each angle of attack to assure statistical convergence of the mean and second order statistics. These images were processed as described below.

As described above, considerable effort was put into minimizing vibrations. However, the remaining vibration had an adverse affect on the images. Specifically, the camera vibrations resulted in the airfoil position "jumping" around from one image to the next. The magnitude of the airfoil jumps was approximately 10 to 15 pixels. Thus, the first step in the data analysis was to "de-jitter" the airfoil images. To accomplish this task, an in-house MATLAB code was developed to locate the airfoil edge on each image. All of the images were translated to align all of the airfoil edges with the first image in the sequence. The airfoil position was aligned to within 4 pixels.

The second step in the data analysis was performed to further minimize the reflection effects. Specifically, an in-house MATLAB code was developed average all the shifted image A's and images B's. The averaged image was then subtracted from each image. This algorithm worked very well as shown in Fig. 5.6. Given in Fig. 5.6(a) is an original instantaneous image before subtraction. The averaged image is shown Fig. 5.6(b), and the image after subtraction is given in Fig. 5.6(c). The contrast in the last image was adjusted to better show the particles.

Velocity fields were created by calculating the displacements of particle ensembles from consecutive images using Innovative Scientific Solutions' Digital Particle Image Velocimetry (DPIV) 32-bit Analysis Code[40]. A four-step adaptive correlation calculation using successive interrogation spot (square) sizes of 128x128, 64x64, 32x32, 16x16 pixel respectively with a 75% overlap was used to determine velocity vectors. The images were correlated to the grid. Hence the grid option was 'on' in the DPIV program. With these settings, data were acquired in 4 pixel increments, which corresponded to approximately 0.06% of the airfoil chord or 0.25 mm. This "hyper fine mesh" is shown in Fig. 5.7. With this mesh, there were nominally 100,000 velocity vectors in the region of interest.

In order to enhance the intensity of correlation peaks relative to random noise, a correlation multiplication process filter with all four correlation maps was turned on. A consistency post processing filter was turned on to improve the adaptive correlation calculation during the first, second, and third steps and eliminated incorrect vectors during the fourth step. The Consistency filter is the parameter which searches for a

correlation peak around another within a radius of 1 unit. Hence in the settings for consistency filter in DPIV program, the minimum particle was set to 2. The radius was also set to 2, which corresponded to one unit to the left and one unit to the right. A filter refinement study was performed to ensure that the results were independent of the filter settings. As a result of the refinement study, the nearest neighbor option in the DPIV program was turned off as option on did not affect the results and consumed significantly more computation time. An example comparison is shown in Figs 5.8, where Fig. 5.8(a) corresponds to the case where the nearest neighbor option was off and 5.8(b) corresponds to the case where it was on. In this figure, the contour plot of the transverse velocity is shown for the case where the wing was at an angle of attack of 14° during the pitch up stroke; the reduced frequency was k=0.18, and the Mach number was 0.2. The results in Figs. 5.8(a) and (b) are indistinguishable.

A grid refinement study was also performed between 3 iteration and 4 iterations as shown in Figs. 5.9(a) and (b), respectively, where contour plots of Mach number are compared. The mesh generated with 3 iterations is named as "coarse" mesh. The correlation to the grid with hyper fine mesh took ~48 more hrs to process than did the coarse mesh. The differences were modest, where the maximum difference was 0.02 in Mach number. The small number of levels used the contours in Fig. 5.9 exaggerated the difference. The hyper fine mesh was chosen for analysis as the result was resolved to a higher order. In the DPIV program, the vector display option was turned off while processing to decrease the processing time. The data reduction analyses to compute the vector fields from the PIV images required 3000 CPU hrs, which was distributed over six

personal computers running in parallel. An output file consisting of instantaneous velocity data was stored in an ASCII file format for each image pair.

First and second order turbulent statistics are created using an in-house MATLAB code that ensemble averaged the velocity vector fields. In order to minimize the effect of fluctuations in the wind tunnel conditions on statistics, the program binned the average velocity data and computed the fluctuating velocities relative to the average velocity in the corresponding bin. The normalized binned data were then averaged. The equation for the bin mean velocity is given below, where n is the number of samples per bin, and J_{max} is the total number of bins.

$$U_{bin,j} = \frac{1}{n} \sum_{i=(j-1)n+1}^{j \cdot n} u_i, \quad j = 1 \dots j_{max} \tag{5.1}$$

The computed mean velocity is then the ensemble average of the bin velocity:

$$U = \frac{i}{J_{max}} \sum_{j=1}^{J_{max}} U_{bin,j} \tag{5.2}$$

The fluctuating statistics were computed as

$$\overline{u'u'} = \frac{1}{N-1} \sum_i^N \left(u_i - \overline{u}_{bin,j} \right)^2$$

$$\overline{v'v'} = \frac{1}{N-1} \sum_i^N \left(v_i - \overline{v}_{bin,j} \right)^2 \tag{5.3}$$

$$\overline{u'v'} = \frac{1}{N-1} \sum_i^N \left(u_i - \overline{u}_{bin,j} \right)\left(v_i - \overline{v}_{bin,j} \right)$$

where $1 \le i \le n \Rightarrow j = 1,\dots,(J_{max}-1)n+1 \le i \le J_{max} n \Rightarrow j = J_{max}$. The z–component of the vorticity and the xy-component of the strain tensor were calculated as follows

$$\omega_z = -\left(\frac{du}{dy} - \frac{dv}{dx}\right)$$

$$S_{xy} = \left(\frac{du}{dy} + \frac{dv}{dx}\right)$$

(5.4)

The strain rates were computed using second order central differences. The static temperature and Mach number were computed assuming an adiabatic flow. Following equations are used to calculate the Mach number. The static temperature is given by $T = T_t - (u^2 + v^2)/2C_p$, where T_t was the temperature in the tunnel stilling chamber. With the static temperature, the speed of sound, a, was computed assuming a thermally perfect gas, and the Mach number was computed as $M = V/a$, where V is the magnitude of the measured velocity.

Both the axes are normalized with the chord length c. The velocities, normal and shear stress components are normalized with the freestream velocity.

In the post processing code, a 3σ filter was used to discriminate erroneous data points. The 3σ retained 98% of the vectors, where a 2σ retains 92%. The choice of the filter setting was made based on a filter refinement study, which are summarized in Figs. 5.10. The flow conditions were the same as those described above for Fig. 5.8. Shown in Figs. 5.10 (a) are contour plots of V velocity and number of velocity vectors remaining after the filter used in the averages, respectively, for the 3σ filter. Given in Figs 5.10 (b) are the same data with 2σ filtering. The peak difference between the two datasets was less than 3%. The 3σ filtering was used for the present study as it retained the larger number of data points.

5.2 Tunnel Flow Freestream Condition Instrumentation

Test section conditions were measured using a Druck DPI 203 digital pressure gage and an Omega Model 199-temperature gage. The Druck pressure gage measures the set dynamic pressure within ±0.08% of full scale, and the Omega thermometer is accurate to within ±0.2 deg C. A Mensor 14500C digital barometer was used to read the atmospheric pressure, and it is accurate to within ± 4.0 Pa. All of these measurements were read with the motion controller computer.

In addition to the wind tunnel instrumentation, the freestream conditions for the 7 ft x 7ft test section were also examined with the present PIV system. The wing was in the tunnel during the tests, but the angle of attack was set to zero. The mean velocity agreed with the tunnel instrumentation to well within the PIV measurement uncertainty. The freestream turbulence was found to increase from 2.0% at Mach 0.2 to 4.0% at Mach 0.28.

5.3 Uncertainty Estimates

The measurement uncertainties for the present study are summarized in Table 5.1, and were accumulated with a Euclidean (L_2) norm. The uncertainties in the freestream stagnation conditions include the transducer uncertainty. The position uncertainties were takes as the uncertainty in the airfoil edge, which was nominally 4 pixels after the de-jitter algorithm was applied. The angle-of-attack uncertainty was based on the calibration (described above). The relative position uncertainties used to compute the strain rates was equivalent to the actual position variance of the CCD array pixels, this uncertainty was assumed negligibly small. The calibration (or conversion) error was nominally 1.0%. The

uncertainty analysis of the PIV data (last four rows in Table 5.1) accounted for correlation mapping error and the conversion error from the physical length scale to the appropriate number of camera pixels. The estimated uncertainty in the statistical quantities was determined using a 95% confidence interval [Benedict and Gould (1996)]. The variance was determined assuming a normal distribution and a total of 1000 instantaneous velocity vector fields. The uncertainty in the production was the result of a combination of the uncertainties in position, the mean velocity and the associated finite difference scheme. The relatively large values of the fluctuating unsteady flow velocities in the separated regions resulted in the large PIV uncertainties listed in Table 5.1. These are the worst case results.

Table 5.1: Uncertainties

Variable	Error
P	1.0%
T	0.5%
U_{inf}	0.3%
x(mm), y(mm)	0.3
α (degree)	0.3
$\bar{u}$	2.0%
$\sqrt{\overline{u'^2}}$, $\sqrt{\overline{v'^2}}$	10.0%
$\overline{u'v'}$	20.0%
$P_{xx}/\bar{\rho}$, $P_{yy}/\bar{\rho}$, $P_{xy}/\bar{\rho}$	30.0%

5.4 Preliminary Assessment of the S3F Technique

At the time of this study, innovative Scientific Solutions, Inc. (ISSI) was developing a new film technology to directly measure both the surface pressure and surface shear stress during wind tunnel testing. This technology was evaluated during the present

dynamic stall study. The operating principle of the film is shown in Fig. 5.11. In general, the film was designed to deform under both shear and normal pressures. The deformation was recorded in two ways. First, the film was doped with particles which shift position when a shear load was applied. The PIV algorithms described above were then used to record this deformation. Second, the film was also doped with fluorescent molecule. The intensity of the fluorescence varied as the normal load varies the film thickness. The film composition and data reduction software is proprietary to ISSI.

The S3F film was evaluated during two series of dynamic stall tests. Since this was a new technique, it was difficult to predict a priori the correct thickness and stiffness of the film. A range of films were tested. However, most of the data were contaminated by film rippling under the harsh loads associated with the present tests. An example set of preliminary data is present in Fig. 5.12. Because the method is preliminary, no addition results were presented in this report.

Chapter 6

DATA REPOSITORY

The high-fidelity wind tunnel tests were completed in May, 2007. The DPIV data reduction step was completed in August, 2007; this step took ~3000 CPU hrs. The experimental data are available in electronic format. PIV movie sequences were also acquired for the first two cases listed in Table 1.1. These are also available in electronic format. Contact information for the PI is given on the Cover page.

An example set of high fidelity data is shown in Fig. 6.1. This figure provides an understanding of the quality and resolution of the data acquired in this study. The data plotted in this figure is for Case 1, where the Mach number was 0.2, the reduced frequency was 0.1, and the amplitude of the sinusoidal motion was 10 degrees. The angle of attack shown is 18 degrees during the upstroke motion.

As mentioned in the introduction, the present study focused on the leading edge region of the flow. A PIV photograph was overlain on the airfoil (approximately to scale) at the top of Fig. 6.1. The flow was from right-to-left. The second PIV image was included to show the magnitude of the flow unsteadiness, where the flow in the image on the airfoil was fully separated, and the flow in the second image appeared to have been attached. Thus, the separation point was moving in an out of the field of view.

Along middle row of Fig. 6.1 are example data;[2] these representative data include, moving from left-to-right, axial velocity (U/U_∞) transverse velocity (V/U_∞), axial turbulence intensity (σ_u), transverse turbulence intensity (σ_v), Reynolds shear stress $-\overline{u'v'}/U_\infty^2$ and the axial stress turbulence production (P_{xx}).[3] As indicated in these images, the flow was dynamically rich in both the mean and in turbulence statistics. The last row in Fig. 6.1 shows expanded views of σ_v and P_{xx}. Overlain on these is the measurement mesh. As indicated, even in the expanded view, the spatial resolution was very good.

Analyses of the acquired data were in-progress at the time of this writing. Hence, it was too early to draw flow field conclusions. A visual catalog of the data listed in Table 1 is given in Figs. 6.2 – 6.25.[3] Mappings similar to those in Fig. 6.1 were being made, at the time of this writing, for all of the conditions shown in Figs. 6.2 – 6.25. The properties under investigation include: the mean velocity, mean vorticity, mean strain, turbulence intensities, Reynolds shear stress, and turbulence production. In addition, detailed analyses of instantaneous snap shots were underway. The ongoing data analyses will be reported to the ARO through subsequent Technical Reports; specifically, the PhD

---

[2] The data were plotted using the Primary Variable contour type option in Tecplot. This is apposed to the more standard Flood option. Flooding resulted in smoothing of the data and blurring of the airfoil surface location. Flooding was not required for this study as all of the data were acquired on the hyperfine mesh, where the spacing between measurements was 0.06% of the chord (see Chapter 5, Fig. 5.7). Also, the high resolution contours were plotted using the continuous color spectrum as apposed to the banded approach. Both approaches are suitable, however, the banded approach was judged to de-emphasize the spatial resolution of the data.

[3] The plotted coordinate system was arbitrarily selected such that the leading-edge of the airfoil was located at $x/c = 0.25$ and $y/c = 0$. The corresponding mapping to the coordinate system in Fig. 1.1 is simple shift based on the angle of attack.

dissertation of Mr. Dipankar Sahoo, the student supported by this grant, and reprints of journal articles.

The images reported in this Chapter were limited to screen quality Portable Network Graphics (PNG) format. This was judged acceptable as these plots primarily serve to catalog the available data, which is available in full resolution electronically.

Chapter 7

CONCLUDING REMARKS

The primary objective of this research project was improved understanding of the fundamental vorticity and turbulent flow physics for a dynamically stalling airfoil at realistic helicopter flight conditions. To meet this objective, an experimental program using high-resolution Particle Image Velocimetry (PIV) was performed to provide an empirical characterization of the leading-edge (first 10-15% of the chord) flow structure. A dynamically pitching NACA 0012 wing operating in the Texas A&M University large-scale wind tunnel was studied. In conclusion, this research program was successful in completing the following tasks:

1. A new apparatus was designed and constructed for basic research studies of dynamic stall at realistic helicopter flight conditions. This included

    a. Large-scale modification to the Texas A&M University Orin Nicks Low-Speed Wind Tunnel

    b. Design and construction of a hydraulic actuation system for the large-scale (0.46 m chord, 2.1 m span) solid aluminum wing

2. Our PIV methods were refined to allow for spatial resolution of 0.25 mm (0.06% of the airfoil chord) and measurements to with 0.5 – 0.7 mm from the wing surface. This included

   a. Developing image processing techniques to minimize the effects of vibration

   b. Developing innovative methods to reduced reflections

   c. Optimizing the data processing routines to produce velocity vectors every 4 pixels (16 x 16 pixel interrogation windows with 75% overlap).

3. Extensive PIV tests focused on characterizing the leading edge flow structure were performed. A minimum of 1000 samples was acquired at each point. This translated into approximately 3 TB of optical data, which required 3000 CPU hrs to process. The processed results included planar contours of the mean velocity (*u*- and *v*-components), vorticity, strain rates, turbulence intensities (*u*- and *v*-components), the Reynolds shear stress, and production of the turbulent stresses (axial, transverse and shear). The test matrix included

   a. Case 1: Detailed leading-edge measurements during the up- and down-stroke a dynamically actuated NACA 0012 [$\alpha = 10 \pm 10 \sin(2\pi f t)$, k = 0.1] at M = 0.2 (Re = 2.0 million). Data were acquired in 2.0 deg. increments over the following range of angles 10-18.

   b. Case 2: Detailed leading-edge measurements during the up- and down-stroke a dynamically actuated NACA 0012 [$\alpha = 10 \pm 10 \sin(2\pi f t)$, k = 0.1]

at M = 0.28 (Re = 2.8 million). Data were acquired in 2.0 deg. increments over the following range of angles 10-18.

c. Case 3: Supplementary leading-edge measurements during the up- and down-stroke a dynamically actuated NACA 0012 [$\alpha = 10 \pm 5\sin(2\pi ft)$, k = 0.18] at M = 0.2 (Re = 2.0 million). Data were acquired at the following angles of attack 9.2, 11.1, and 13.0.

d. Case 4: Supplementary leading-edge measurements during the up- and down-stroke a dynamically actuated NACA 0012 [$\alpha = 15 \pm 5\sin(2\pi ft)$, k = 0.18] at M = 0.2 (Re = 2.0 million). Data were acquired at the following angles of attack 13.7, and 16.9.

e. Case 5: Static measurements were acquired at M = 0.2. These data were acquired for comparison purposes.

All of the processed data were stored in Tecplot format for each test condition, and are available from the PI. A catalog of the results is given in Chapter 6. These data are now being interrogated by the PI and his students. The results from these analyses will be reported to the ARO through subsequent technical reports; specifically, the PhD dissertation of Dipankar Sahoo and reprints of journal articles.

REFERENCES

1. McCroskey, W., "Unsteady Airfoils", *Ann. Rev. Fluid Mech.*, Vol. 14, pp. 285-311, 1982.

2. Lawrence, W. Carr, "Progress in Analysis and Prediction of Dynamic Stall", *Journal of Aircraft*, Vol. 25, No 1, pp. 6-17, January 1988.

3. Carr, L., and McCroskey, W., "A Review of Recent advances in Computation and Experimental analysis of Dynamic Stall", *International Union of Theoretical and Applied Mechanics on Fluid Dynamics at High Angle of Attack*, Tokyo, Japan, Sept. 1992.

4. Ekaterinaris, J., and Platzer, M., "Computational Prediction of Airfoil Dynamic Stall", *Progress in Aerospace Sciences*, Vol. 33, pp. 759-846, 1997.

5. Greenblatt, D., and Wygnanski, I, "Dynamic Stall Control by Periodic Excitation, Part 1: NACA 0015 Parametric Study", *Journal of Aircraft*, Vol. 38, No. 3, pp. 430-438, May 2001.

6. Leishman, J., *Principles of Helicopter Aerodynamics*, Cambridge Aerospace Series, Cambridge University Press, New York, 2000.

7. Choudhuri, P., Knight, D., and Visbal, M., "Two-Dimensional Unsteady Leading edge Separation on a Pitching Airfoil", *AIAA Journal*, Vol. 32, pp. 673-681, April 1994.

8. Boussinesq, J., "Theorie de l'ecoulement tourbillonnant et tumultueux", *Mem. Presents par Diveers Savant Acad. Sci Fr.*, Vol. 23, pp. 46-50, 1897.

9. Barakos, G., Drikakis, D., and Leschziner, M., "Numerical Investigation of the Dynamic Stall Phenomenon Using Non-Linear Eddy-Viscosity Models", *AIAA-98-2740*, Applied Aerodynamics Conference, 16th, Albuquerque, NM, June 1998.

10. Ko, Sungho, and McCroskey, W. J., "Computations of Unsteady Separating Flows over an Oscillating Airfoil", *AIAA Journal*, Vol. 35, No. 7: Technical Notes, pp. 1235-1238, July 1997.

11. Wilcox, D., *Turbulence Modeling for CFD*, 2nd. Ed., DCW Industries, Inc., La Canada, CA, 2000.

12. Carr, L. W., Chandrasekhara, M. S., Broke, N. J., "A Quantitative Study of Unsteady Compressible Flow on an Oscillating Airfoil", *Journal of Aircraft*, Vol. 31, No. 4, pp. 892-898, July-August 1994.

13. Shih, C., Lourenco, L., Van Dommelen, L., and Krothapalli, A., "Unsteady Flow Past an Airfoil Pitching at a Constant Rate", *AIAA Journal*, Vol. 30, No. 5, pp. 1153-1161, May 1992.

14. Harper, W. Paul and Roy, E. Flanigan, "Investigation of the Variation of Maximum Lift for a Pitching Airplane Model and Comparison with Flight Results", *National Advisory Committee for Aeronautics*, Technical Note No. 1734, pp. 2-18, Washington 1948.

15. Carta, F.O., "Experimental Investigation of the Unsteady Aerodynamic Characteristics of a NACA 0012 Airfoil", *Res. Rep. M-1283-1*, United Aircraft Corp., July 1960.

16. Harris, F. D. and Pryun, R. R., "Blade Stal-Half Fact, Half Fiction", *Journal of the American Helicopter Society*, Vol. 13, No. 2, pp. 27-48, April 1968.

17. Ham, N. D. and Garelick, M. S., "Dynamic Stall considerations in Helicopter Rotors", *Journal of the American Helicopter Society*, Vol. 13, No. 2, pp. 49-55, April 1968.

18. Ham, N. D., "Aerodynamic Loading on a Two-Dimensional Airfoil during Dynamic Stall", *AIAA Journal*, Vol. 6, pp. 1927-1934, October 1968.

19. Liiva, J. and Davenport, F. J., "Dynamic Stall of Airfoil Sections for High-Speed Rotors", *Journal of the American Helicopter Society*, Vol. 14, No. 2, pp. 26-33, April 1969.

20. McCroskey, W. J. and Fisher, R. K., "Detailed Aerodynamic Mesaurements on a Model Rotor in the Blade Stall Regime", *Journal of the American Helicopter Society*, Vol. 17, No. 1, pp. 20-30, January 1972.

21. Martin, J. M., Empey, R. W., McCroskey, W. J., and Caradonna, F. X., "AN Experimental Analysis of Dynamic Stall on an Oscillating Airfoil", *Journal of the American Helicopter Society*", Vol. 19, No. 1, pp. 26-32, 1974.

22. McCroskey, W. J., McAlister K. W., and Carr, L. W., "Dynamic Stall Experiments on Oscillating Airfoils", *AIAA Journal*, Vol. 14, pp. 57-63, January 1976.

23. Sankar, N. L., and Tassa, Y., "Compressibility effects on Dynamic Stall of NACA 0012 Airfoil", *AIAA Journal*, Vol. 19, pp. 557-558, May 1981.

24. Lorber, P. F., and Carta, F. O., "Airfoil Dynamic Stall at Constant Pitch Rate and High Reynolds Number", *Journal of Aircraft*, Vol. 25, No. 6, pp. 548-556, January 1988.

25. Chandrasekhara, M. S., and Carr, L. W., "Flow Visualization Studies of the Mach Number Effects on Dynamic Stall of an Oscillating Airfoil", *Journal of Aircraft*, Vol. 27, No. 6, pp. 516-522, January 1990.

26. Carr, L. W., Platzer, M. F., Chandrasekhara, M. S., and Ekaterinaris, J., "Experimental and Computational Studies of Dynamic Stall", *Numerical and Physical Aspects of Aerodynamic Flows IV*, pp. 239-256, August 1990.

27. Wilder, M. C., Chandrasekhara, M. S., and Carr, L. W., "Transition Effects on Compressible Dynamic Stall of Transiently Pitching Airfoils", *AIAA Paper*, 93-2978, July 1993.

28. Knight, D., and Choudhuri, Ghosh, P., "2-D Unsteady Leading Edge Separation on a Pitching Airfoil", *AIAA Paper*, 93-2977, July 1993.

29. Niven, A. J. M., Galbraith, R. A., and David, G. F. H., "Analysis of Reattachment during Ramp Down Tests", *Vertica*, Vol. 13, No. 2, pp. 187-196, 1989.

30. Ahmed, S., and Chandrasekhara, M. S., "*Reattachment Studies of an Oscillating Airfoil Dynamic Stall Flowfield*", AIAA Journal, Vol. 32, No. 5, pp. 1006-1012, May 1994.

31. Chandrasekhara, M. S., Wilder, M. C., and Carr, L. W., "*Boundary Layer Tripping Studies of Compressible Dynamic Stall Flow*", AIAA Journal, Vol. 34, No. 1, pp. 96-103, January 1996.

32. Geissler, W., Carr, L. W., Chandrasekhara, M. S., Wilder, M. C., and Sobieczky, H., "Compressible Dynamic Stall Calculations Incorporating Transition Modeling for Variable Geometry Airfoils", *AIAA Paper*, 1997.

33. Chandrasekhara, M. S., Wilder, M. C., and Carr, L. W., "Competing Mechanisms of Compressible Dynamic Stall", *AIAA Journal*, Vol. 36, No. 3, pp. 387-393, March 1998.

34. Chandrasekhara, M. S., Wilder, M. C., and Carr, L. W., "Compressible Dynamic Stall Control Using Dynamic Shape Adaptation", *AIAA Journal*, Vol. 39, No. 10, Technical Notes, pp. 2021-2024, June 2001.

35. Greenblatt, D., Nishri, B., Darabi, A, and Wygnanski, I, "Some Factors Affecting Stall Control with Particular Emphasis on Dynamic Stall", *AIAA Paper* 99-3504, July 1999.

36. Chandrasekhara, M. S., Wilder, M. C., and Carr, L. W., "Compressible Dynamic Stall Control: Comparison of Two Approaches", *Journal of Aircraft*, Vol. 38, No. 3, pp. 448-453, 2001.

37. Greenblatt, D., Nishri, B., Darabi, A., and Wygnanski, I., "Dynamic Stall Control by Periodic Excitation, Part 2: Mechanisms", *Journal of Aircraft*, Vol. 38, No. 3, pp. 439-447, May 2001.

38. Carr, L. W., Chandrasekhara, M. S., Wilder, L. W., and Noonan, K. W., "Effect of Compressibility on Suppression of Dynamic Stall Using a Slotted Airfoil", *Journal of Aircraft*, Vol. 38, No. 2, pp. 296-309, March 2001.

39. Norton, D., and Noak, R., "A Two-Dimensional Flow Insert for the TAMU 7 x 10' LSWT", *TAMU Aerospace Engineering Report for Test 8101 for Bell Helicopter*, January 1981.

40. McCroskey, W., McAlister, K., Carr, L., and Pucci, S., "An Experimental Study of Dynamic Stall on Advanced Airfoil Sections", Vol. 2 Pressure and Force Data, *NASA TM-84245*, July 1982.

41. dPIV, 32-bit PIV Analysis Code, Software Package, Ver. 2.1, Innovative Scientific Solutions Inc., Dayton, OH, 2005.

42. Bowersox, R., "Turbulent Flow Structure Characterization of Angled Injection into a Supersonic Crossflow", *J. of Spacecraft and Rockets*, Vol. 34, No. 2, 1997.

SUPPLEMENTAL SOURCES CONSULTED

43. Carr, L., *Personal Conversation*, June 2002.

44. Benedict, L.H., and Gould, R. D., "Towards Better Unsteady Estimates For Turbulence Statistics", *Experiments in Fluids,* Vol. 22, pp. 129 – 136, 1996.

45. T. L. Doligalski, C. R. Smith, and J. D. A. Walker, "Vortex Interactions with Walls, *Annu. Rev. Fluid. Mech.*, Vol. 26, pp. 573 – 616, 1994.

46. Glezer, A., "Fluidic Virtual Aerosurfaces for Flow Control Applications", *AFOSR 2002 Contractor's Meeting in Turbulence and Rotating Flows*, Fort Worth, TX, August 2002.

47. Katz, J., and Meneveau, C., "Measurement and Modeling of Turbulence and Complex Flow Phenomena in Multi-stage Axial Turbomachines", *AFOSR 2002 Contractor's Meeting in Turbulence and Rotating Flows*, Fort Worth TX, August 2002.

48. P. B. Martin, K. W. McAlister, M. S. Chandrasekhara, and W. Geissler, "Dynamic Stall Measurements and Computations for a VR-12 Airfoil with a Variable Droop Leading Edge*", presented at the AHS Forum 59*, Phoenix, AZ, May 6-8, 2003.

49. McCRoskey, W., *Personal Conversation*, June 2002.

50. Menon, R., and Lai, W., "Key Considerations in the Selection of Seed Particles for LDV Measurements", *4th. Int. Conference on Laser Anemom.*, Cleveland OH, Aug. 1991.

51. Pope, A., *Wind Tunnel Testing, 2nd. Ed.*, John Wiley and Sons Publications, New York, 1954.

52. Abbott, H. Ira, and Doenhoff, Von, E. Albert, "*Theory of Wing Sections*", Dover Publication, Inc., New York, 1949.

53. Raffel, Markus, Willert, E. Christian, and Kompenhans, J., "*Particle Image Velocimetry*", A Practical Guide, Springer Publications, Germany, 1998.

54. White, Frank, "*Viscous Fluid Flow", 2nd. Ed.,* McGraw Hill Publications, Boston, 2001.

55. Reynolds, O., "On the Dynamical theory of Incompressible Viscous Fluids and the Determination of the Criterion", *Phil. Trans. Roy. Soc. London Ser. A*, Vol. 186, pp. 123-164, 1895.

56. Ekoto, Isaac, "Supersonic Turbulent Boundary Layers With Periodic Mechanical Non-Equilibrium", *PhD Dissertation,* Texas A&M University*,* December, 2006.

FIGURES
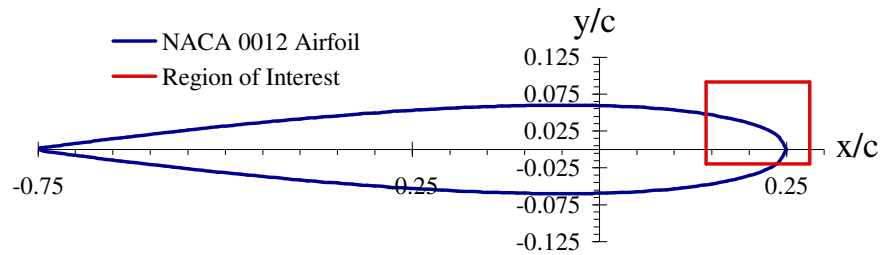
Figure 1.1 Wing Region of Interest and Coordinate System
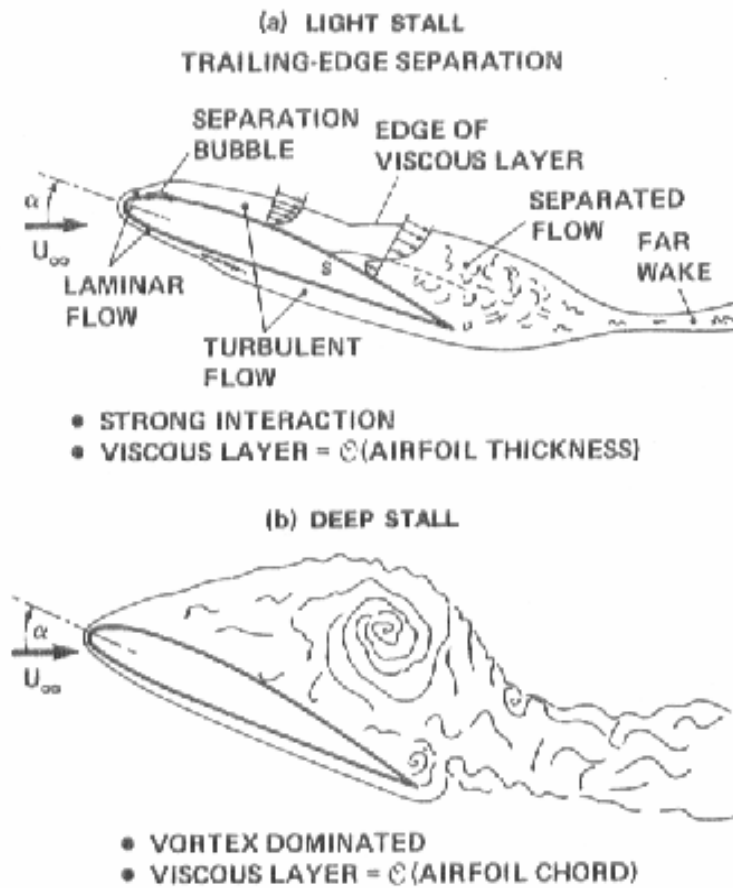
Figure 2.1 Light and Deep Dynamic Stall Flow
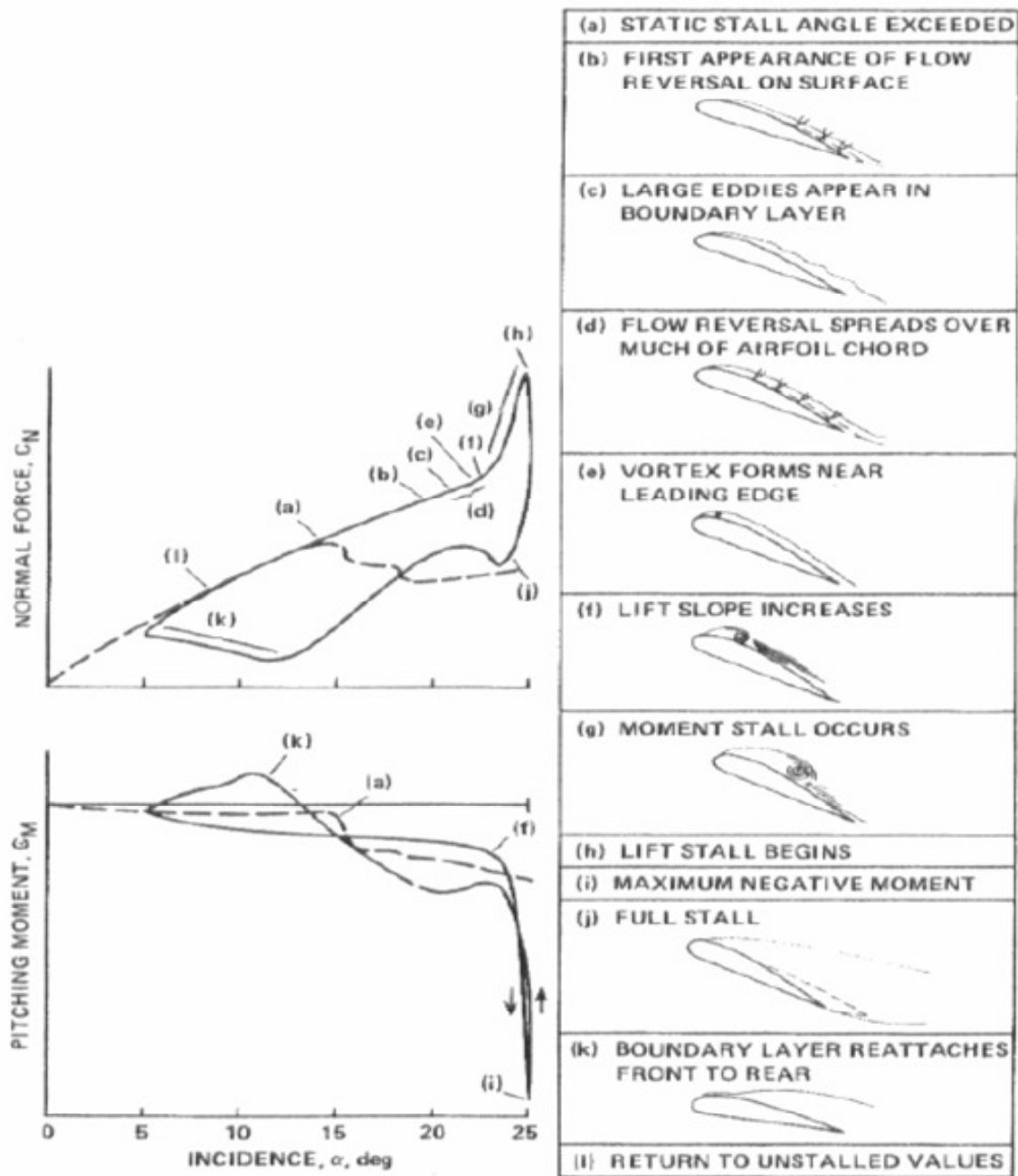
Figure 2.2 Process of Deep Dynamic Stall on a NACA Features [McCroskey[1]]
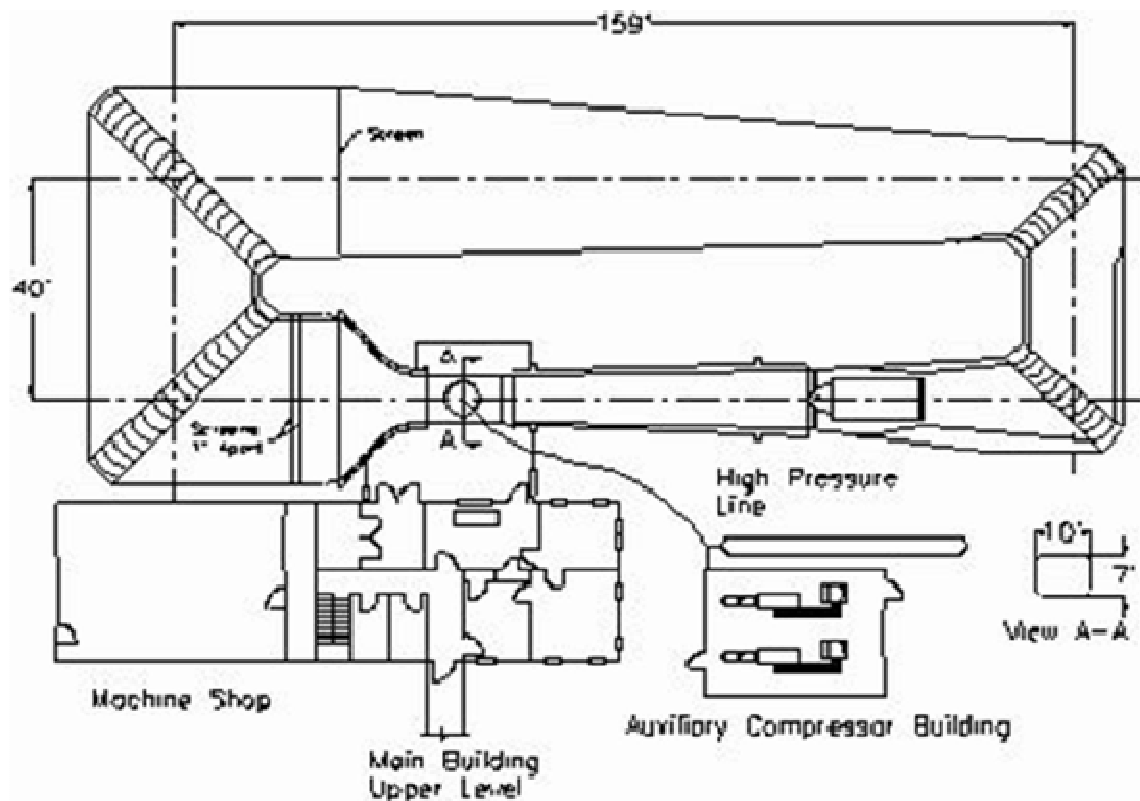
a) Schematic of the wind tunnel
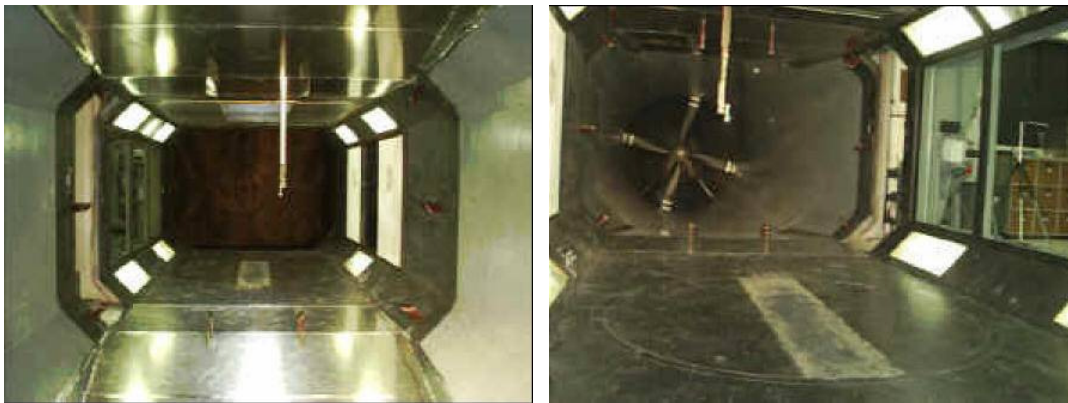
b) Upstream and downstream view of test section
Figure 4.1 Photographs of the Oran W. Nicks Wind Tunnel.

Test Section

Test Section
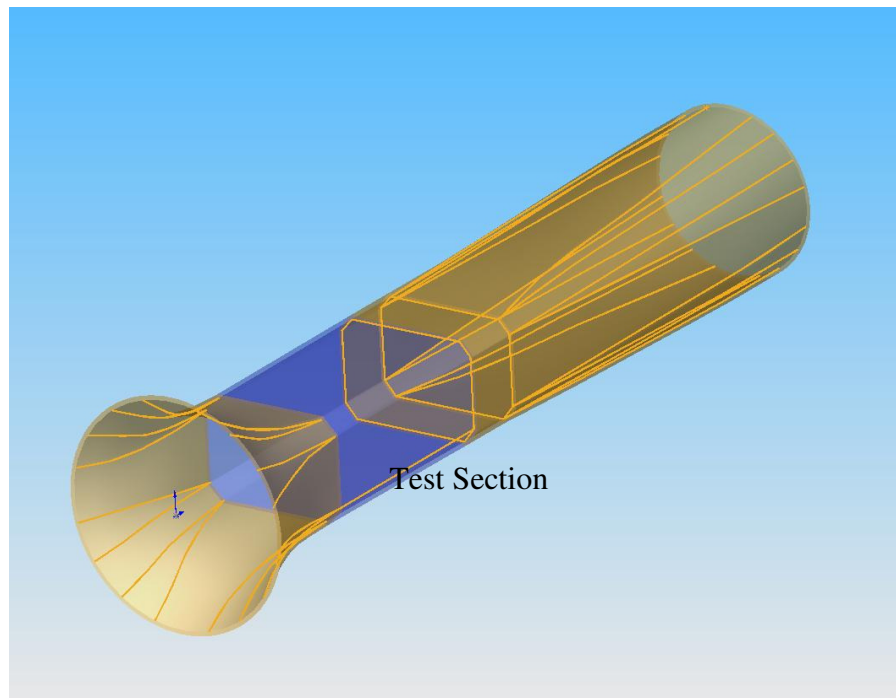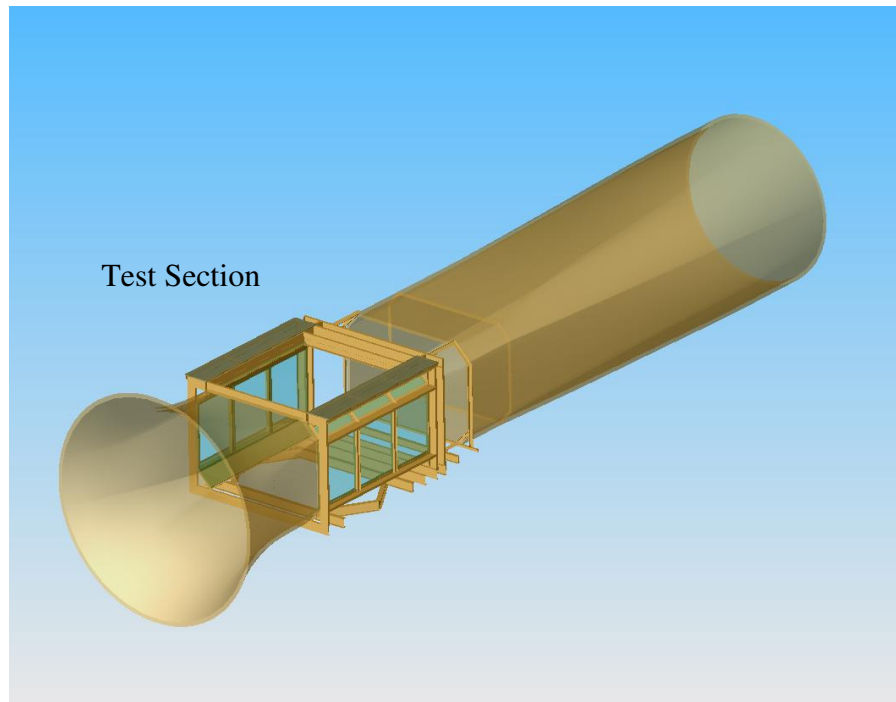
Figure 4.2 Drawings of the Oran W. Nicks Wind Tunnel

Inlet

Y-Symmetry

X-Symmetry
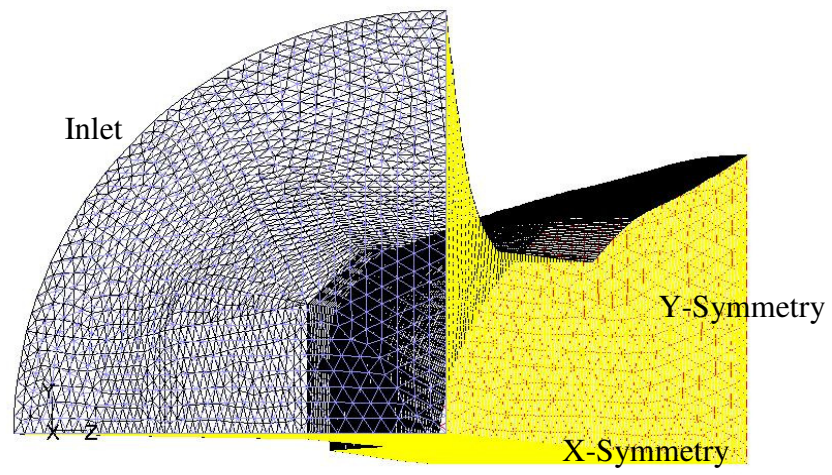
Figure 4.3 Grid of the Oran W. Nicks Wind Tunnel

(a) Floor

(b) Wall
Figure 4.4 Vinyl tubes taped to the wind tunnel

P(Wall) Vs. X-location
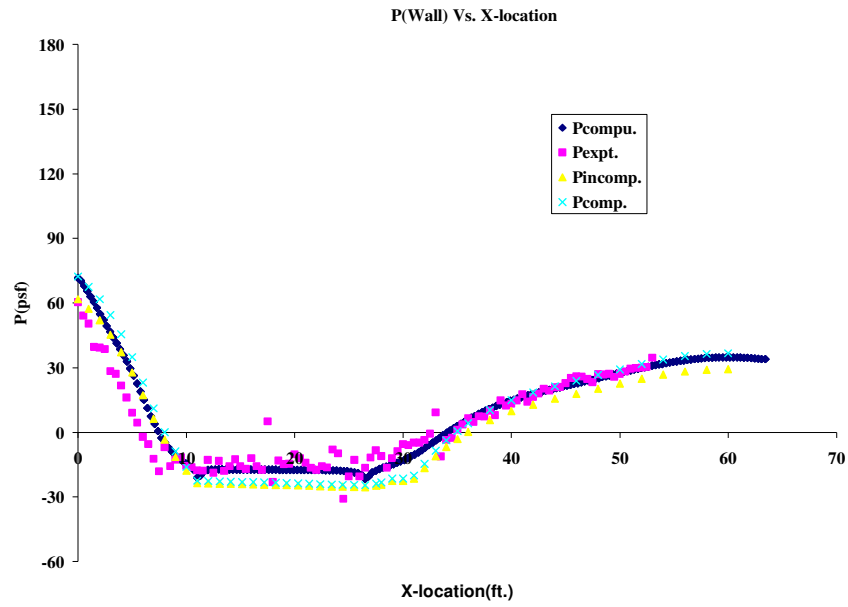
Figure 4.5 Comparison of pressure data on the wall (7 ft x 10 ft)

P(Floor) Vs. X-location
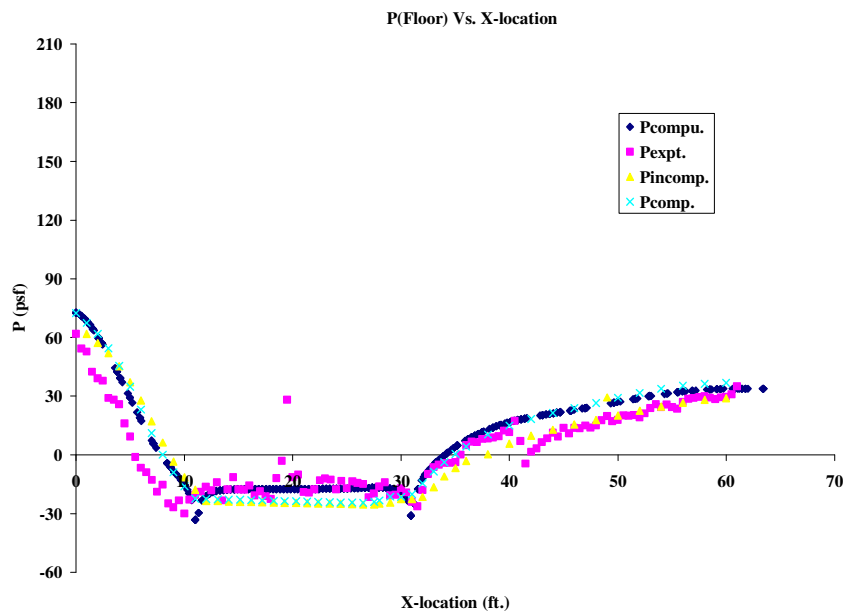
Figure 4.6 Comparison of pressure data on the floor (7 ft x 10 ft)
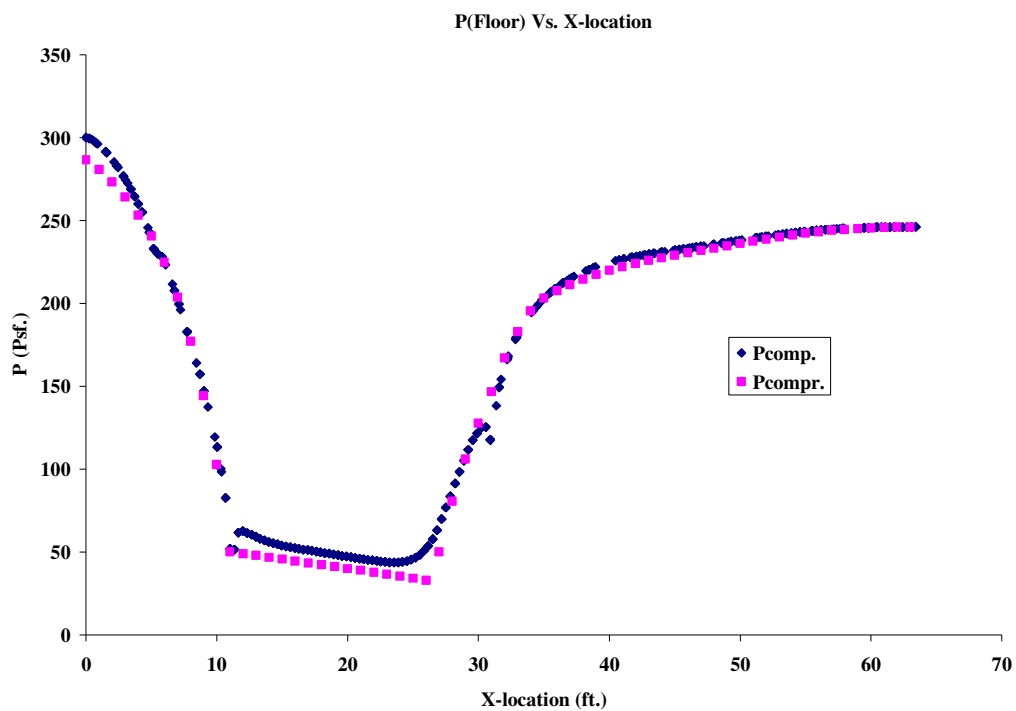
Figure 4.7 Pressure on the 7 ft x 7ft tunnel floor
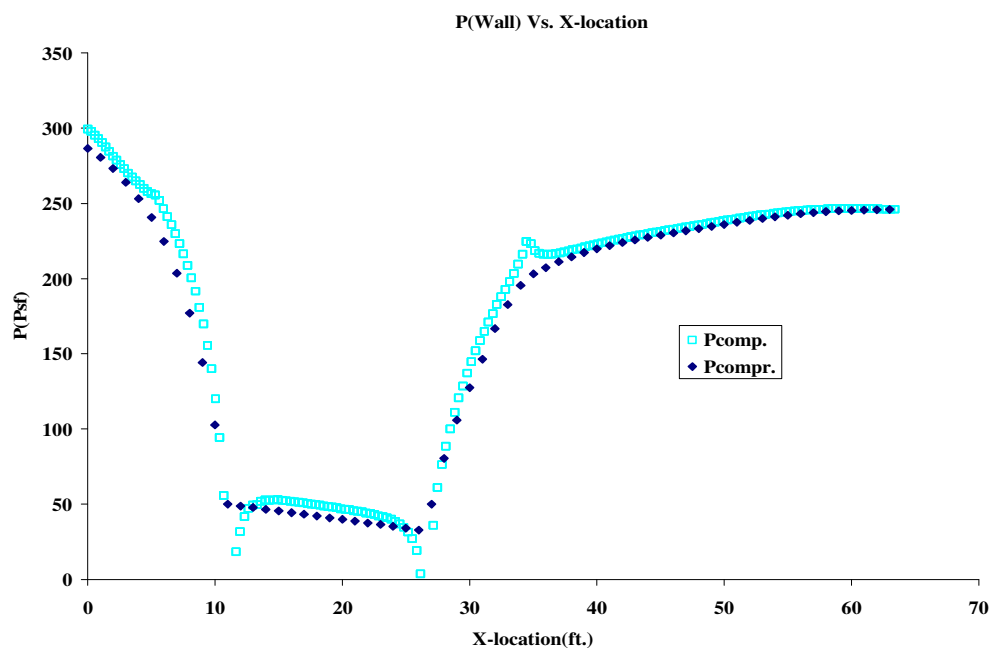
Figure 4.8 Pressure on the 7 ft x 7ft tunnel wall

81
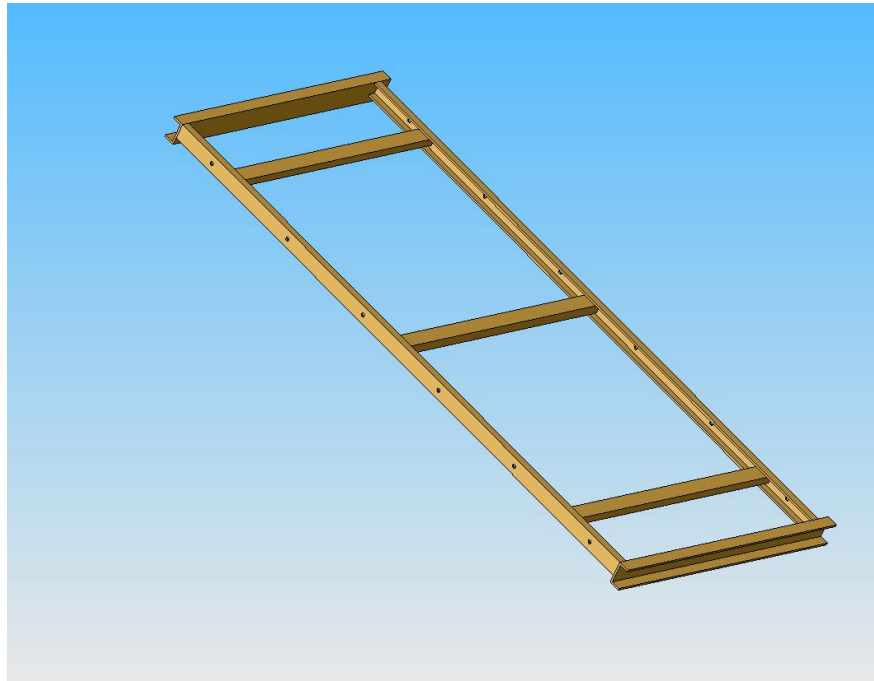
Figure 4.9 Drawing of wall panel support
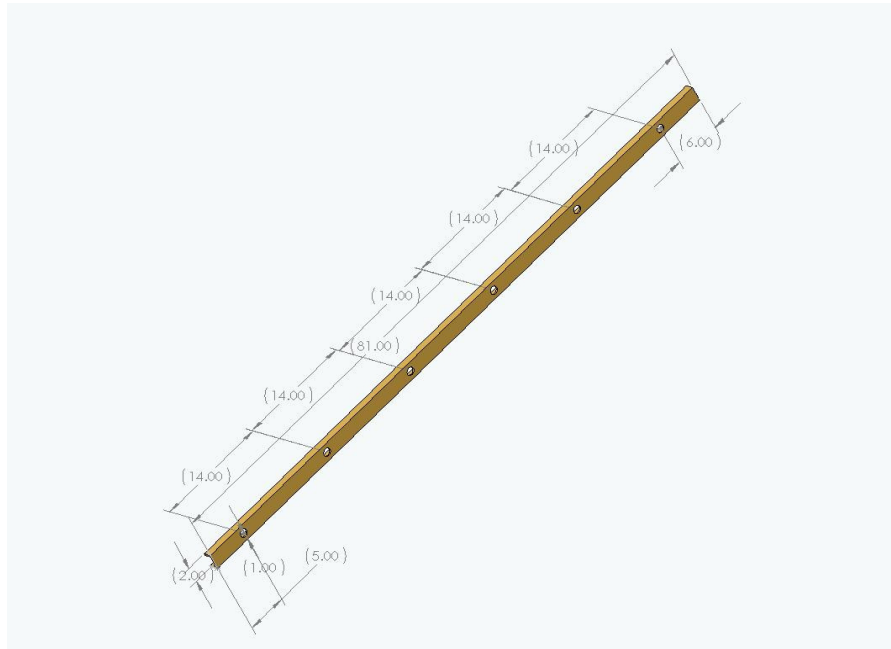
(a) 2 in. x 1 in. C-channel
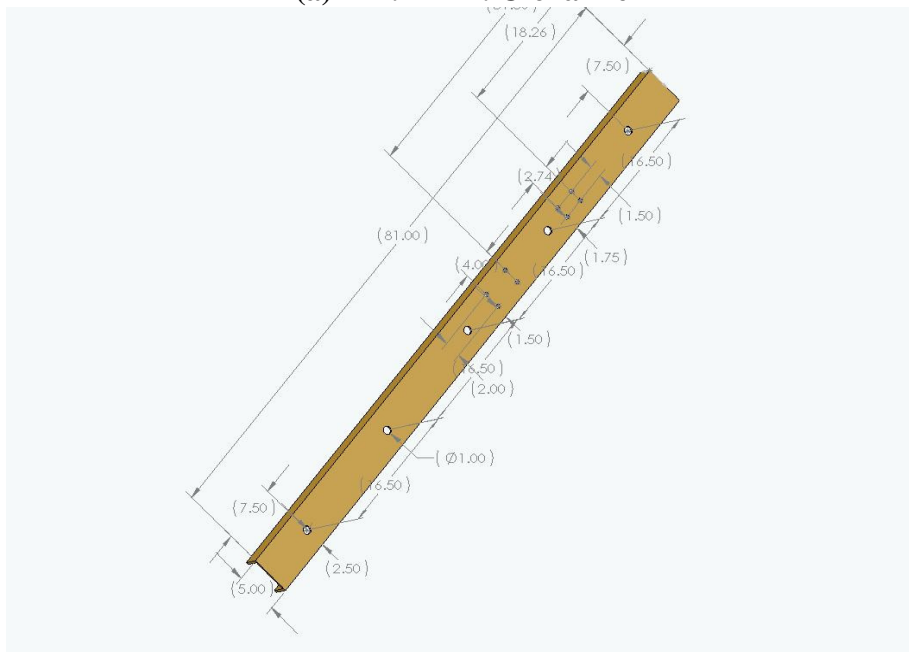
(b) 5 in. x 1.75 in. C-channel
Figure 4.10 Hole patterns in C-channels
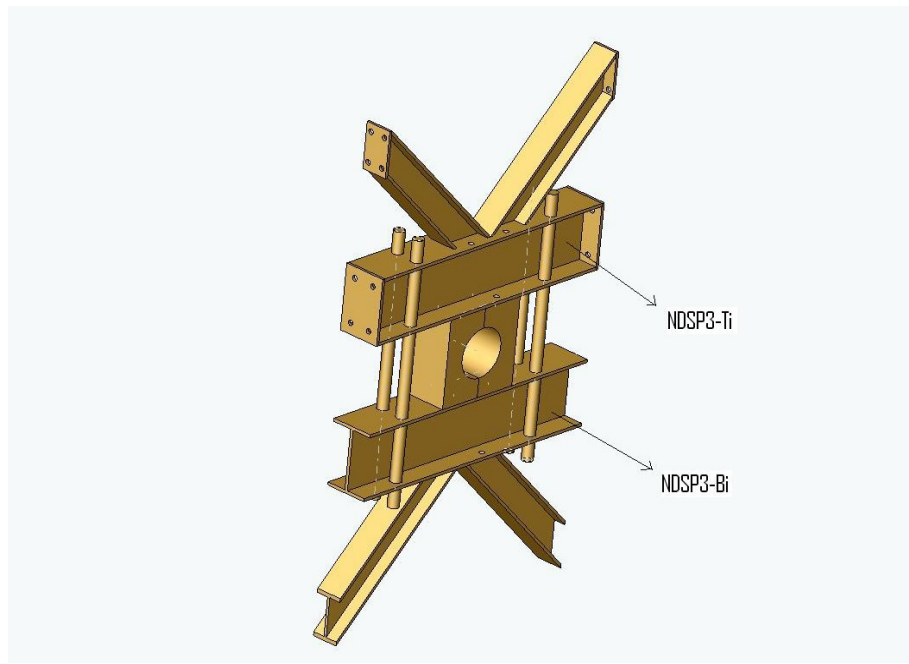
Figure 4.11 Wing Support Structure

Figure 4.12 Shaft of the wing going through the bearing housing

Figure 4.13 Additional structures from inside of the modified wind tunnel
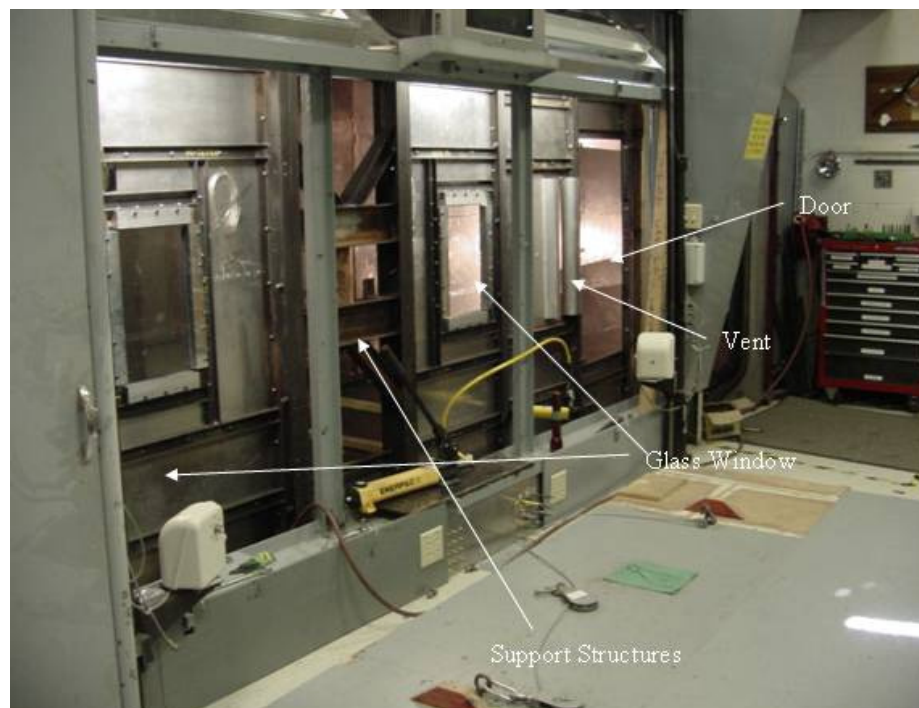
Figure 4.14 Glass windows, structures to hold wing, vent and door on left wall

Figure 4.15 Optical glass windows for 2D PIV experiment
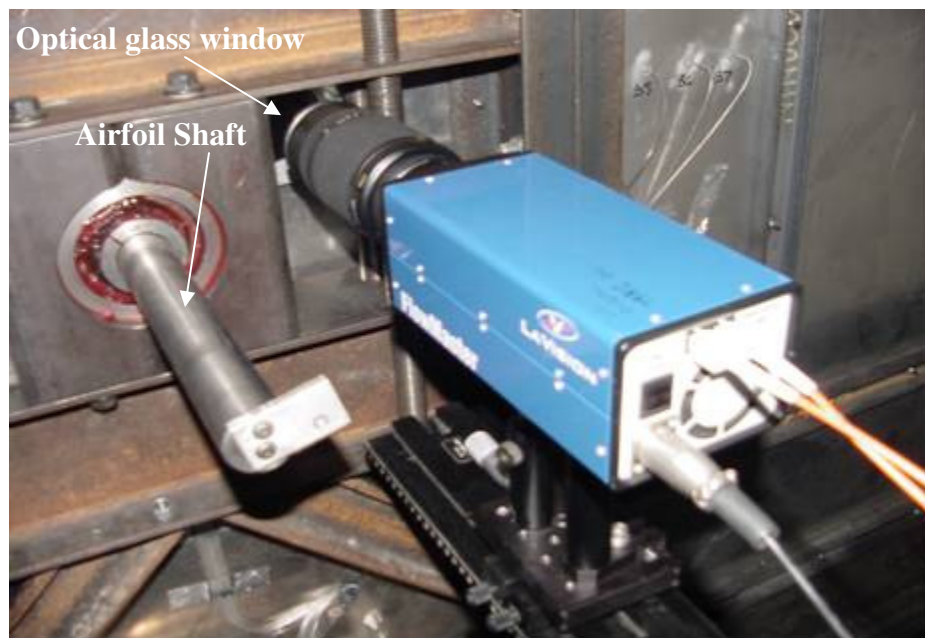
Figure 4.16 Optical glass window with the camera acquiring images
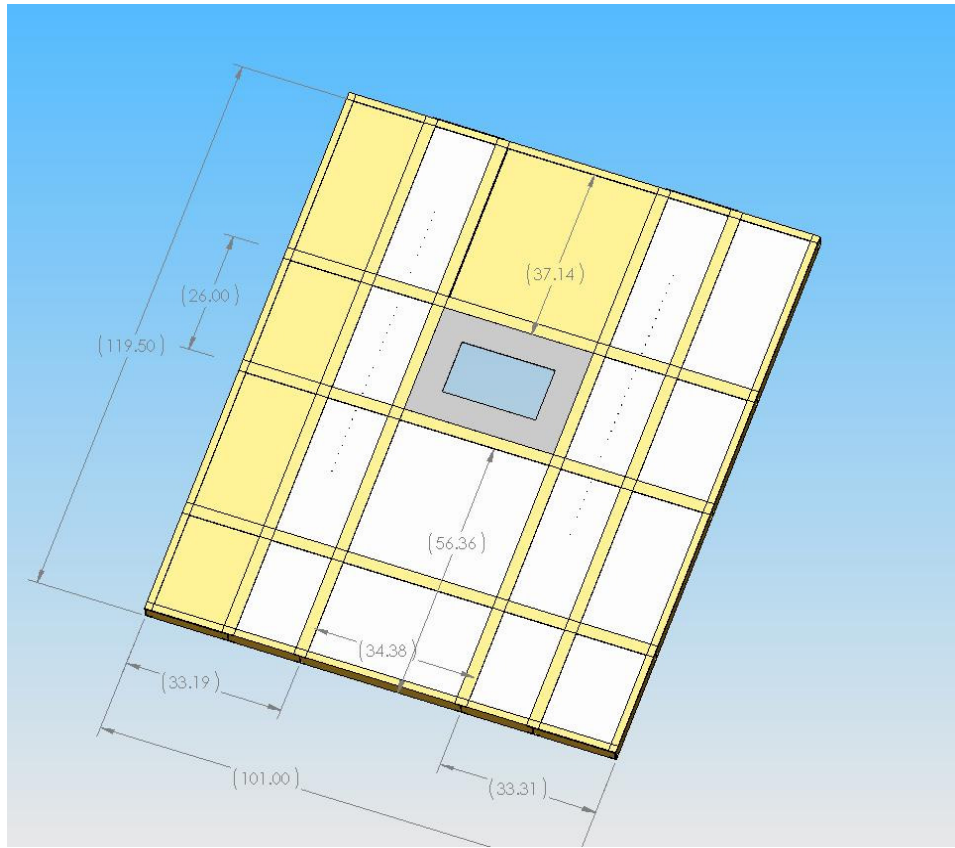
Figure 4.17 Design of the roof
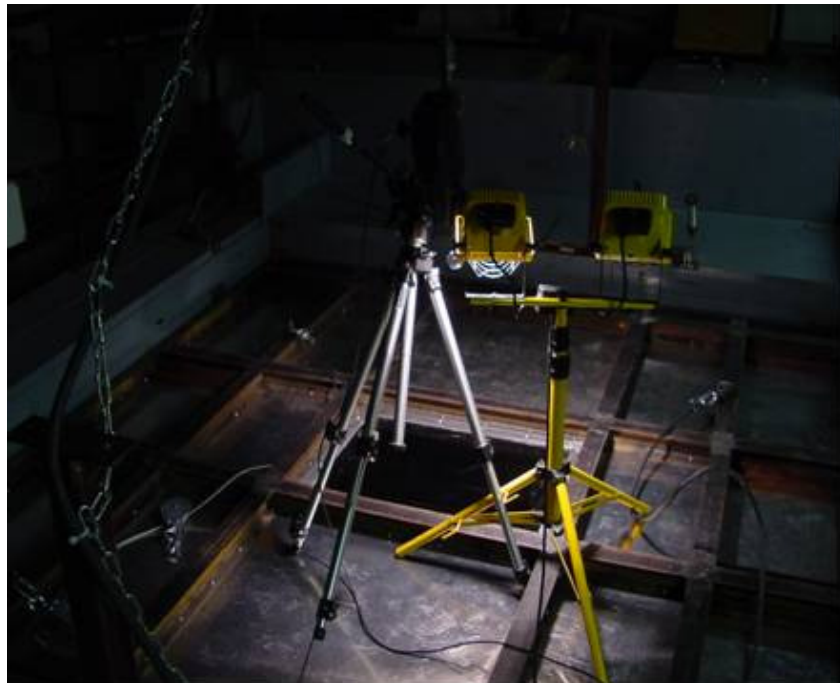
Figure 4.18 Roof with the Plexiglas window

Figure 4.19 Card board used to define the shape of inlet

Figure 4.20 Curved steel frame of the inlet

Figure 4.21 Curved aluminum sheet screwed to steel frame

Figure 4.22 Steel frame of inlet screwed to the concrete

Figure 4.23 Inlet section of the modified wind tunnel
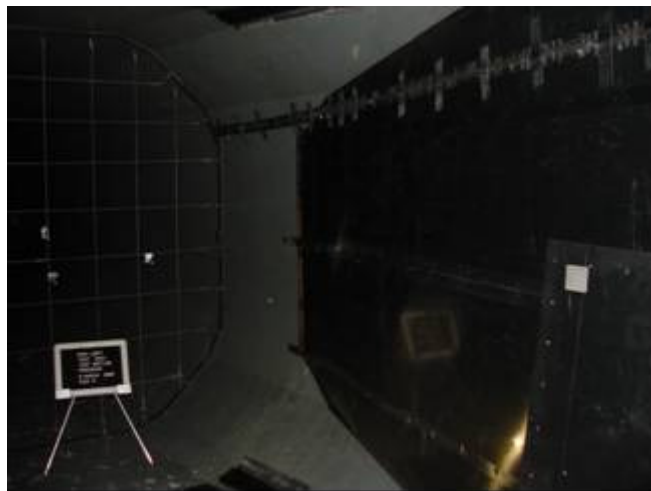
Figure 4.24 Left diffuser wall of the modified wind tunnel
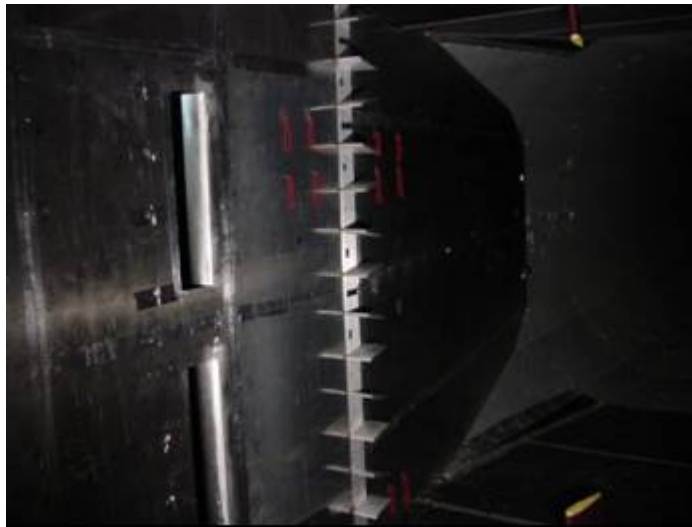
Figure 4.25 Vortex generators
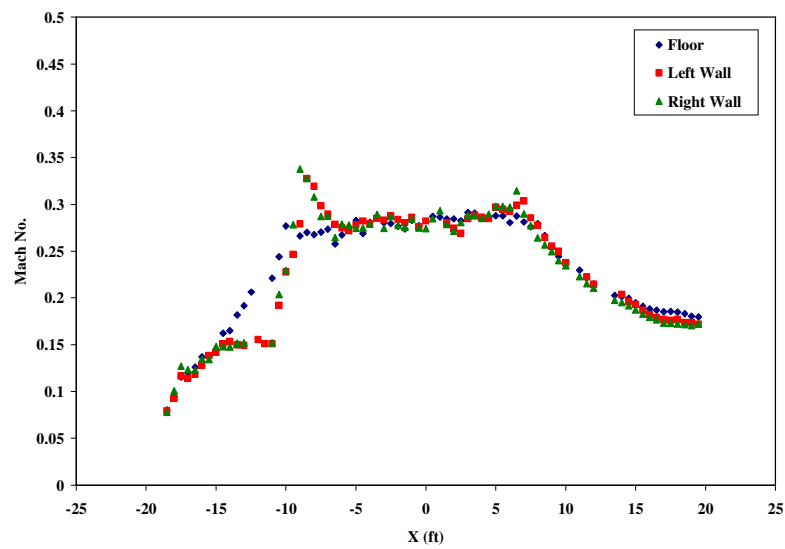
(a) Mach Number
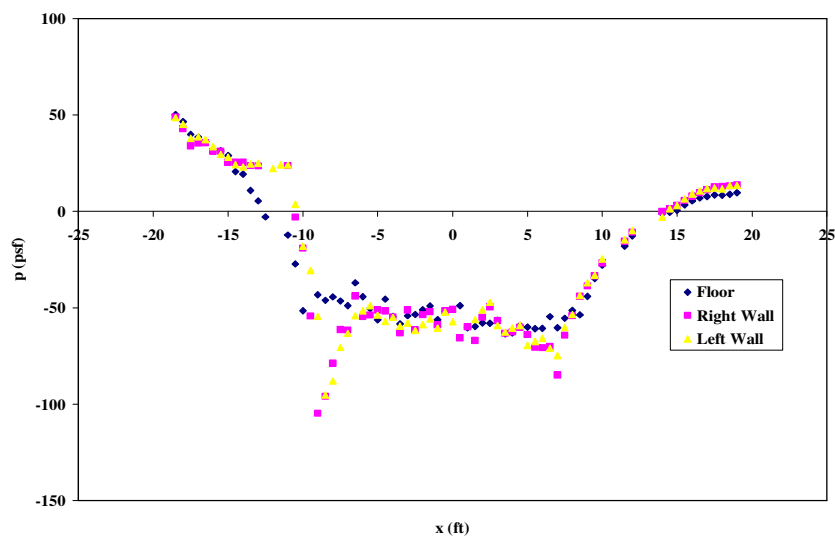
(b) Static Presure
Figure 4.26 Calibration of Modified Test Section
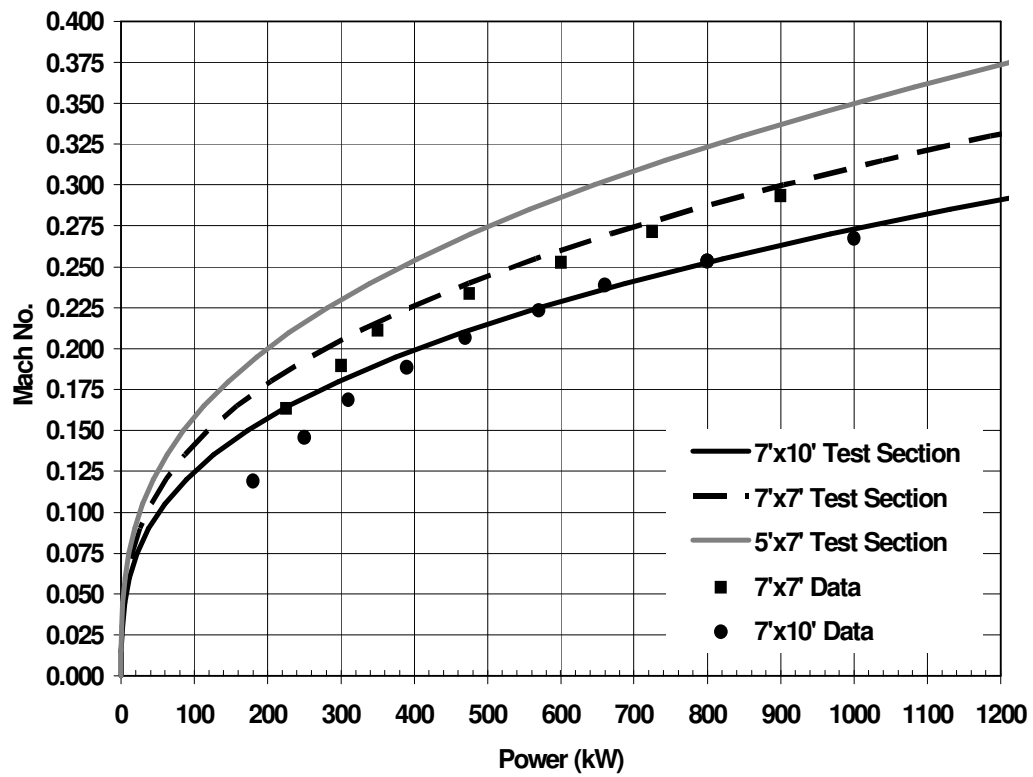
Figure 4.27 Power requirement calculations

Figure 4.28 28 3 in x 3 in C-channels bolted to the steel frame of 7 ft x 7 ft wind tunnel
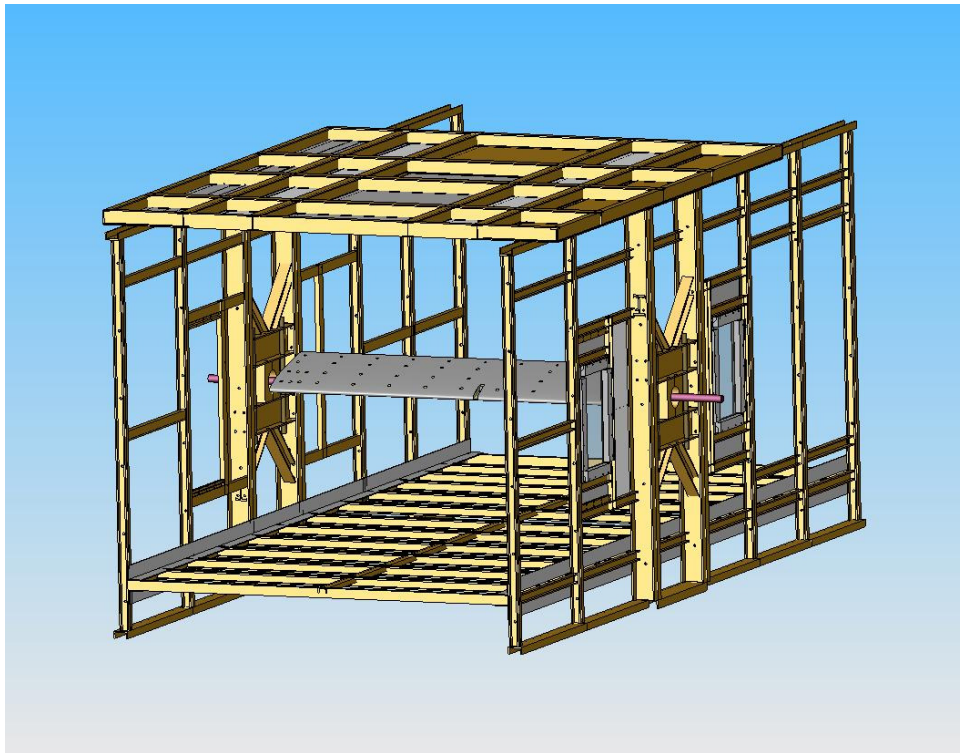
Figure 4.29 SolidWorks drawing of floor of the 5 ft x 7 ft test section
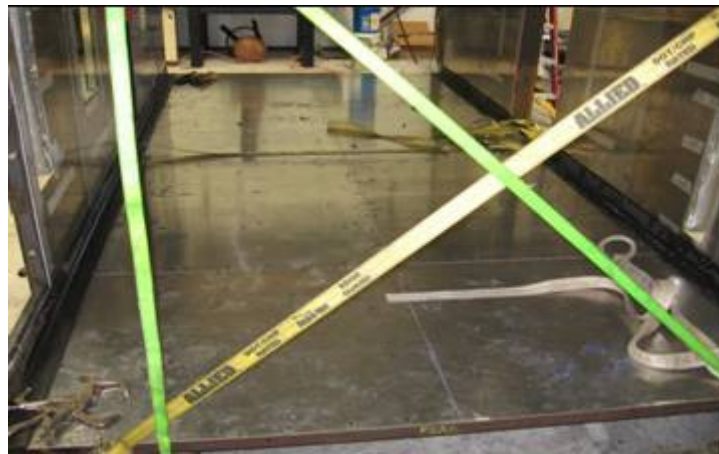
Figure 4.30 Floor of the 5 ft x 7 ft test section
(straps were used ensure the facility angles were true)

Figure 4.31 Roof of the 5 ft x 7 ft test section
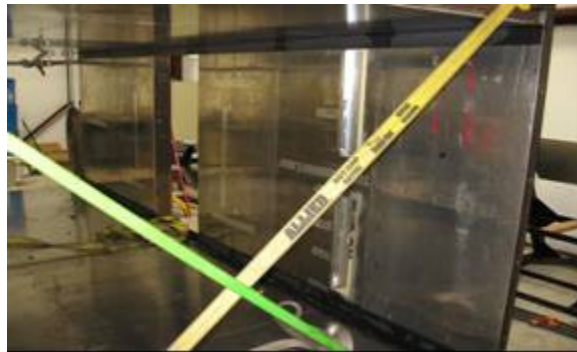
Figure 4.32 Right side view of the 5 ft x 7 ft test section

Figure 4.33 Left side view of the 5 ft x 7 ft test section

Figure 4.34 Left wall of the test section with frames

Figure 4.35 Left and right wall of the test section with frames

Figure 4.36 Right wall of the test section with aluminum sheet

Figure 4.37 Roof of the test section with glass window

Figure 4.38 View of the wind tunnel inserts from stilling chamber

Figure 4.39 View of the wind tunnel from the ready room
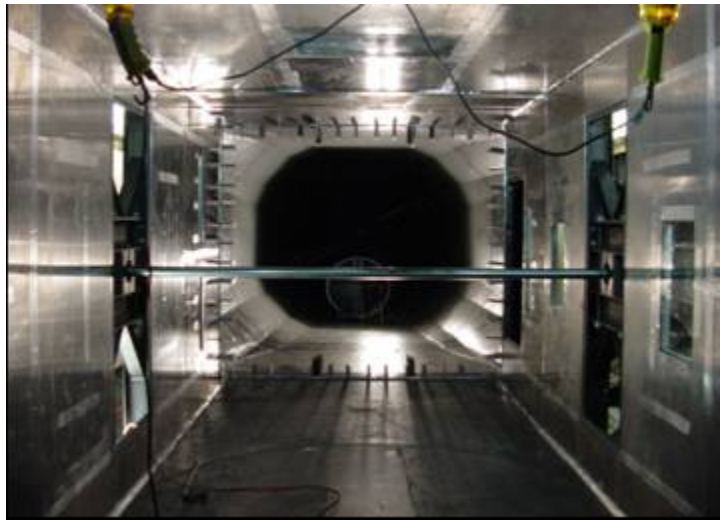
Figure 4.40 View of the 7ft x 7ft tunnel

P (Pa) Vs. c (in)
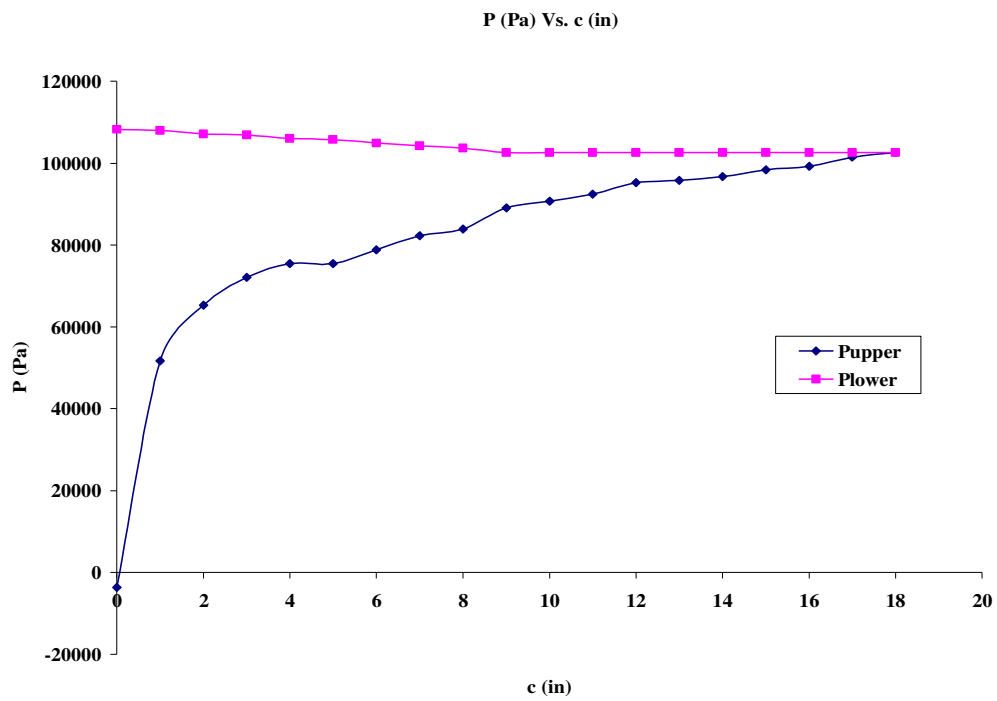
Figure 4.41 Loading condition applied to the wing in ABAQUS
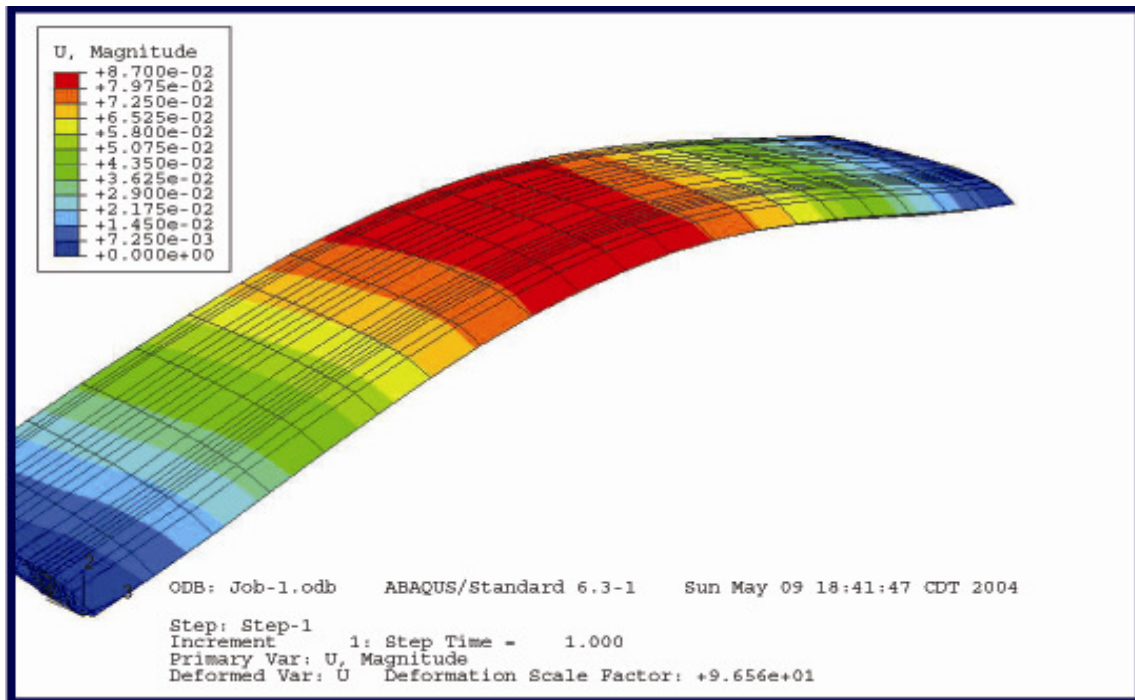
Figure 4.42 Contour plot of deflection analysis on the wing using ABAQUS
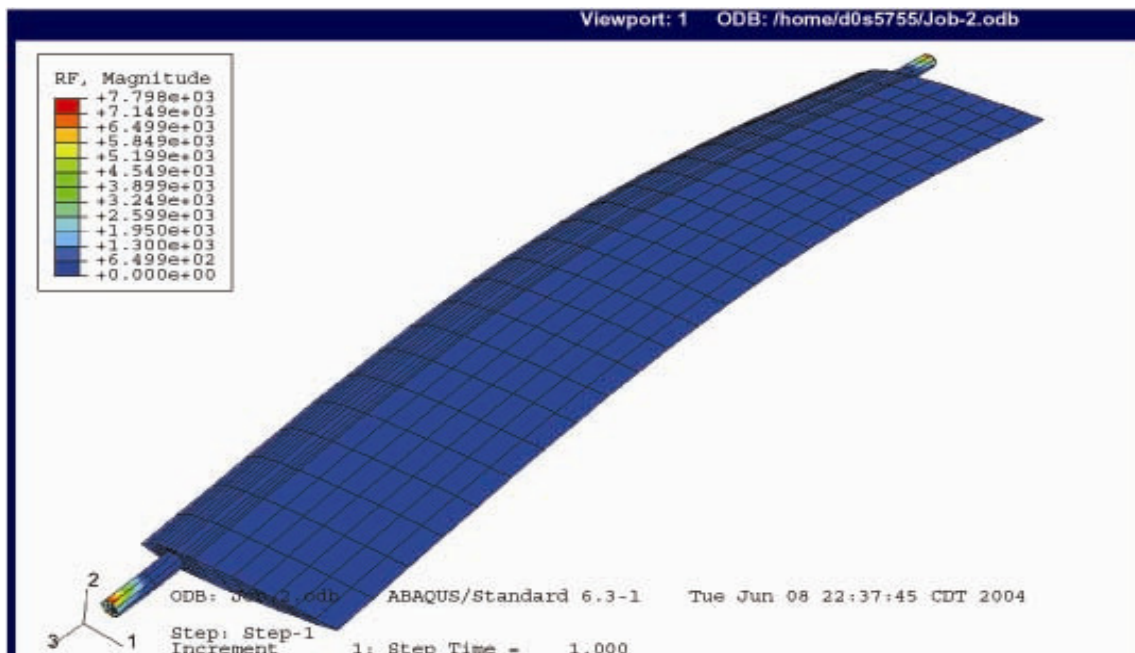
Figure 4.43 Contour plot of reaction force analysis on the wing using ABAQUS
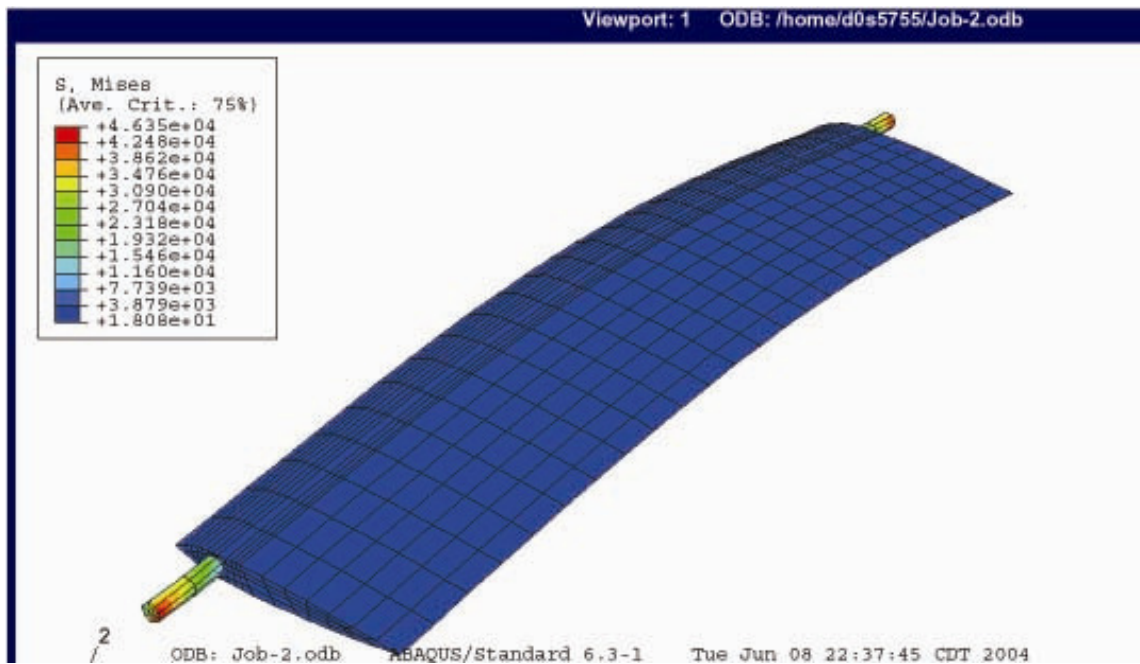
Figure 4.44 Contour plot of stress analysis on the wing using ABAQUS
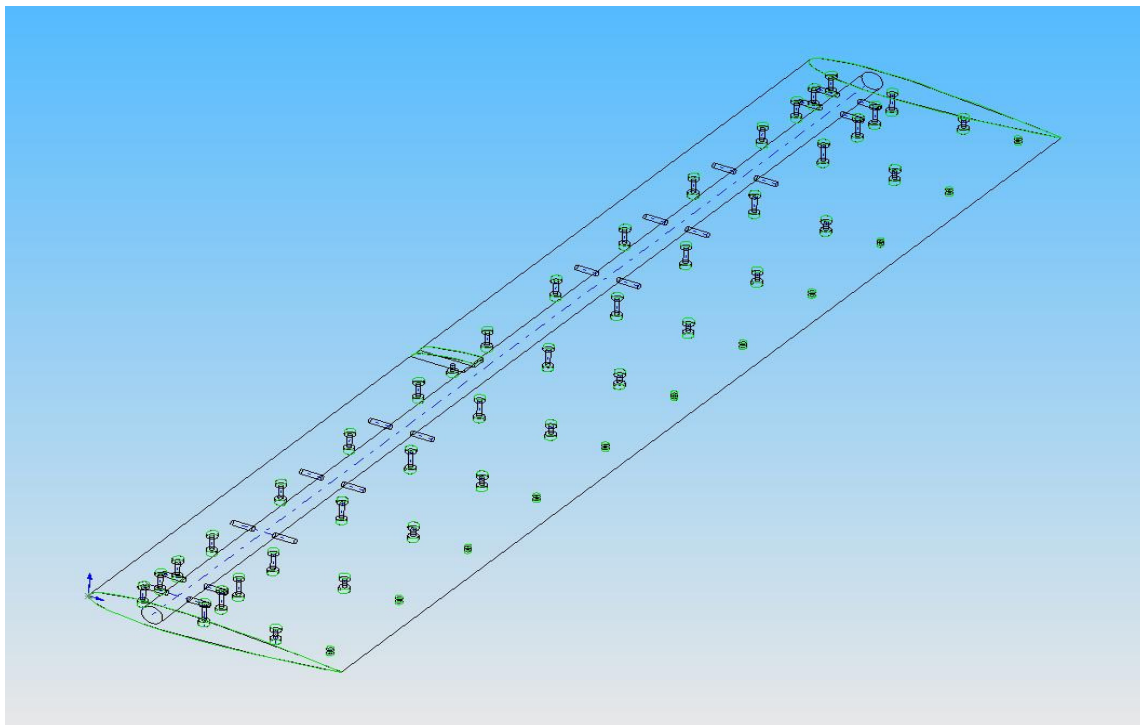
Figure 4.45 Detail drawing of the wing with screws and dowel pins
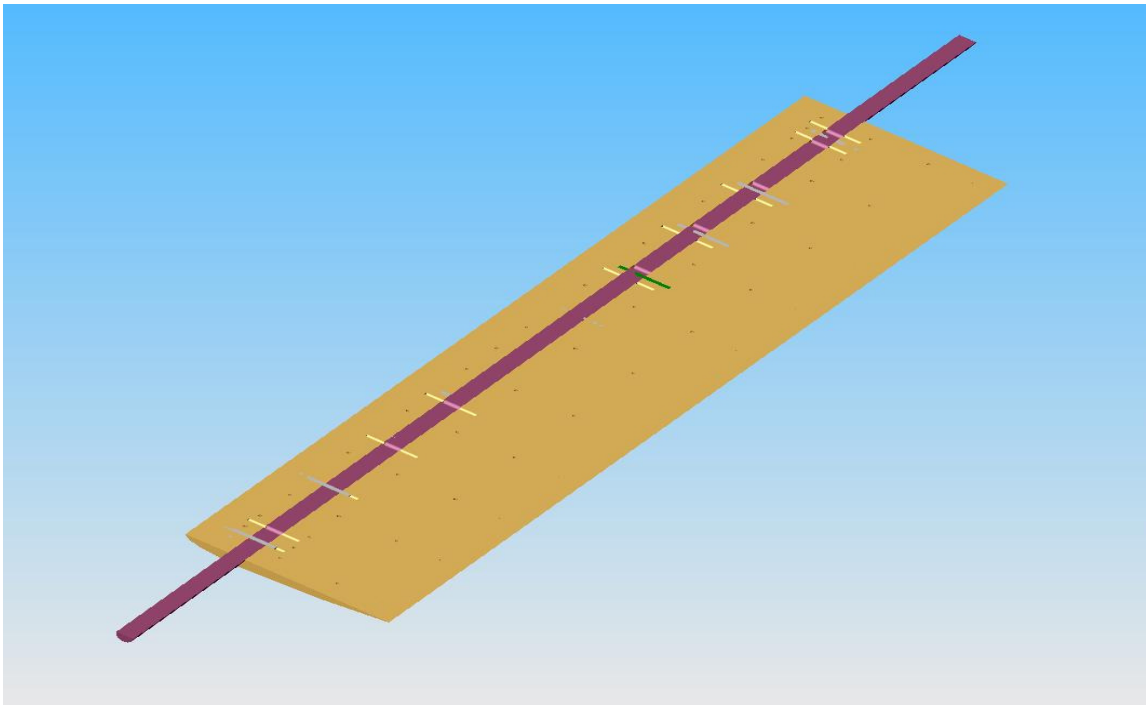
Figure 4.46 Cross sectional drawing of bottom half of the wing

Figure 4.47 NACA 0012 Model (Plexiglas insert: midspan at the leading edge)

Figure 4.48 Hydraulic drive system reservoir

Figure 4.49 Accumulator with servo valve
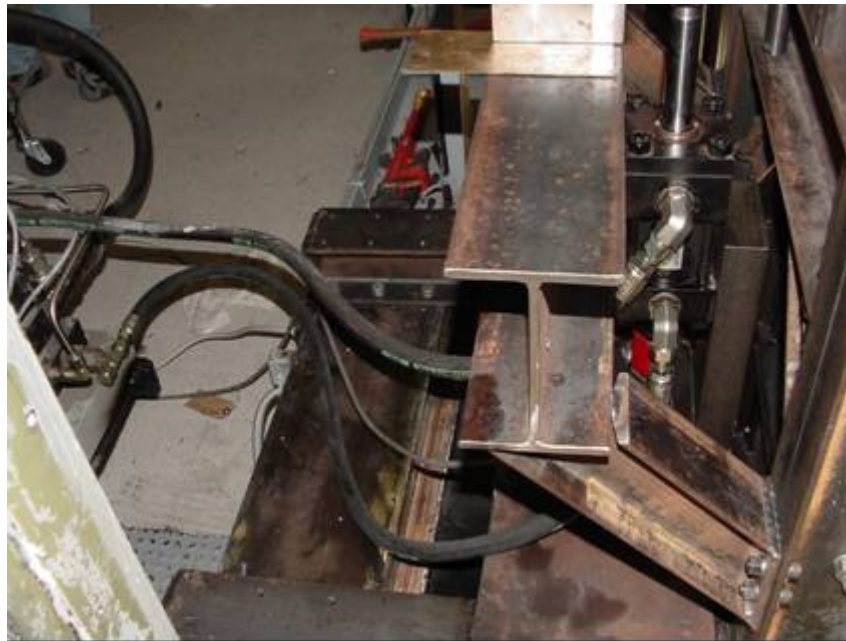
Figure 4.50 Hydraulic actuator with hoses

Figure 4.51 Actuator and the moment arm

Figure 4.52 Linear position sensor attached to the hydraulic actuator

Figure 4.53 Stand to hold the wing during synchronization testing

Figure 4.54 Stand holding the pitching wing
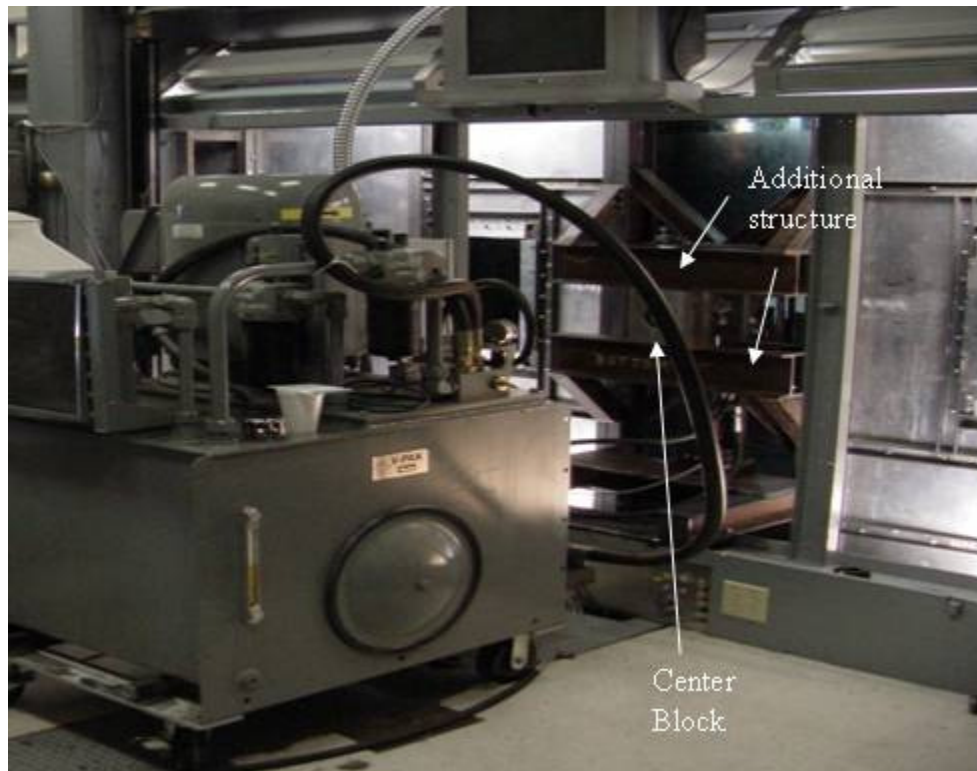
Figure 4.55 Structures to reduce vibration

Figure 4.56 Structure to support the actuator and transfer the load

Figure 4.57 Wing vibration and load support structures in-place

Figure 4.58 Image of the hydraulic actuator drive system
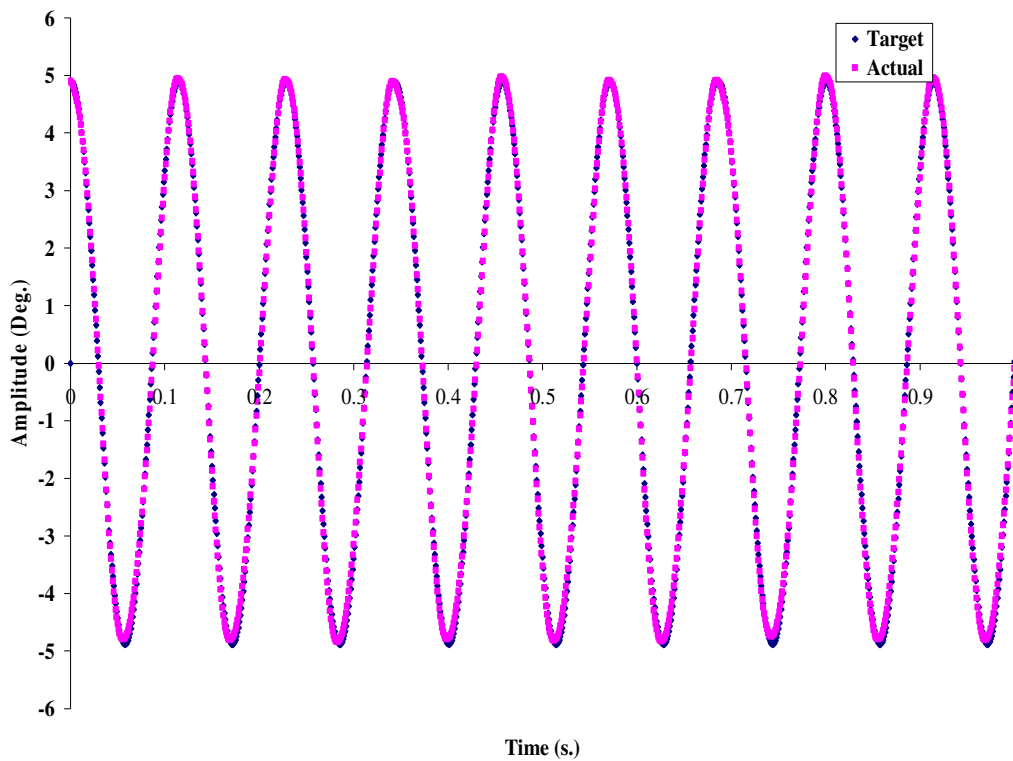
Figure 4.59 Plot of pitching of the wing following a sine function
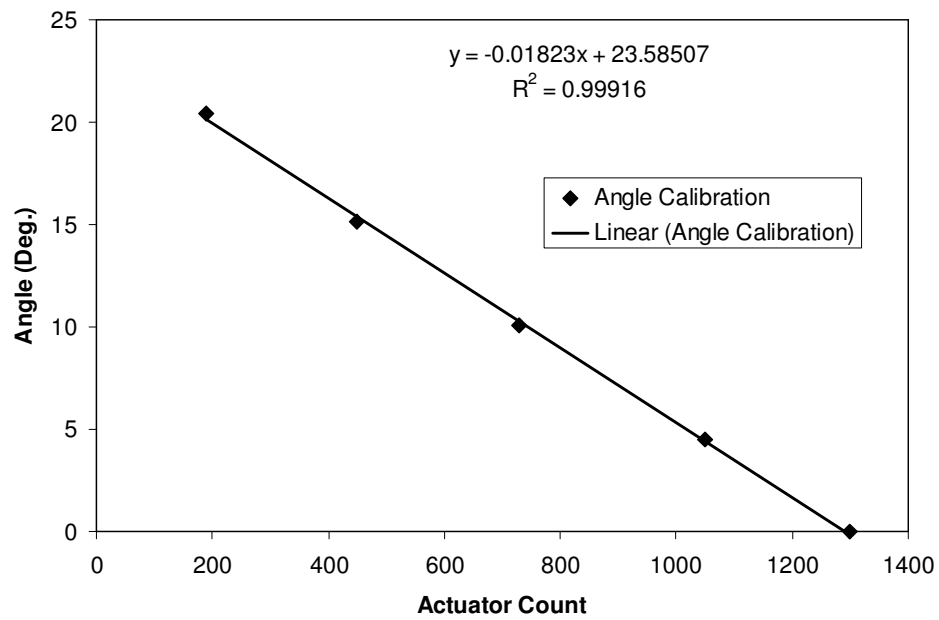
Figure 4.60 Example wing angle-of-attack calibration
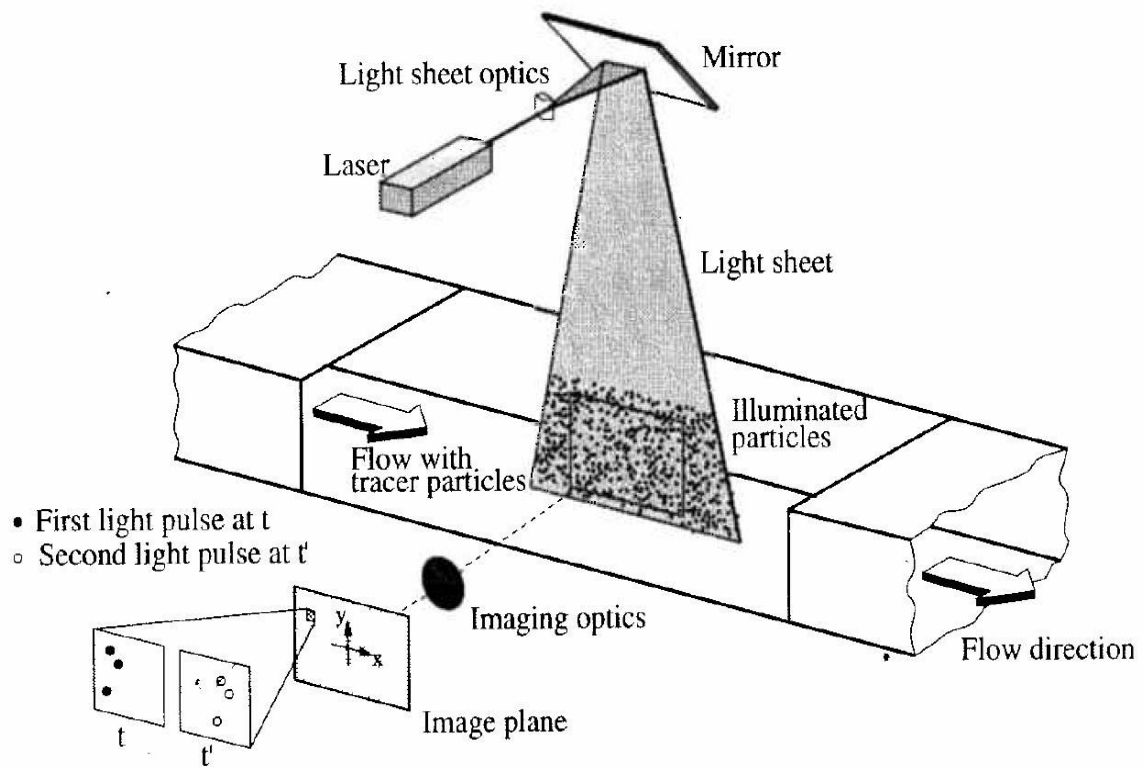
Figure 5.1 Experimental arrangement of PIV in a wind tunnel
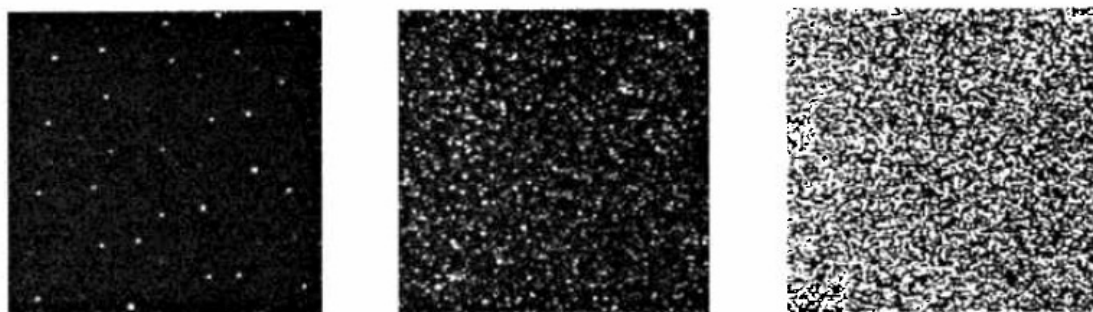
(a) low (PTV)   (b) medium (PIV)   (c) high (LSV)

Figure 5.2 The three modes of particle image density
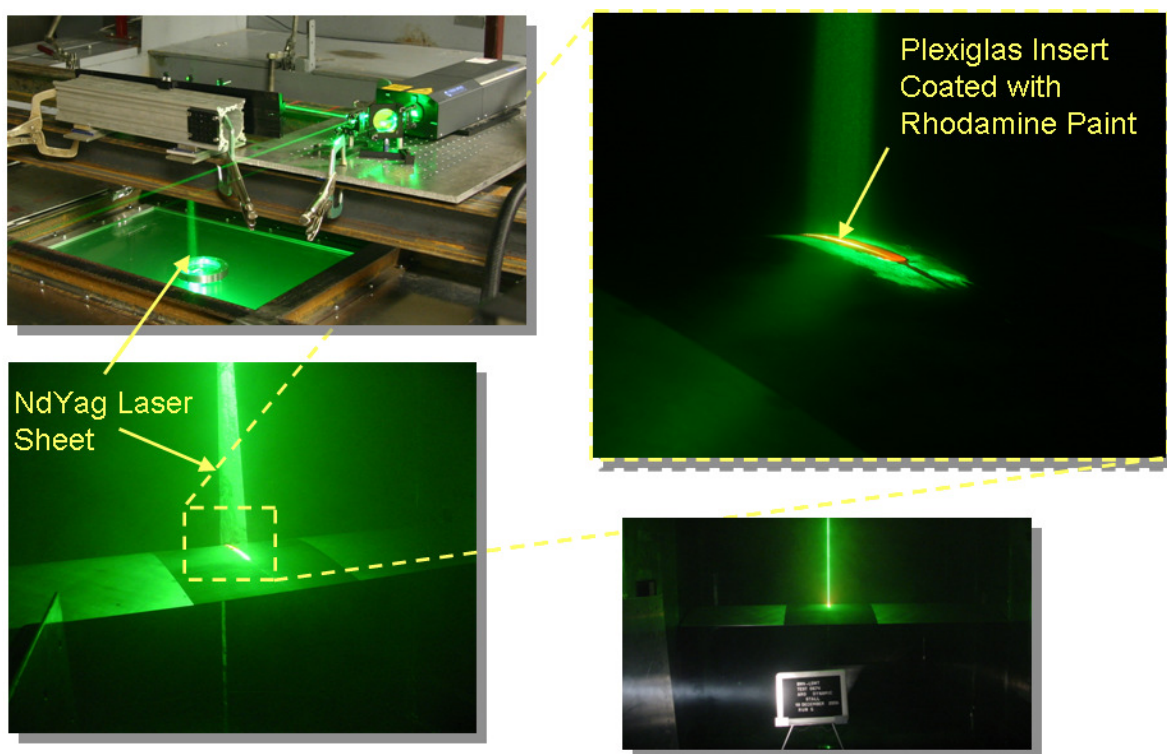
Figure 5.3 Experimental setup for the laser and the optics

Figure 5.4 H-shaped stand to support the camera

Figure 5.5 Experimental setup for the camera
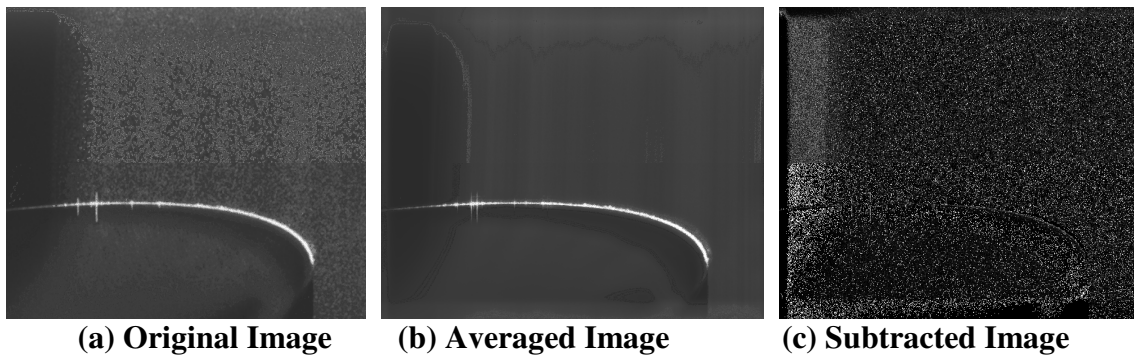
    (a) Original Image   **(b) Averaged Image**   **(c) Subtracted Image**
Figure 5.6 Image Processing Steps
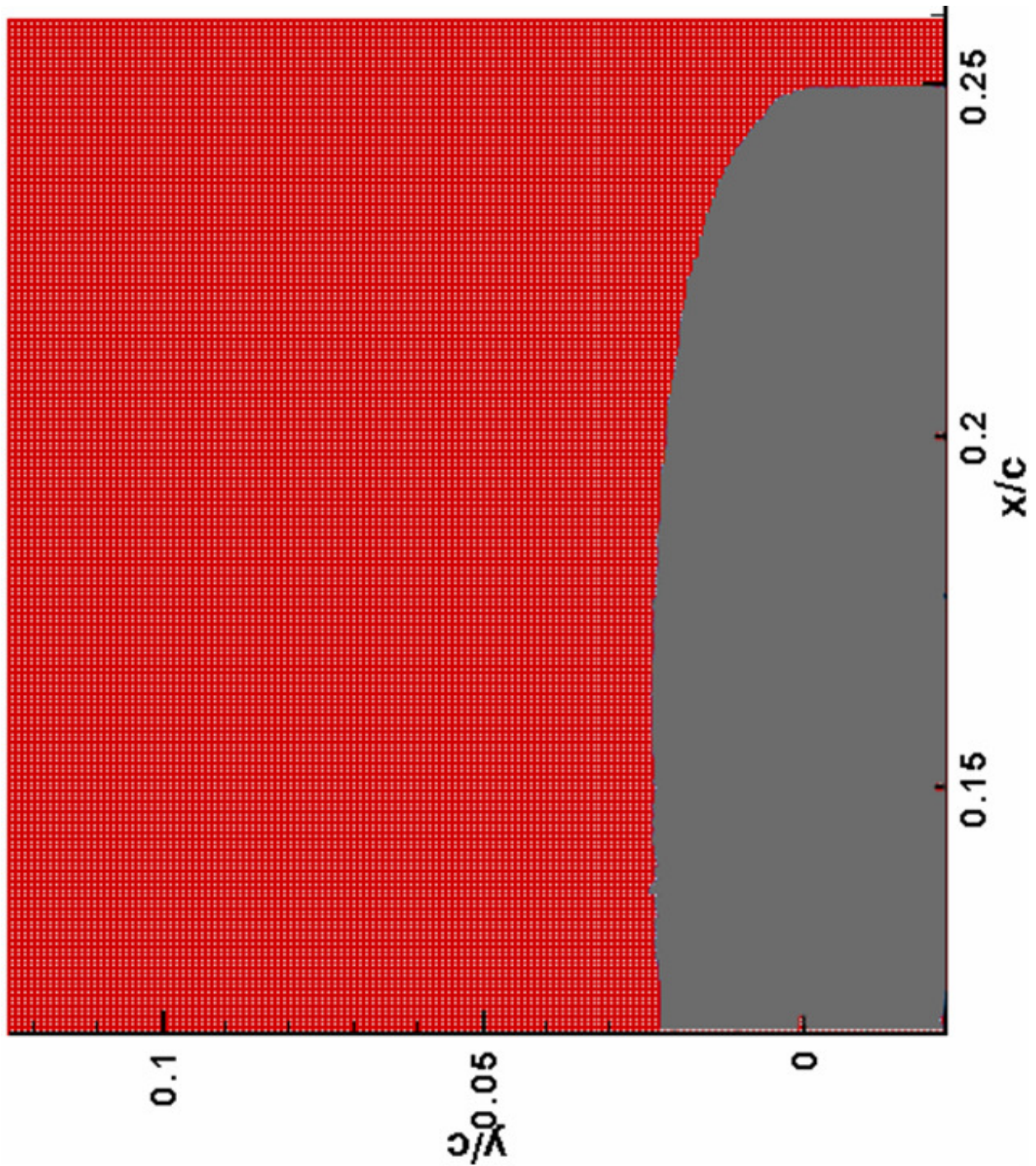
Figure 5.7 Hyper fine data reduction mesh
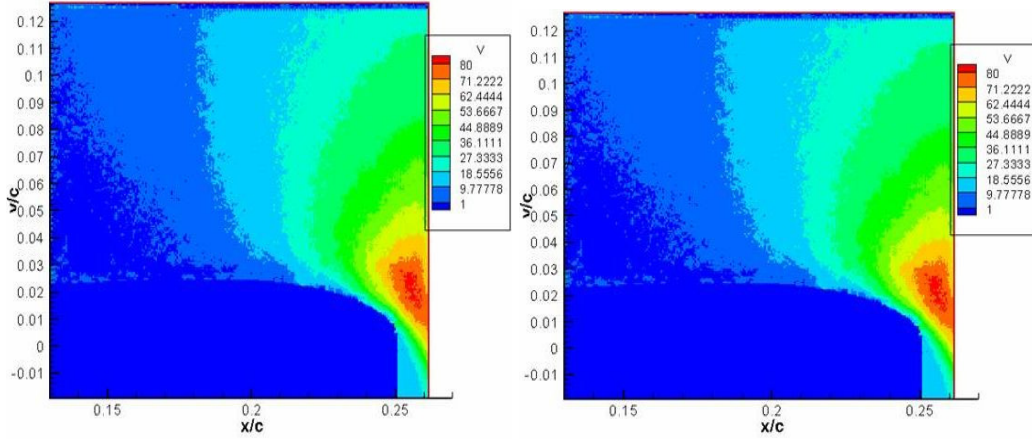
(a) Nearest neighbor option off   **(b) Nearest neighbor option on**

Figure 5.8 Nearest Neighbor Filter Effect
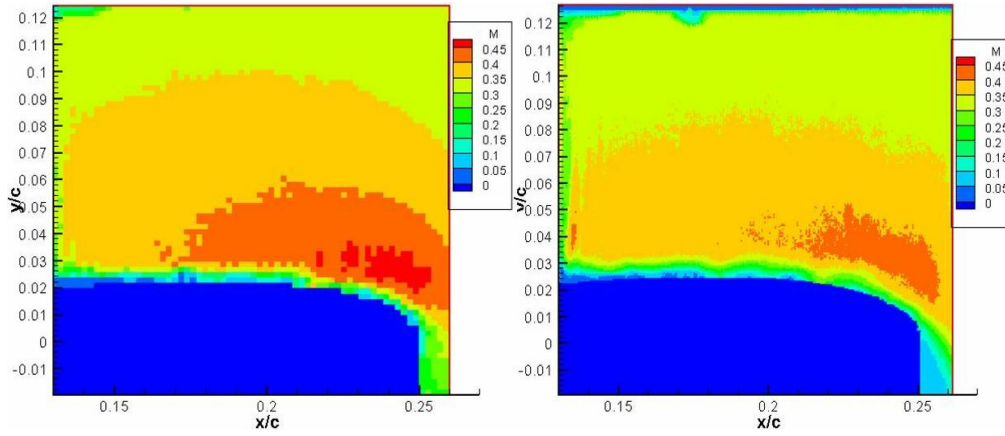
(a) Course Mesh (8 pixel)   **(b) Hyperfine (4 pixel)**

Figure 5.9 Mesh refinement study
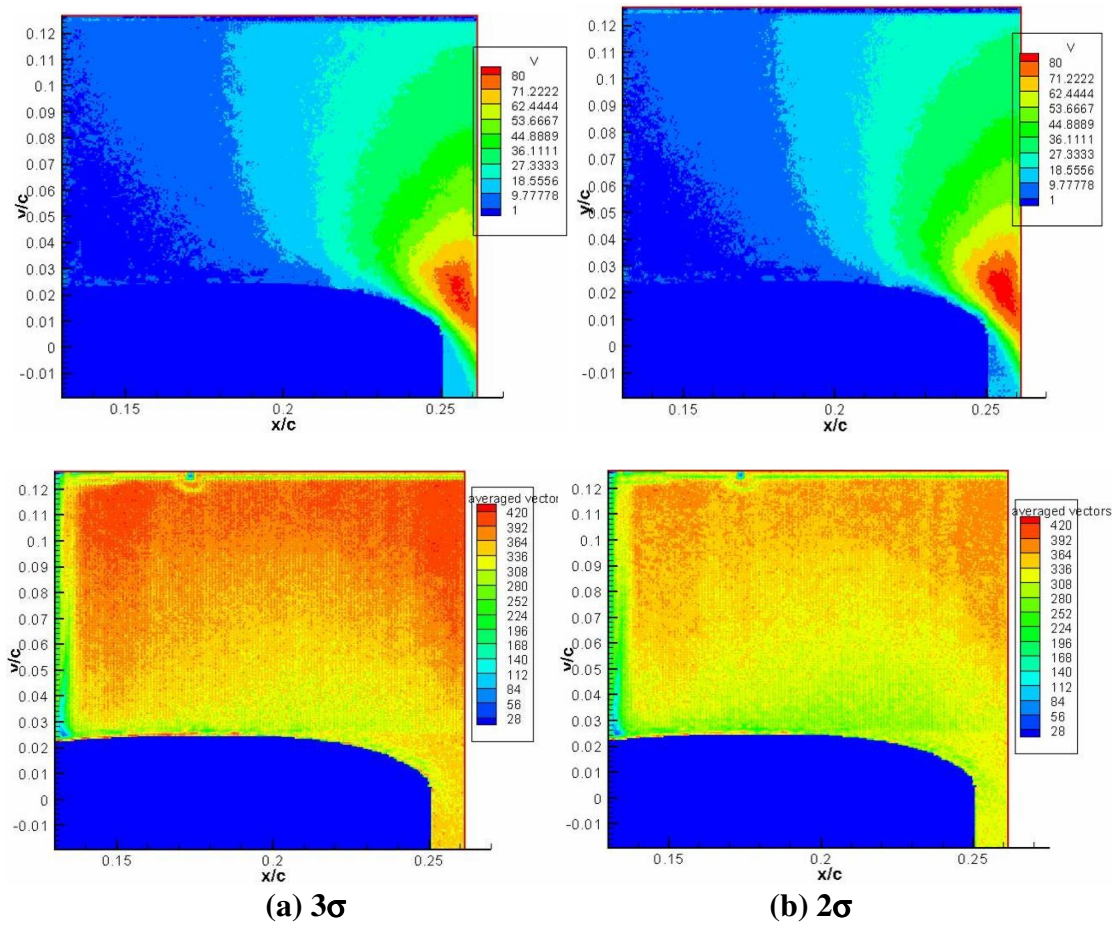
(a) 3σ   **(b) 2σ**
Figure 5.10 Post-processing filter refinement study

Hi-resolution Cooke CCD Camera

P(x,z)

Shear
Deformation
(D_x, D_z)

Contrast
pattern

T(x,z)

Sensitive
Layer

Normal Deform. H(x,z)

S

L

F_x

D_x

h

Model

Elastomer
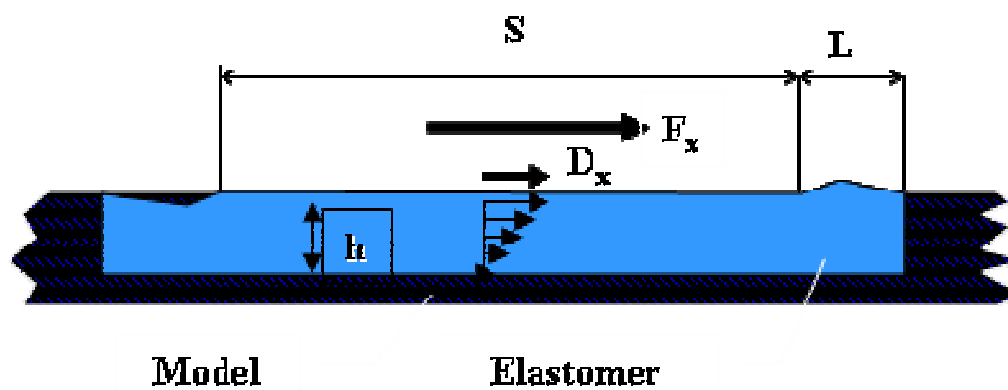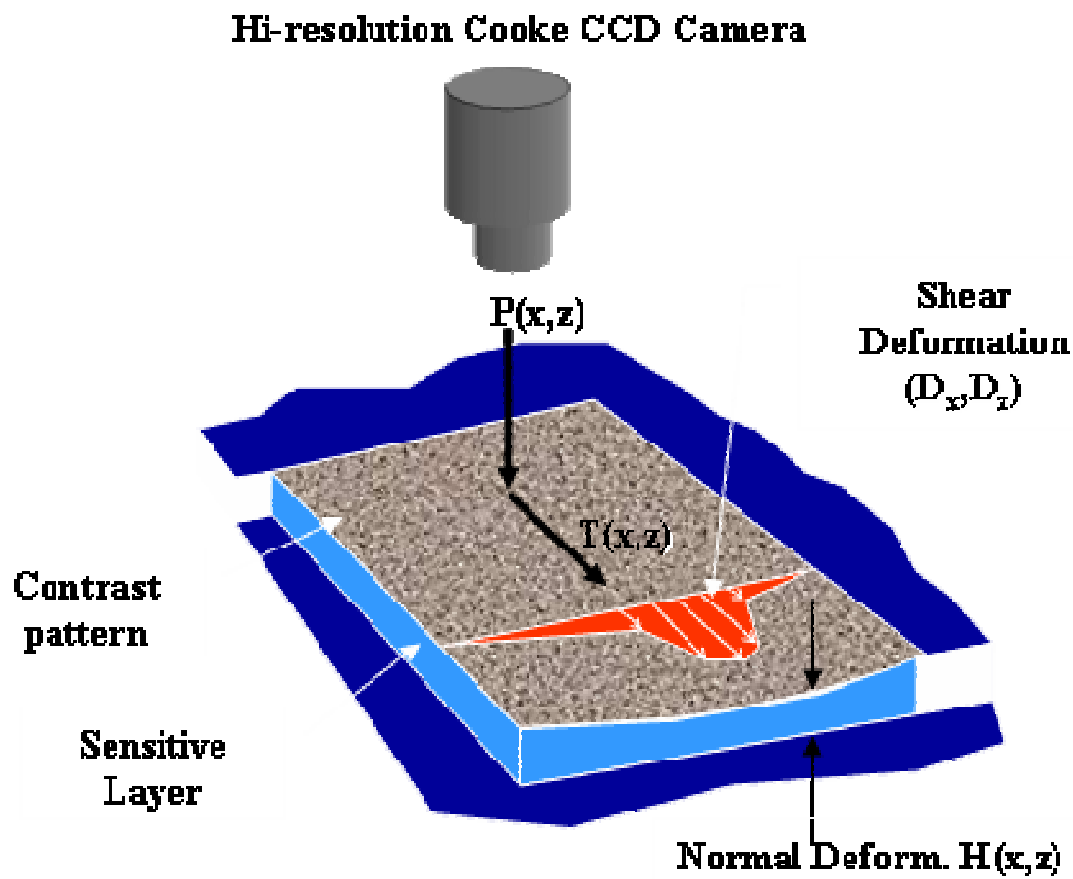
(a) Basic Set-Up for S3F

Shear and Pressure Sensitive Film (S3F)
• **0.5 or 1.0 mm thick**
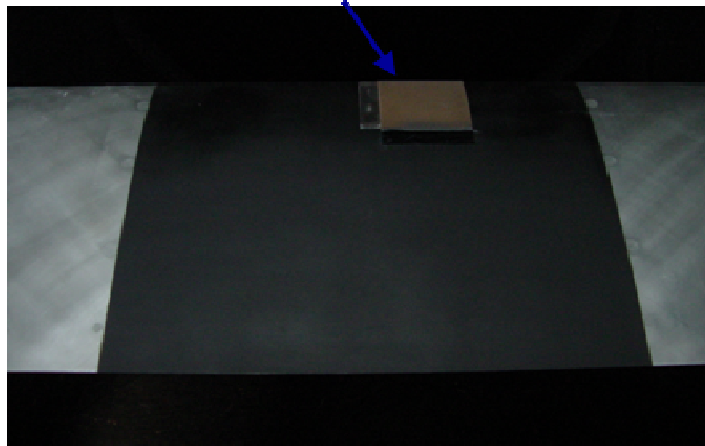
S3F During Testing
• **LED Illumination**
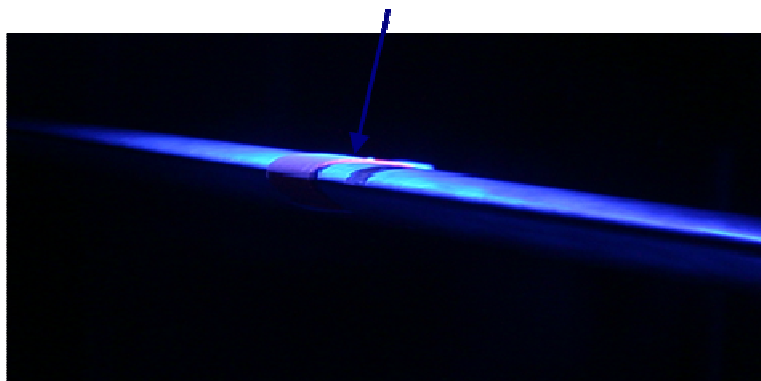
S3F After Testing
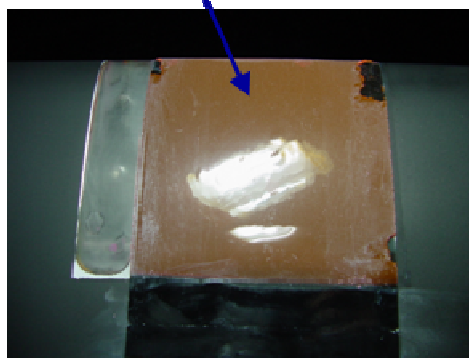
(b) Photographs of the S3F from the present studey
Figure 5.11 ISSI Brand S3F Set-Up

Static   **Flapping**

Normal Displacement Field

Normal Displacement Field

Flow Component of Displacement Field

Flow Component of Displacement Field
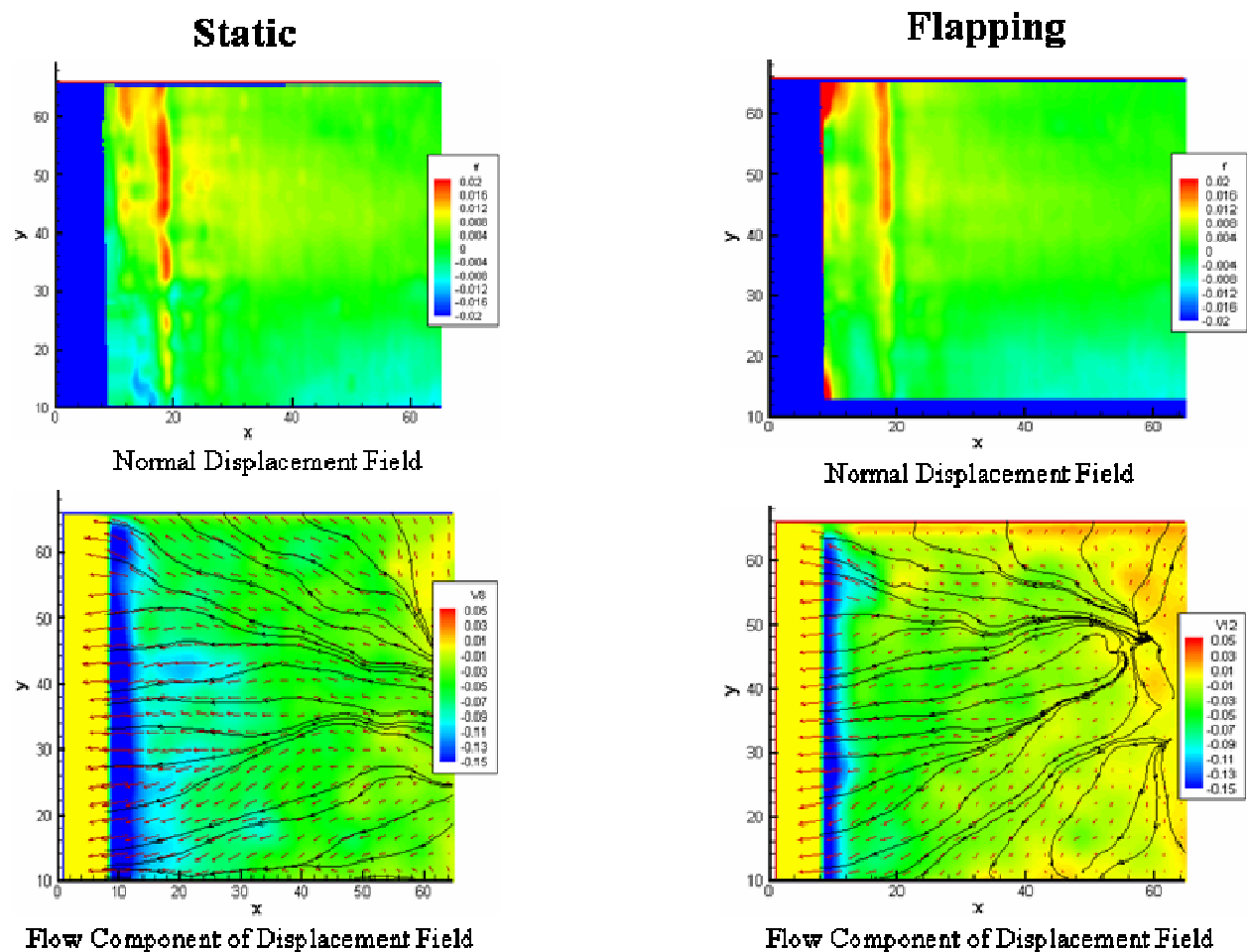
Figure 5.12 Example S3F Case 4 (M = 0.2, k = 0.18, Δα = 5 deg)
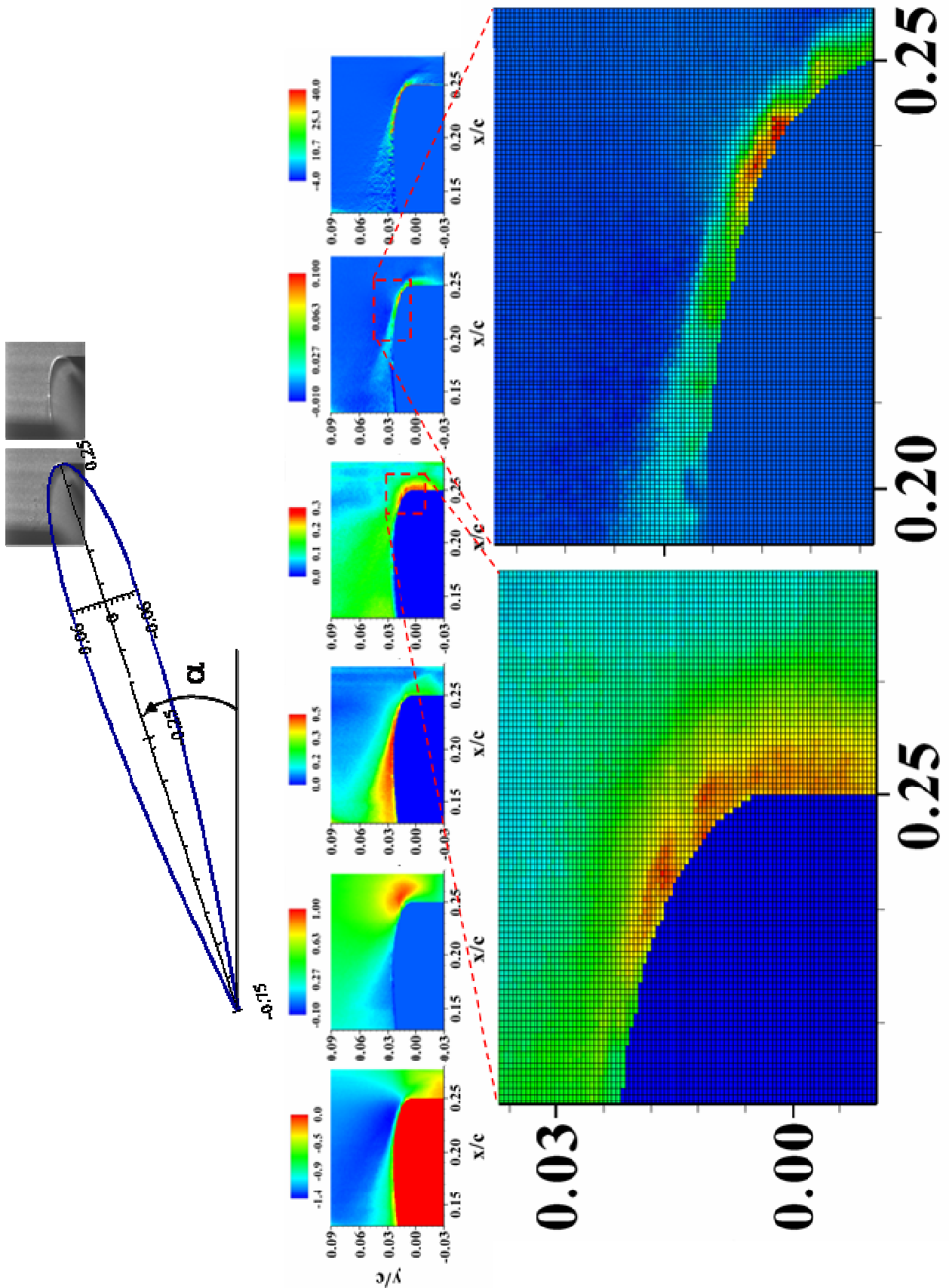
Figure 6.1 Example data (α = 18 deg) for Case 1 (M = 0.2, k = 0.1, $\Delta\alpha$ = 10 deg)
(The smaller images, from left-to-right, correspond to U/U_∞, V/U_∞, σ_u, σ_v, τ_{xy}^T, and P_{xx})
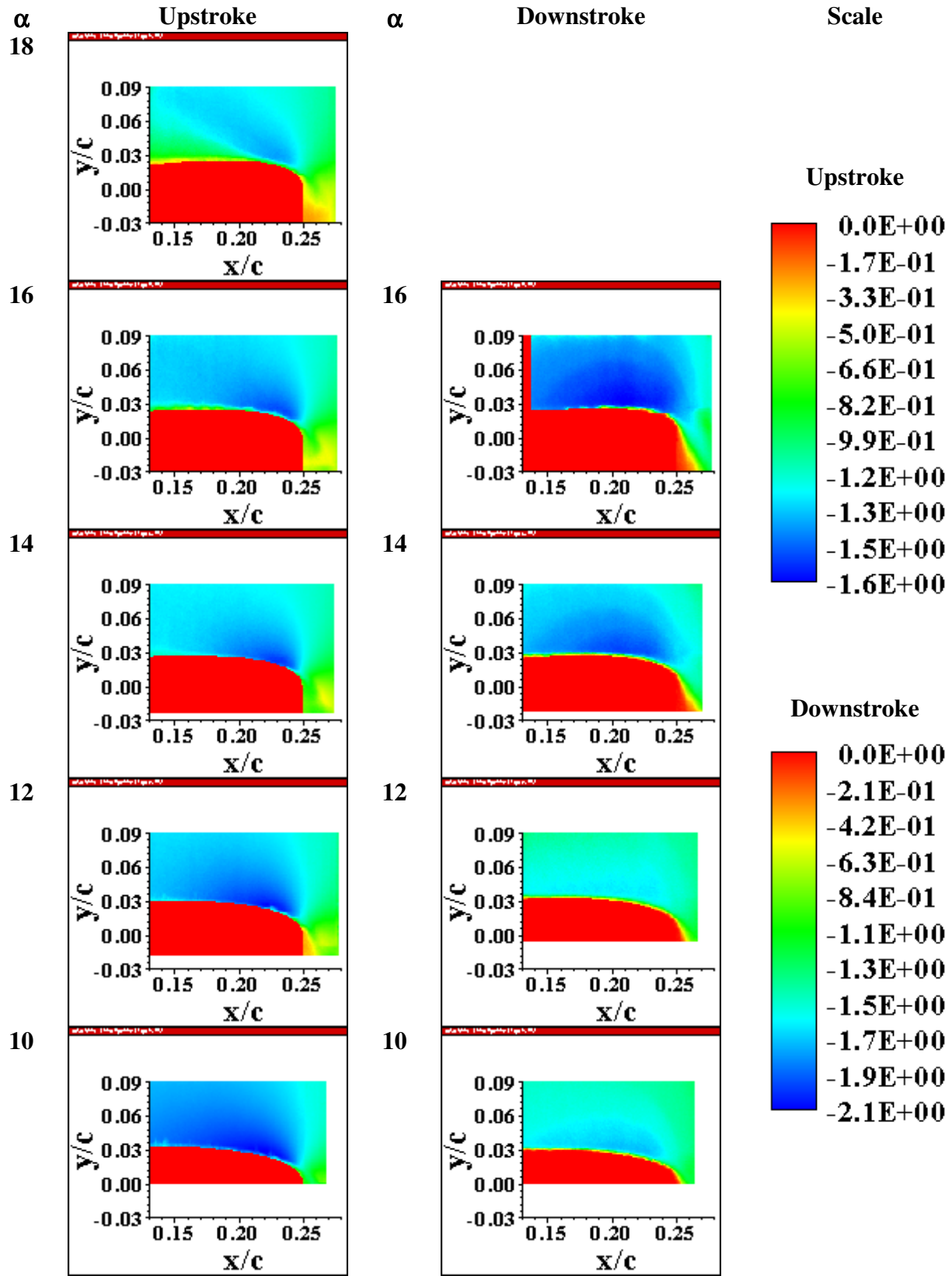
Figure 6.2 U/U$_\infty$, Case 1 (M = 0.2, k = 0.1, Δα = 10 deg)

116
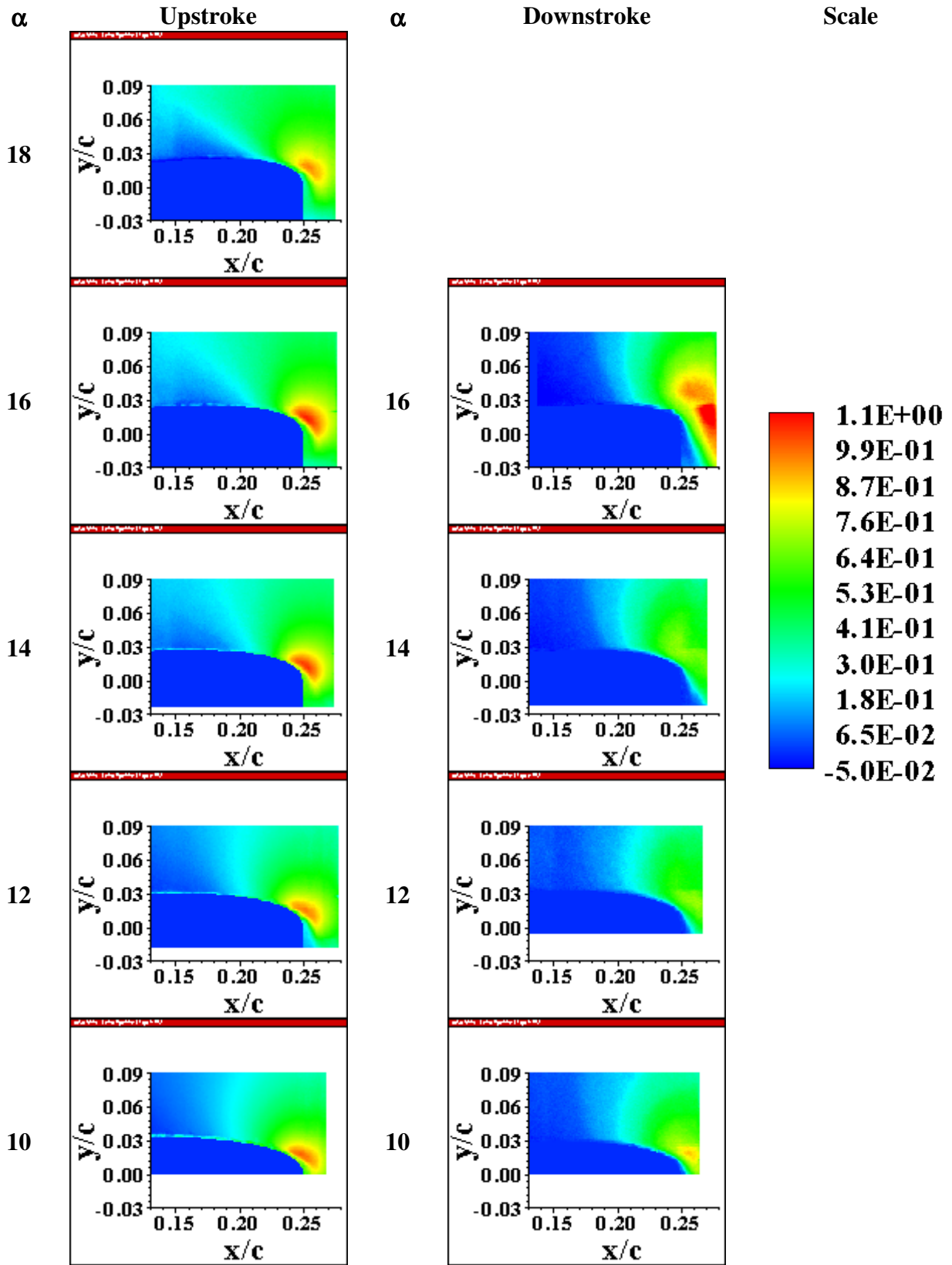
Figure 6.3 V/ U$_\infty$, Case 1 (M = 0.2, k = 0.1, $\Delta\alpha$ = 10 deg)
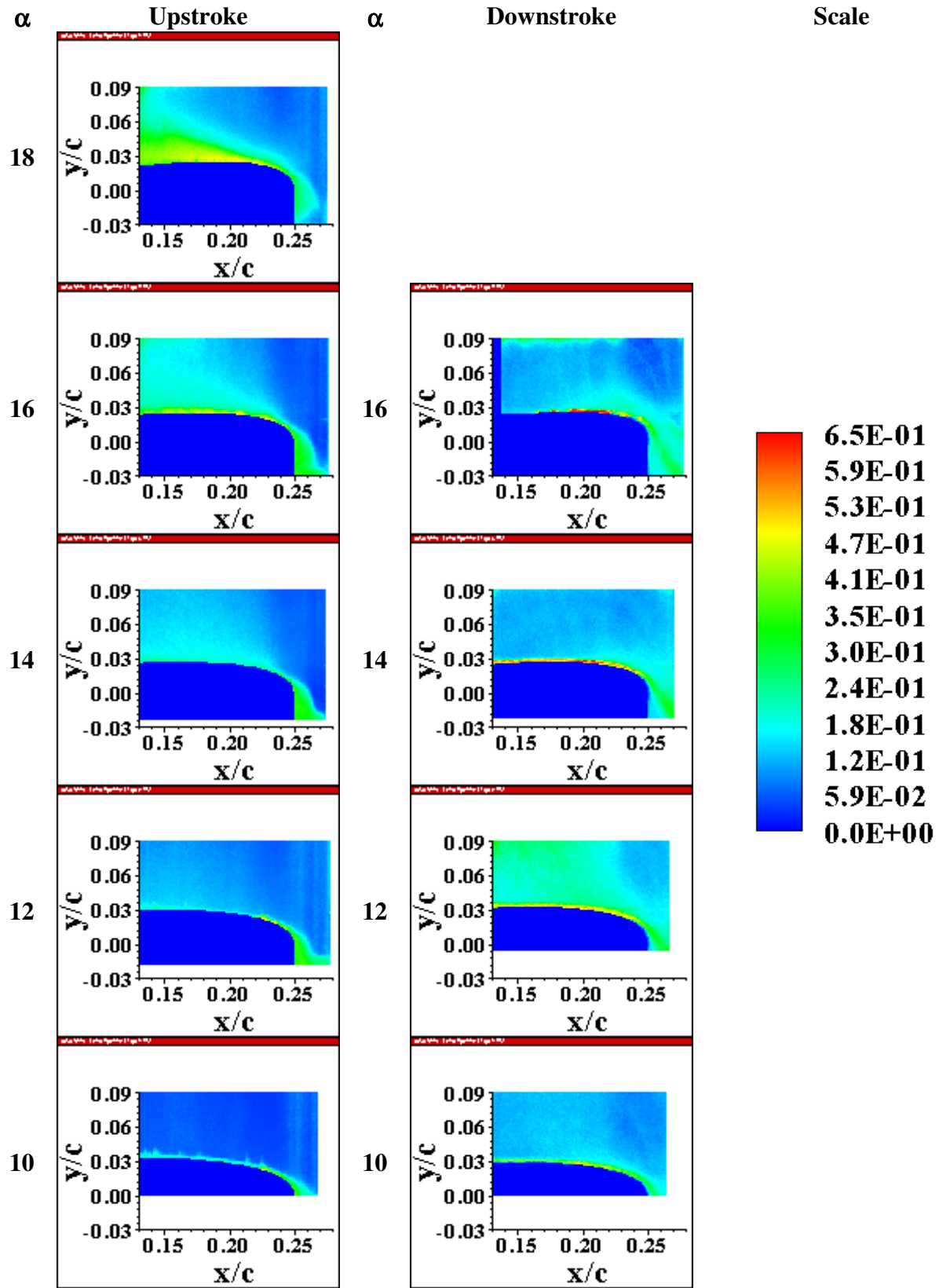
Figure 6.4 σ_u, Case 1 (M = 0.2, k = 0.1, $\Delta\alpha$ = 10 deg)
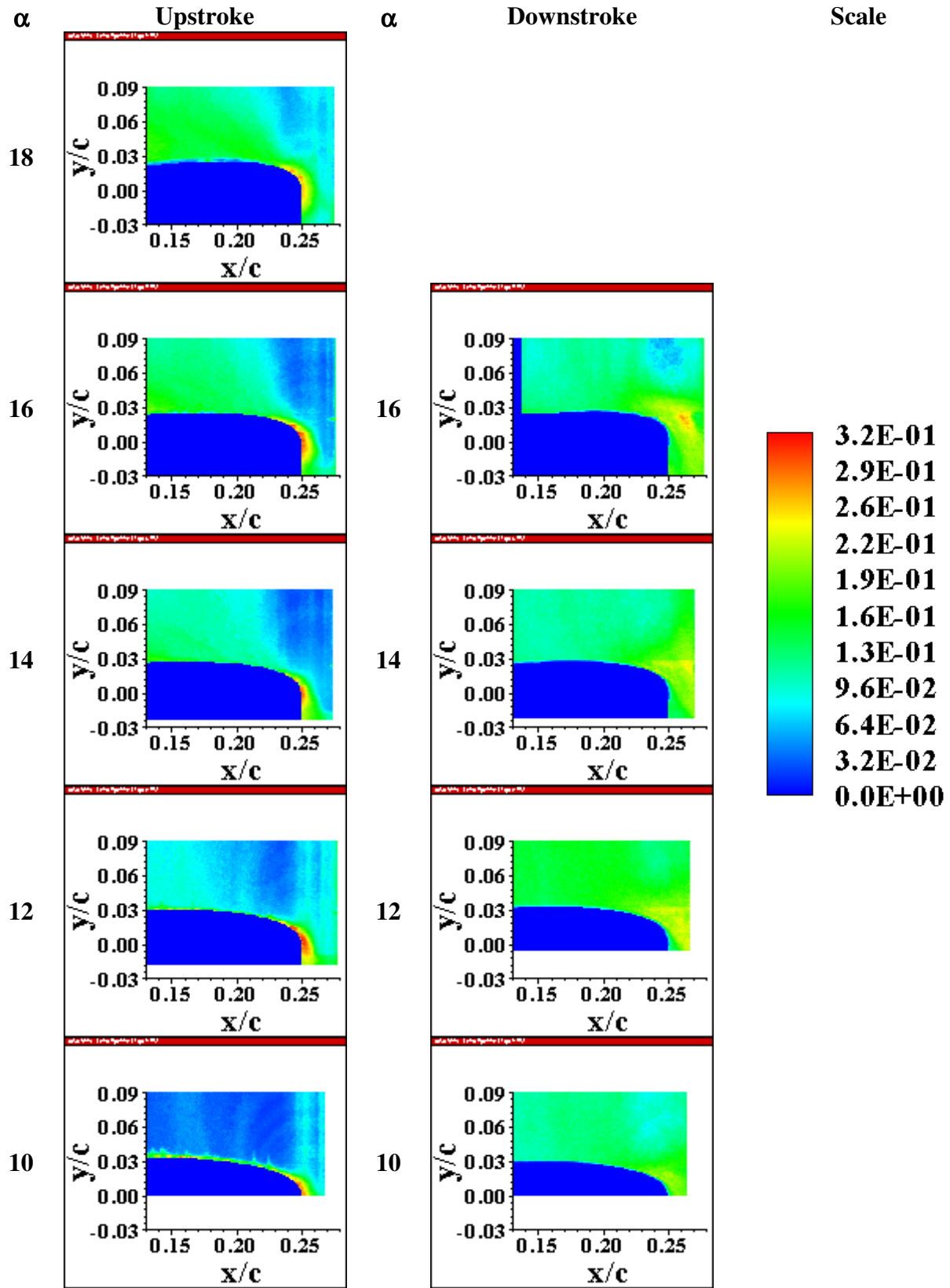
Figure 6.5 σ_v, Case 1 (M = 0.2, k = 0.1, $\Delta\alpha$ = 10 deg)
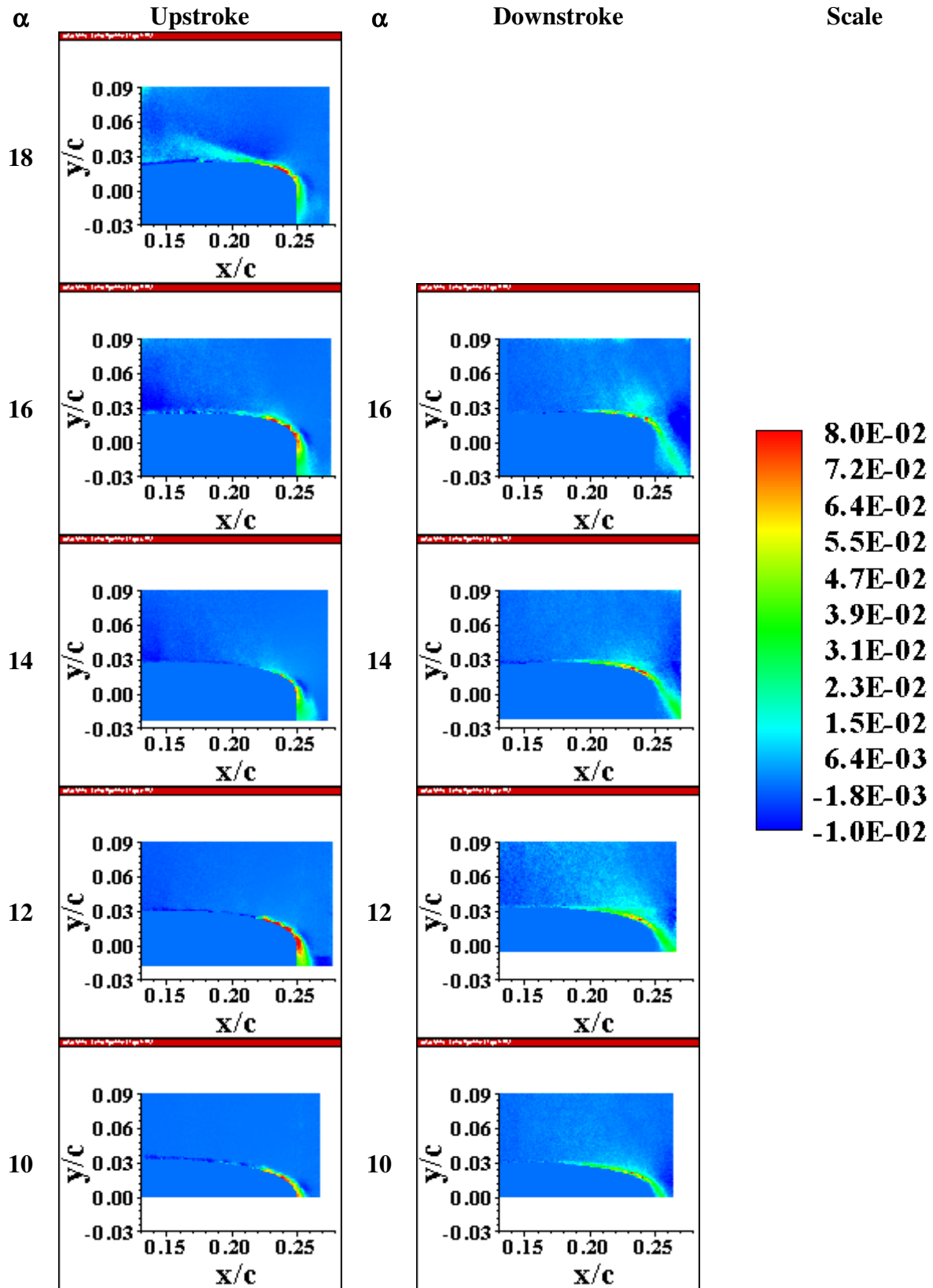
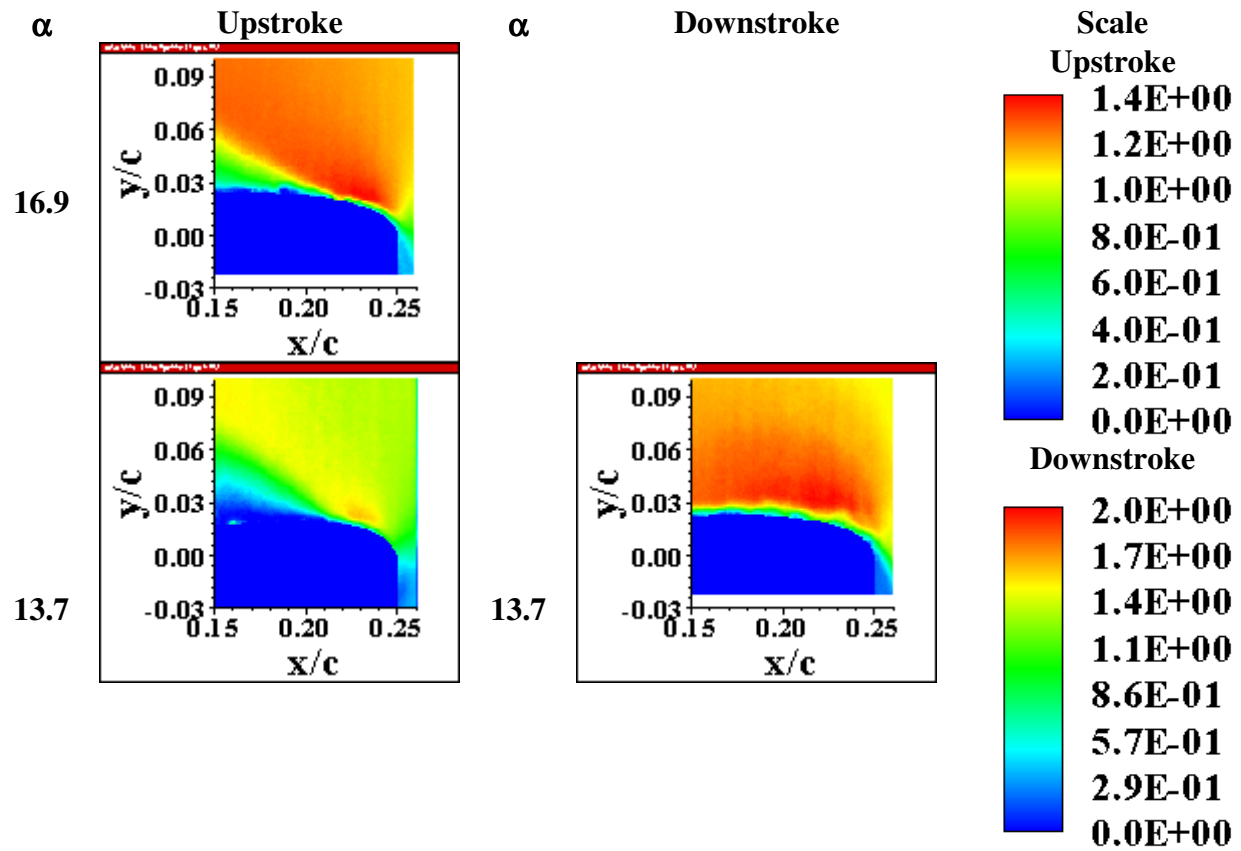**Figure 6.6 Reynolds Stress (τ_{xy}^{T}), Case 1 (M = 0.2, k = 0.1, $\Delta\alpha$ = 10 deg)**
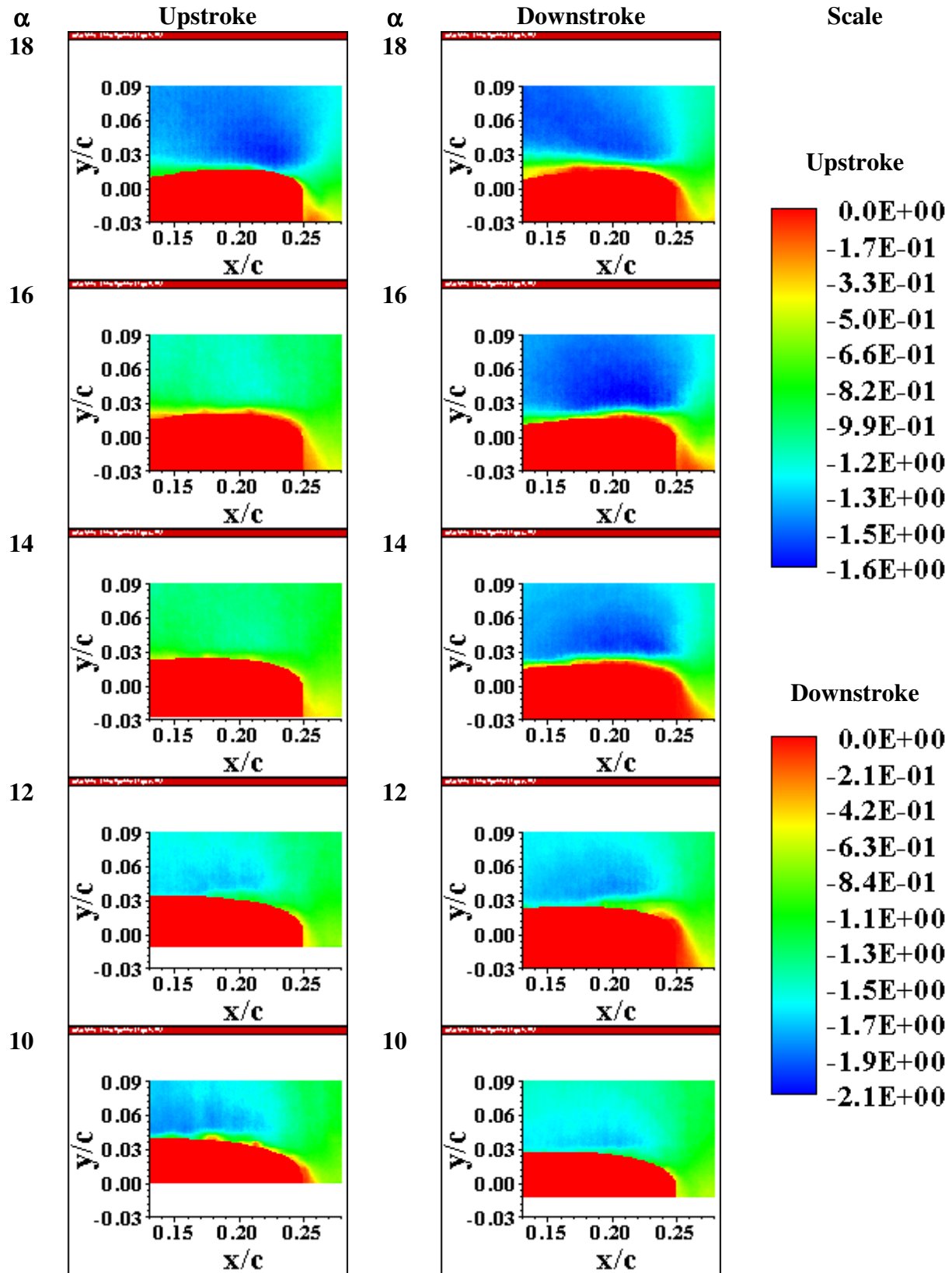
Figure 6.7 U/U$_\infty$, Case 2 (M = 0.28, k = 0.1, Δα = 10 deg)
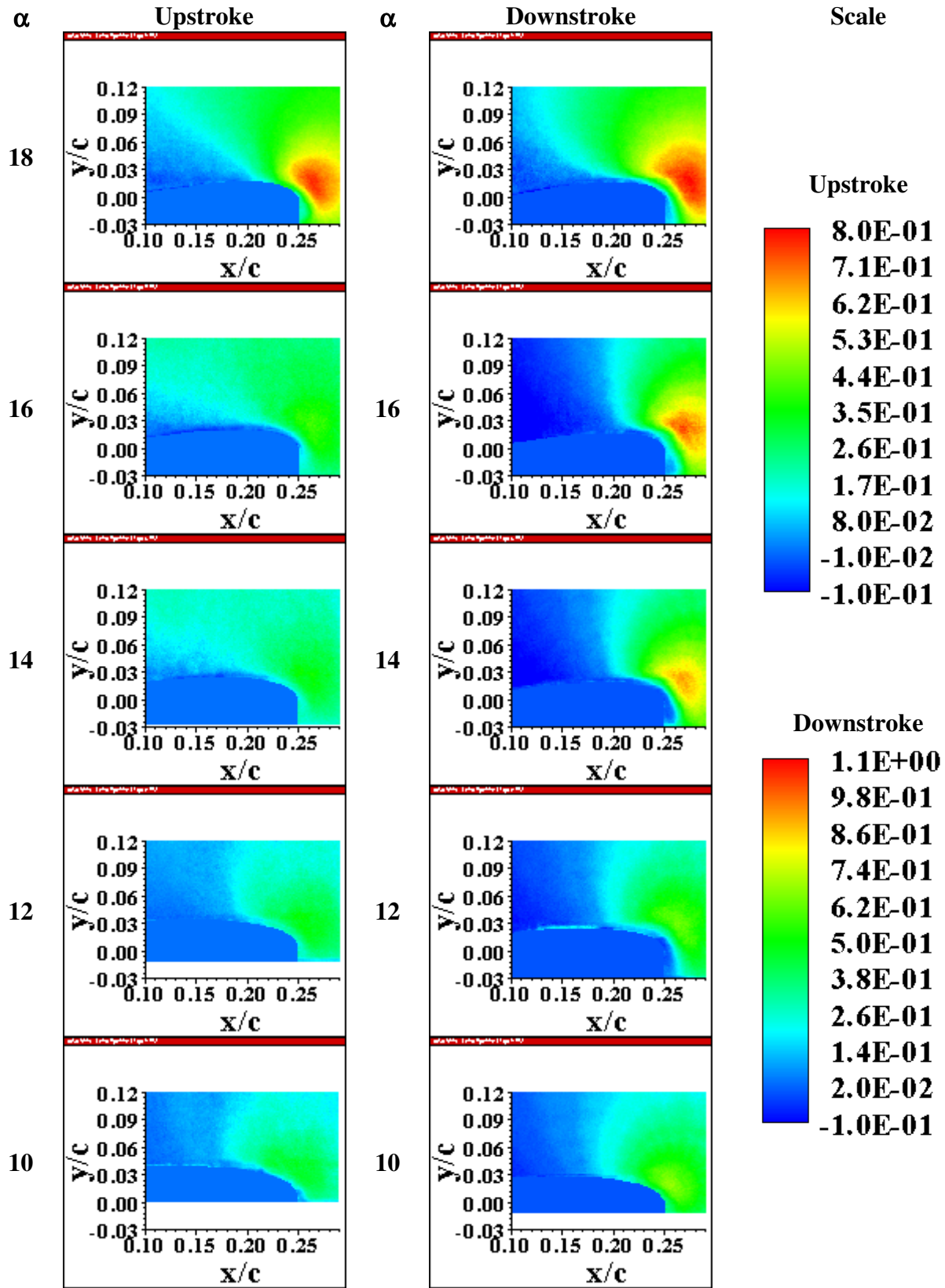
Figure 6.8 V/ U∞, Case 2 (M = 0.28, k = 0.1, Δα = 10 deg)

Figure 6.9 σ_u, Case 2 (M = 0.28, k = 0.1, $\Delta\alpha$ = 10 deg)
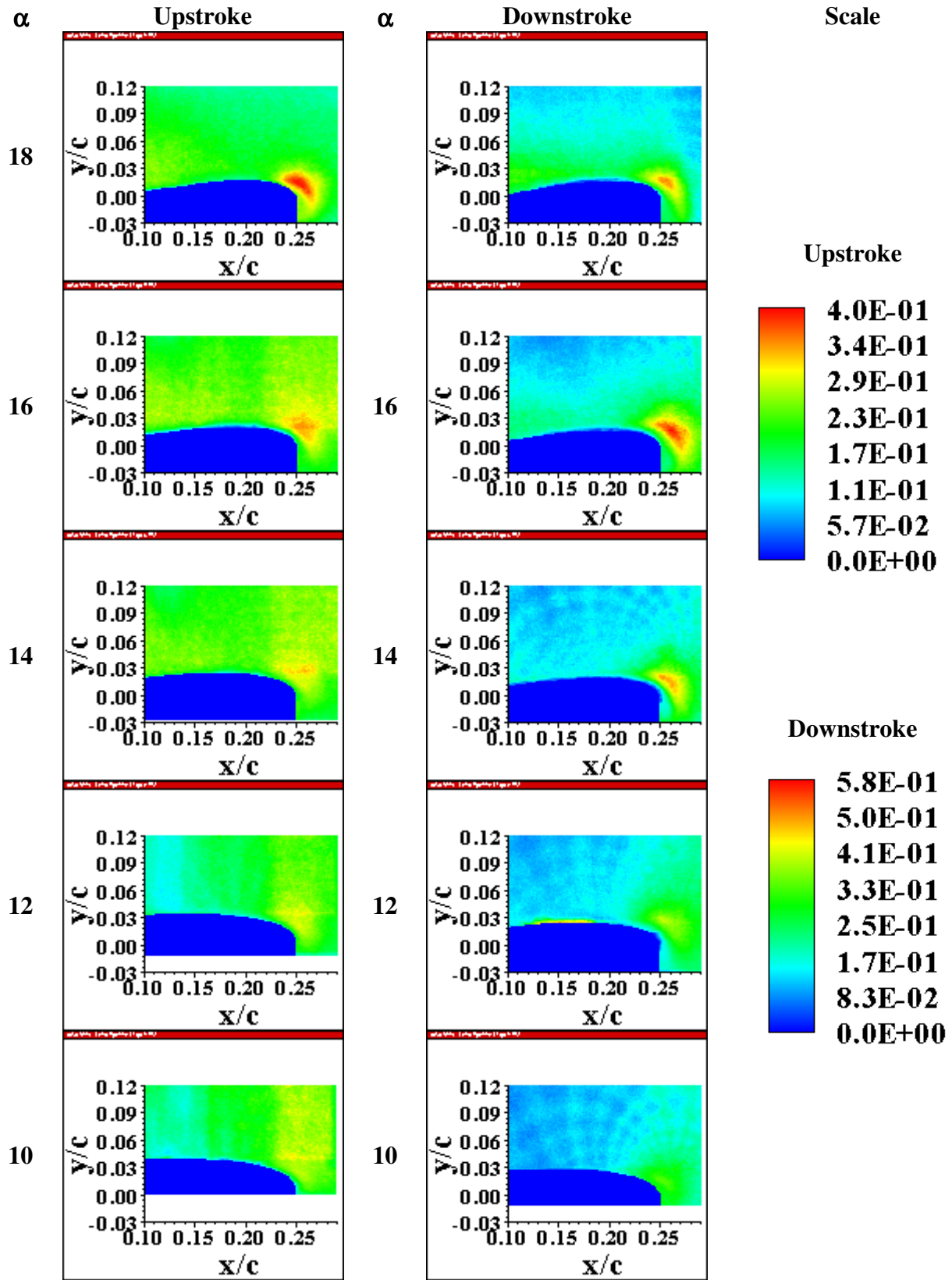
Figure 6.10 σ_v, Case 2 (M = 0.28, k = 0.1, $\Delta\alpha$ = 10 deg)
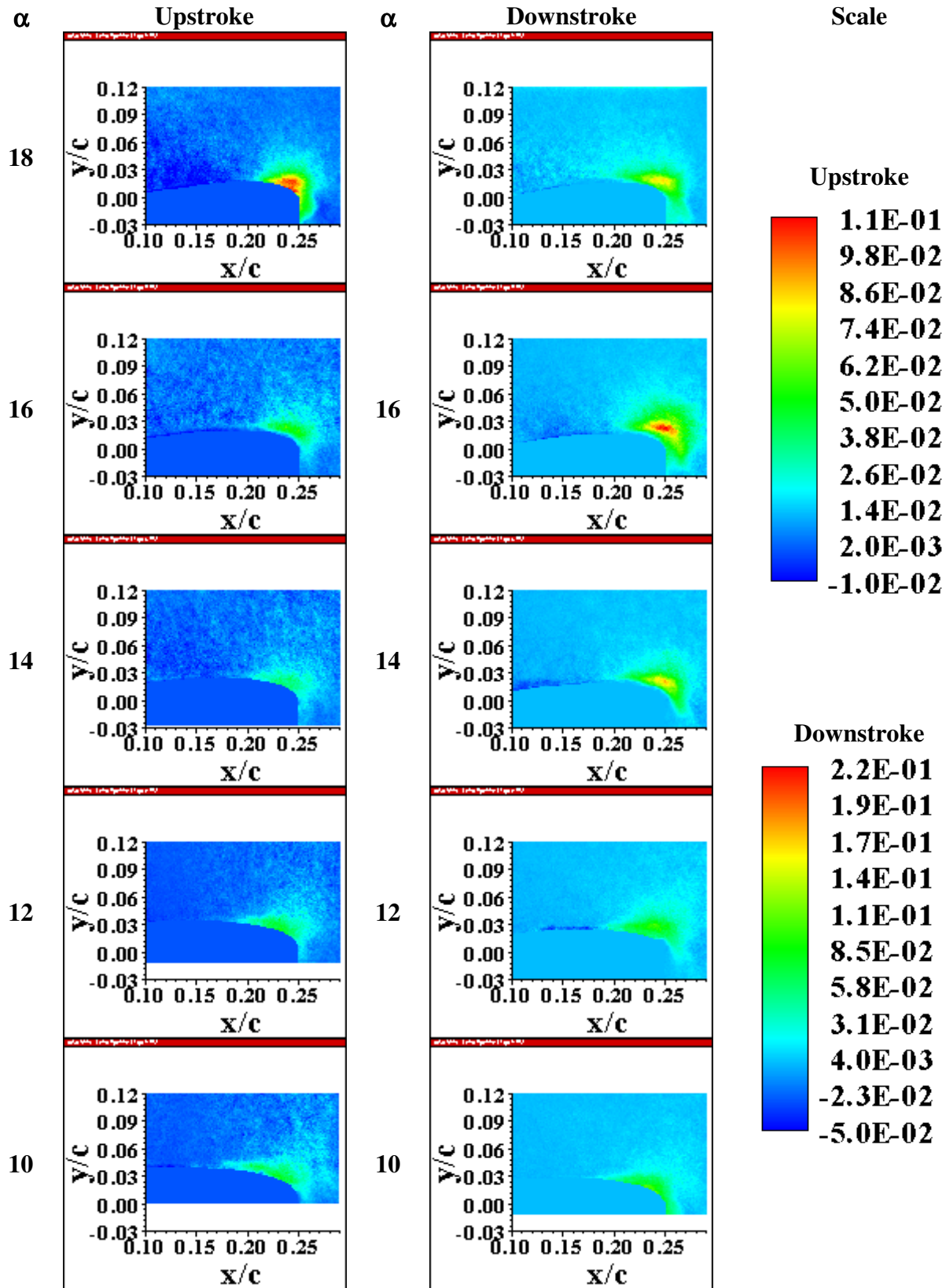
Figure 6.11 Reynolds Stress (τ_{xy}^T), Case 2 (M = 0.28, k = 0.1, $\Delta\alpha$ = 10 deg)
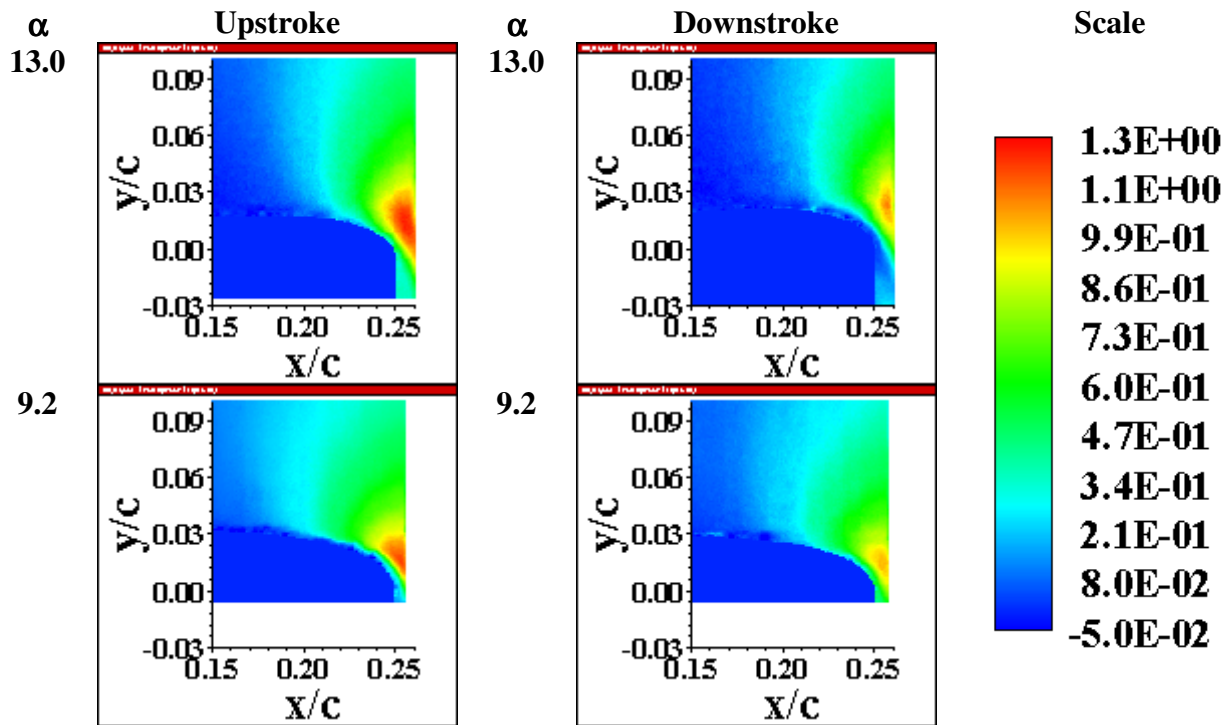
Figure 6.12 V/ U$_\infty$, Case 3 (M = 0.2, k = 0.18, $\Delta\alpha$ = 5 deg)
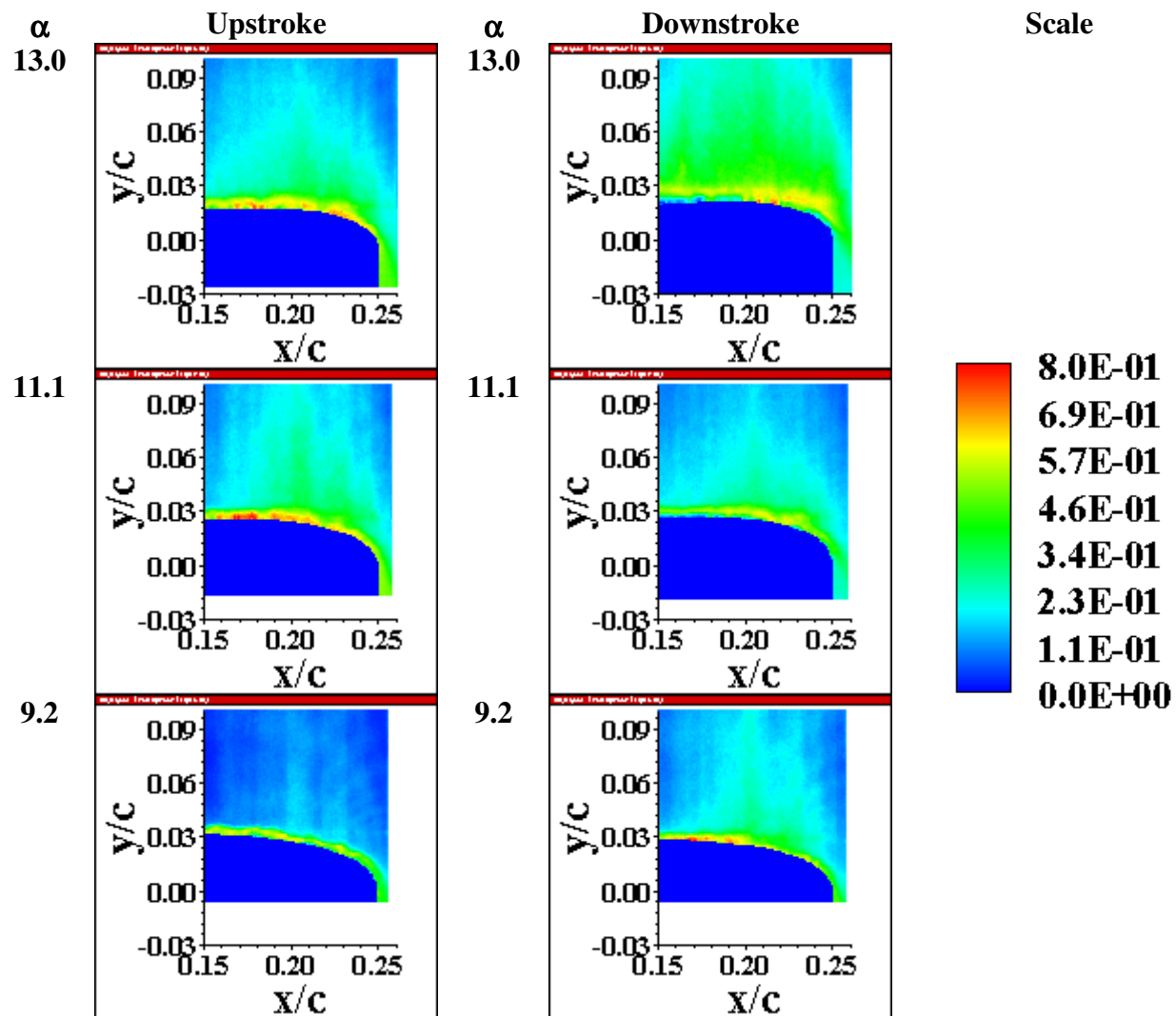
Figure 6.13 σ_u, Case 3 (M = 0.2, k = 0.18, $\Delta\alpha$ = 5 deg)
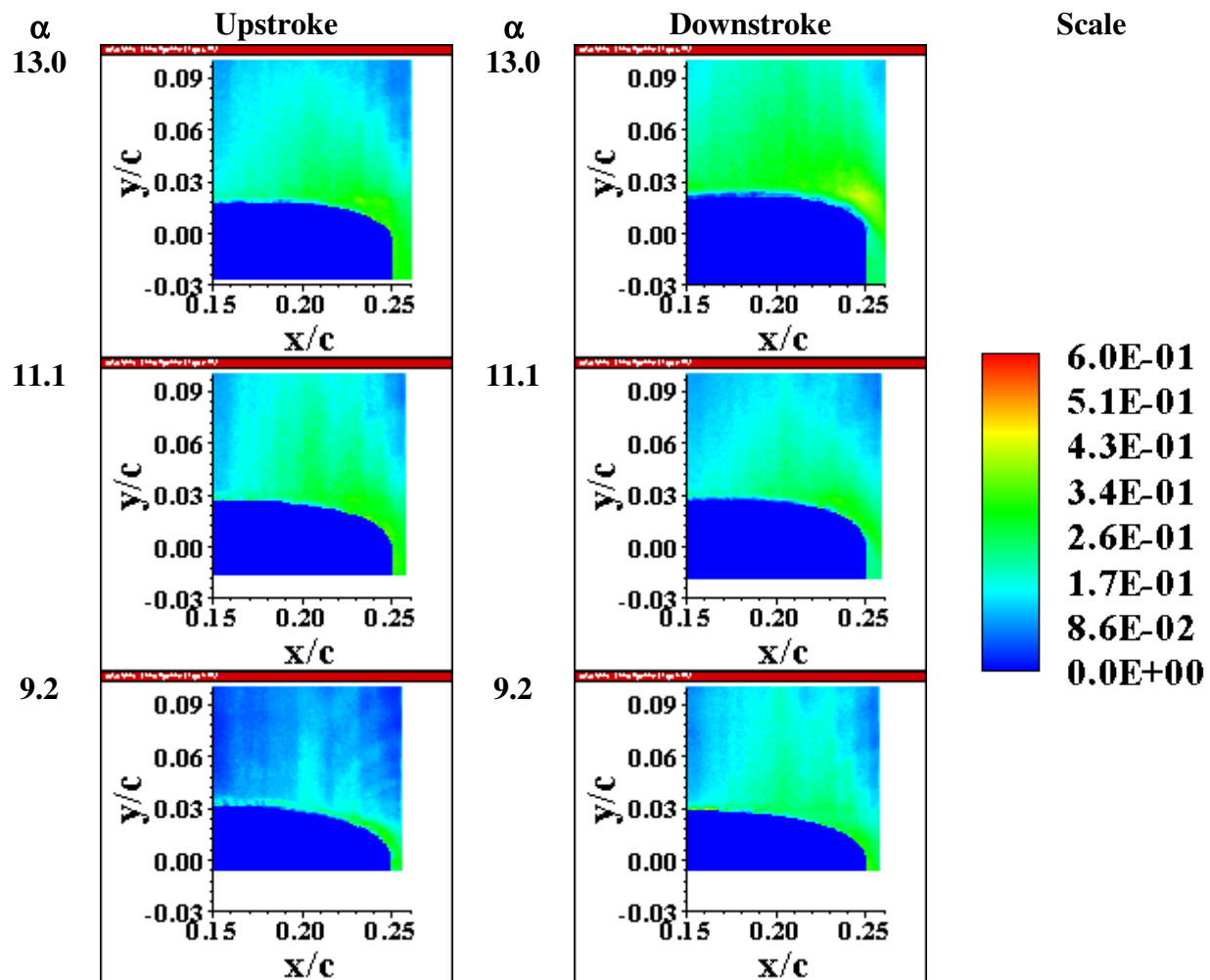
Figure 6.14 σ_v, Case 3 (M = 0.2, k = 0.18, $\Delta\alpha$ = 5 deg)
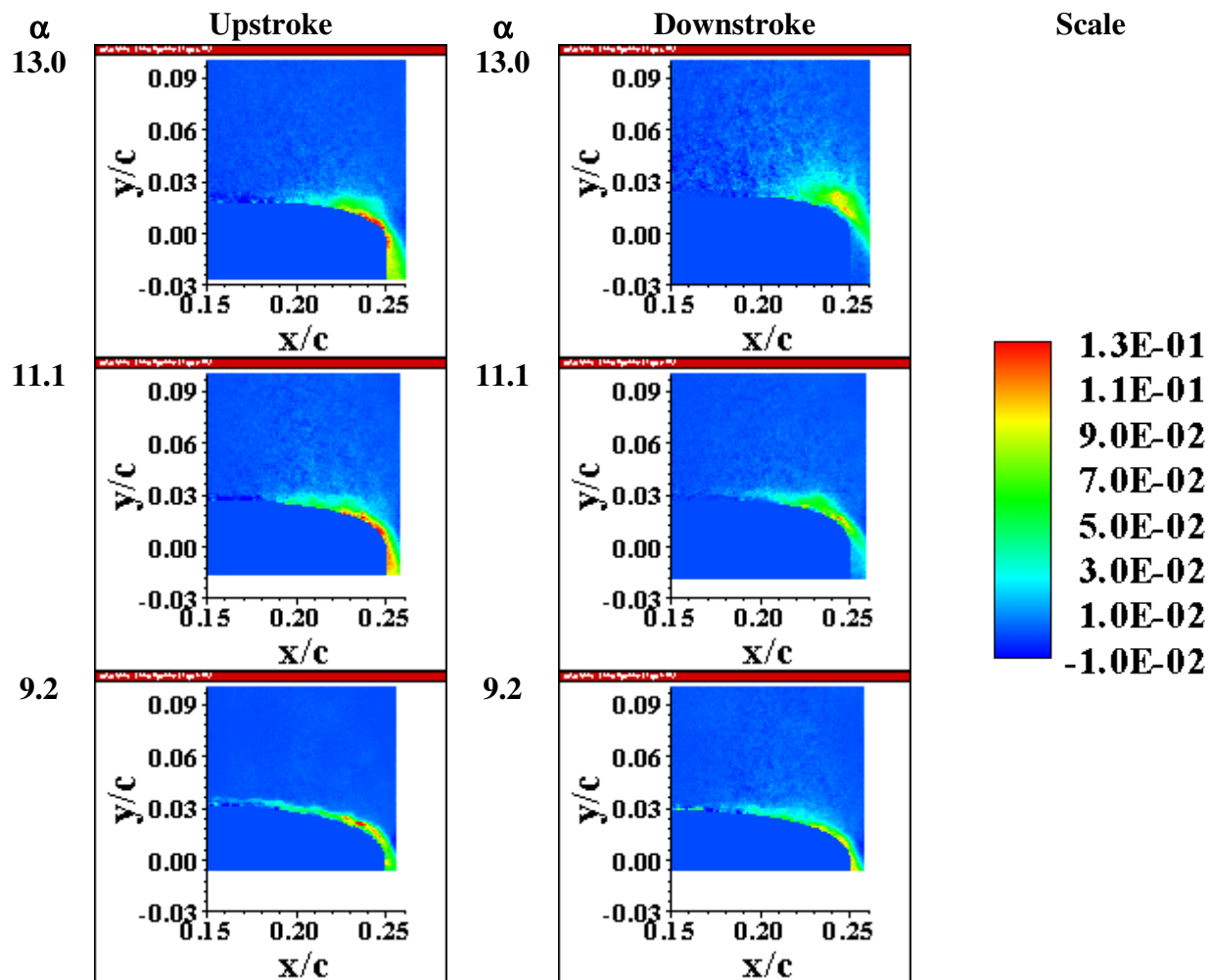
Figure 6.15 Reynolds Stress (τ_{xy}^T), Case 3 (M = 0.2, k = 0.18, $\Delta\alpha$ = 5 deg)

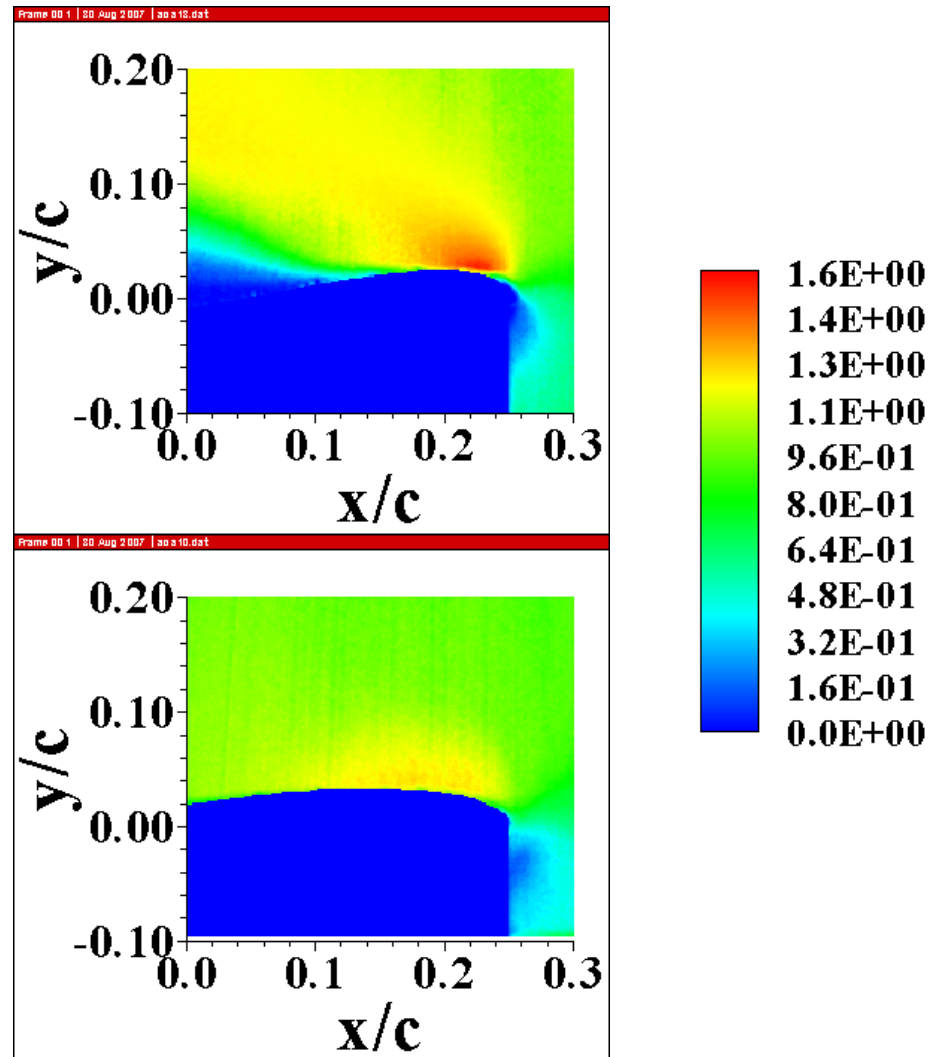α Upstroke α Downstroke Scale

Upstroke

16.9

13.7 13.7

1.4E+00
1.2E+00
1.0E+00
8.0E-01
6.0E-01
4.0E-01
2.0E-01
0.0E+00

Downstroke

2.0E+00
1.7E+00
1.4E+00
1.1E+00
8.6E-01
5.7E-01
2.9E-01
0.0E+00

Figure 6.16 (-U)/U$_\infty$, Case 4 (M = 0.2, k = 0.18, $\Delta\alpha$ = 5 deg)
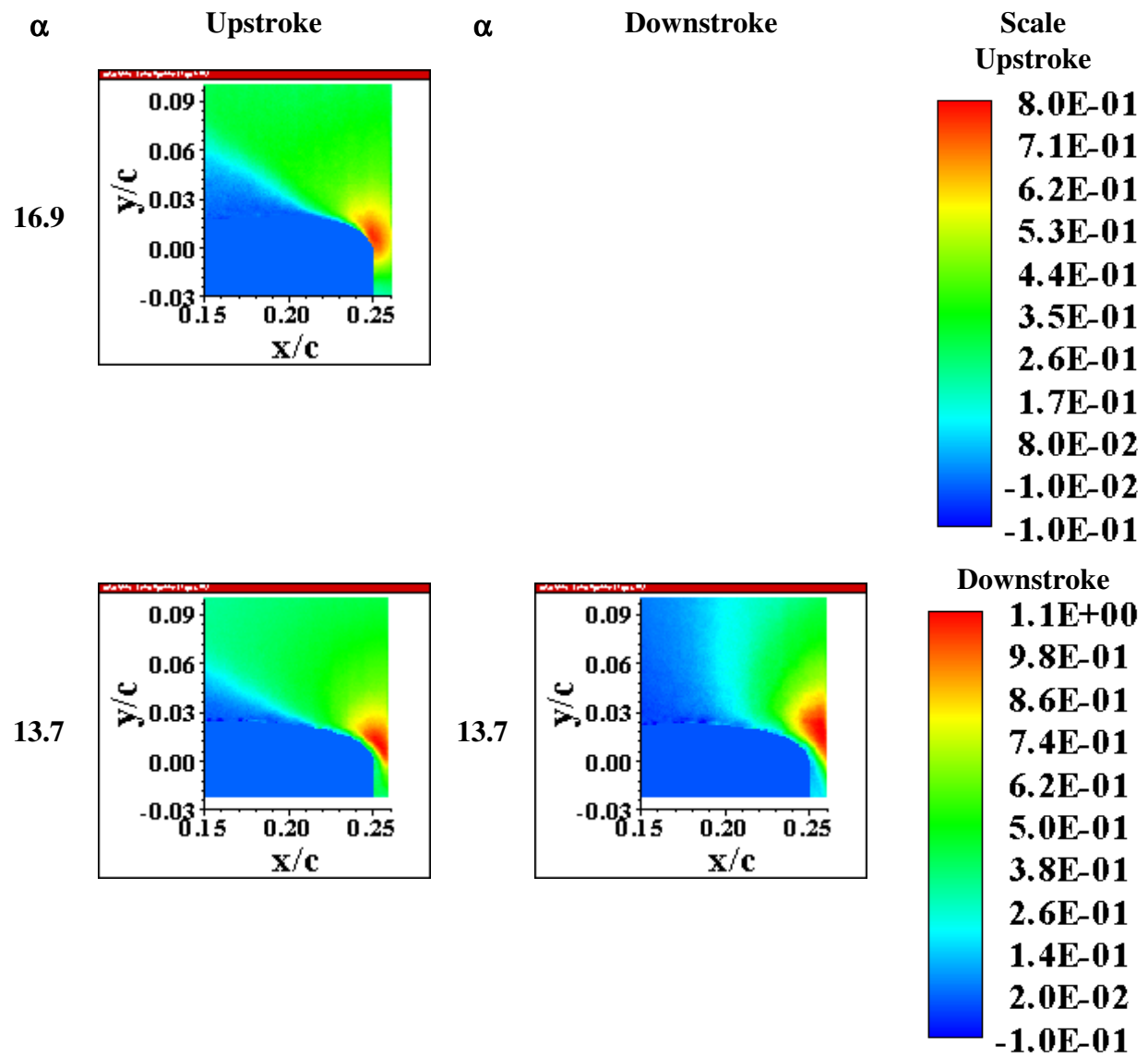
Figure 6.17 V/ U$_\infty$, Case 4 (M = 0.2, k = 0.18, $\Delta\alpha$ = 5 deg)

Figure 6.18 σ_u, Case 4 (M = 0.2, k = 0.18, $\Delta\alpha$ = 5 deg)
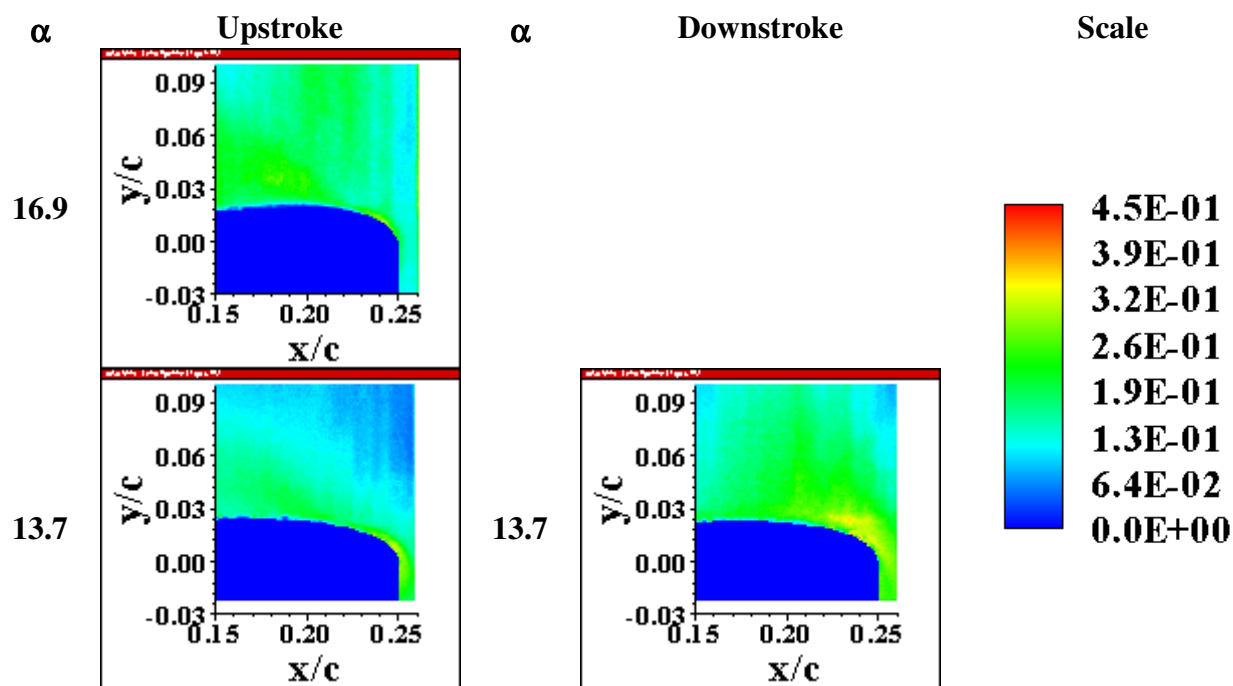
Figure 6.19 σ_v, Case 4 (M = 0.2, k = 0.18, $\Delta\alpha$ = 5 deg)
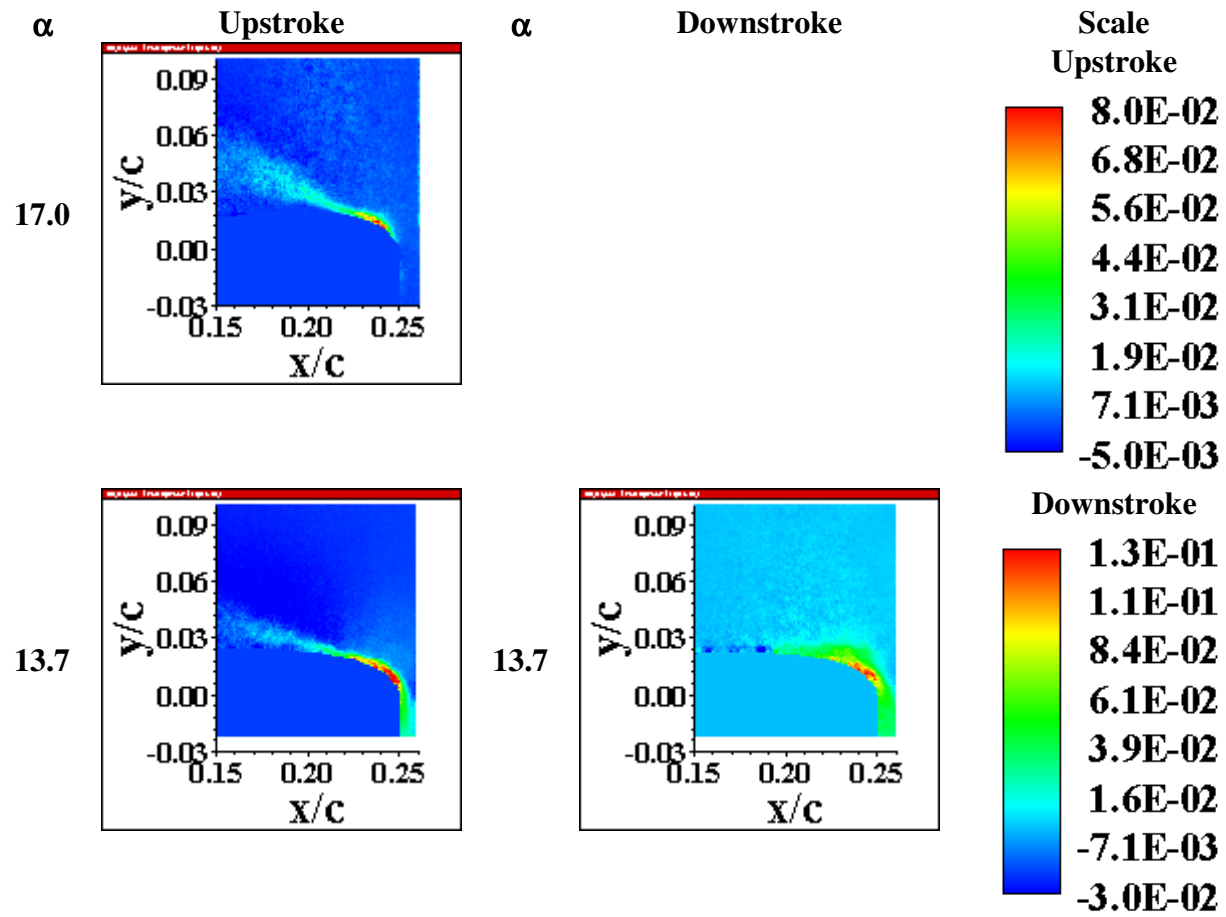
Figure 6.20 Reynolds Stress (τ_{xy}^T), Case 4 (M = 0.2, k = 0.18, $\Delta\alpha$ = 5 deg)
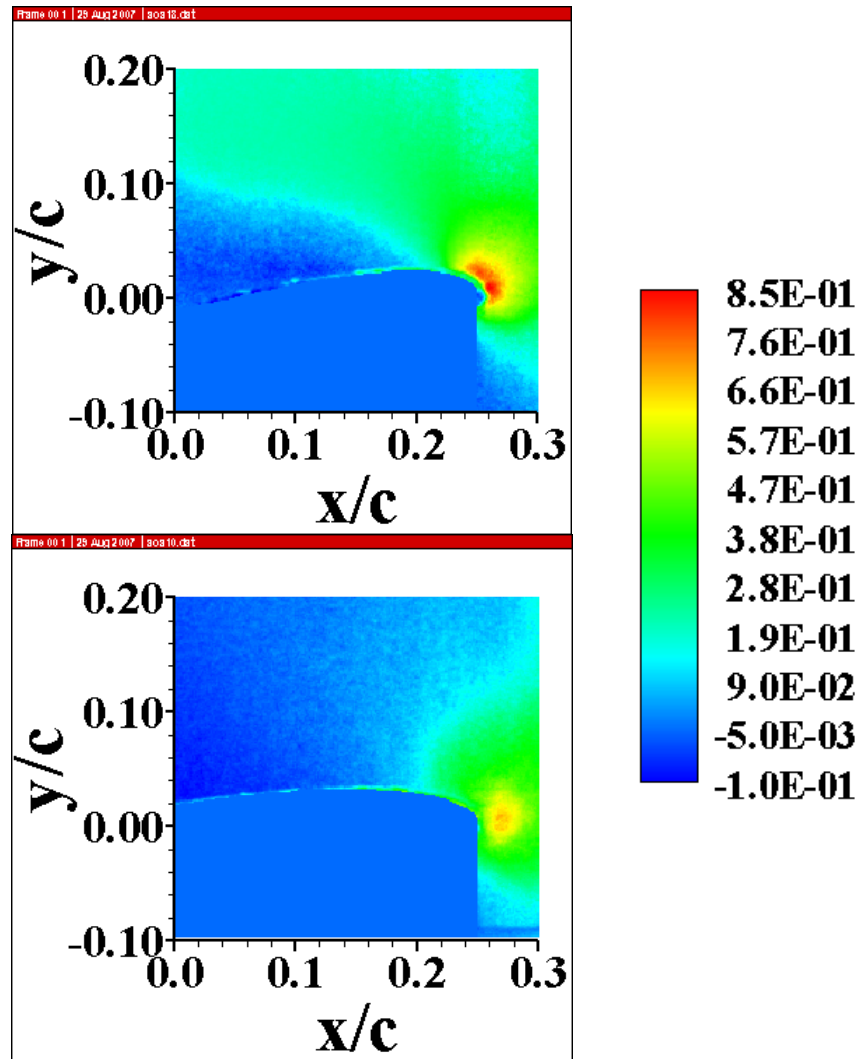
Figure 6.21 U/U∞, Case 5 (M = 0.2, Static)

Figure 6.22 V/ U$_\infty$, Case 5 (M = 0.2, Static)
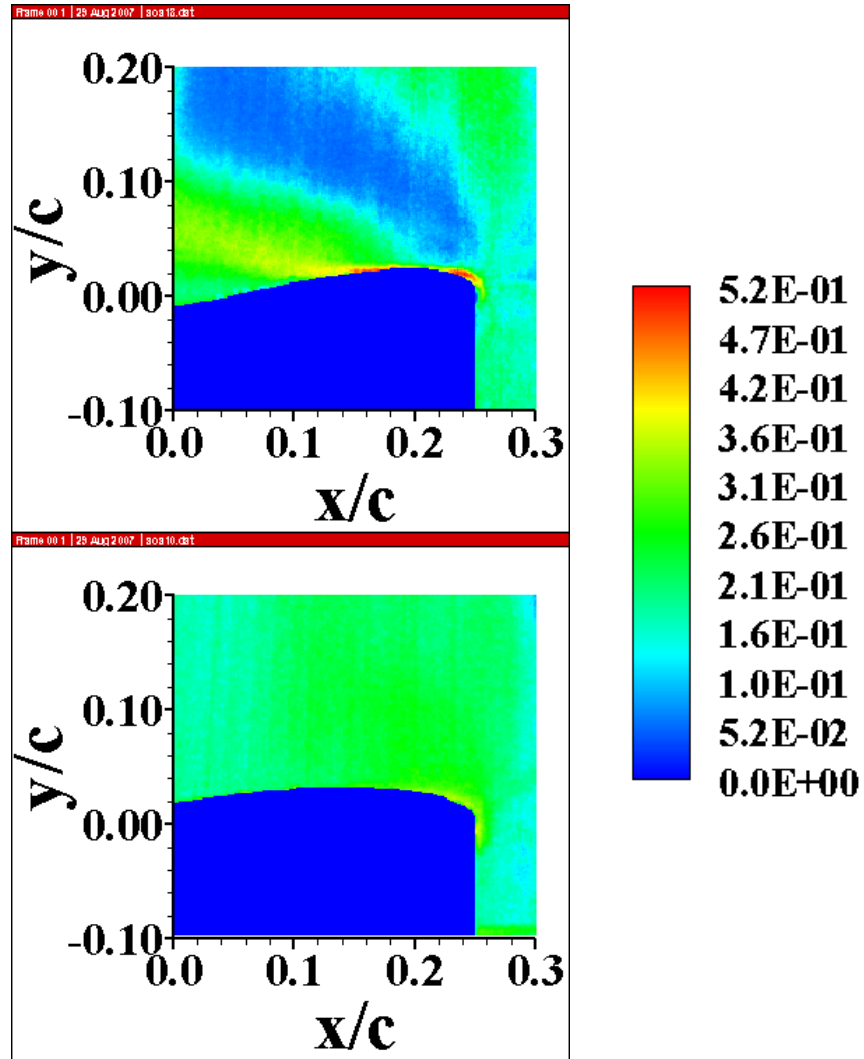
Figure 6.23 σ_u, Case 5 (M = 0.2, Static)
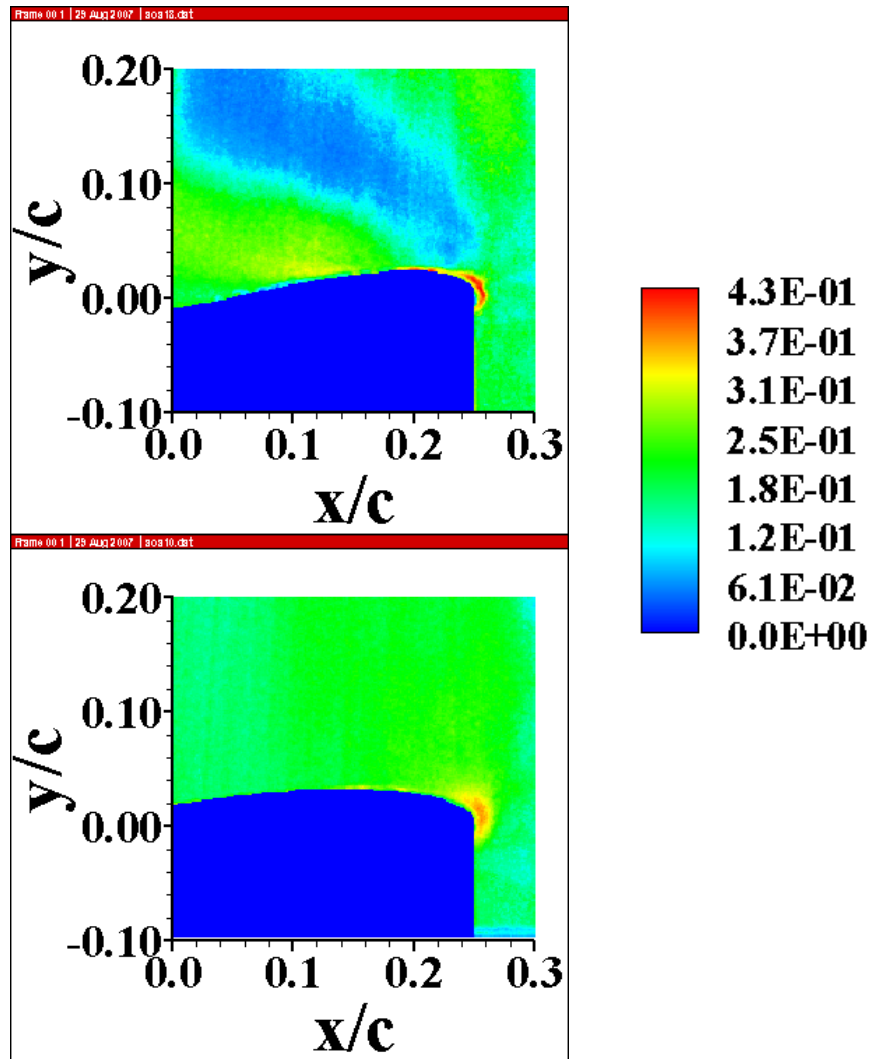
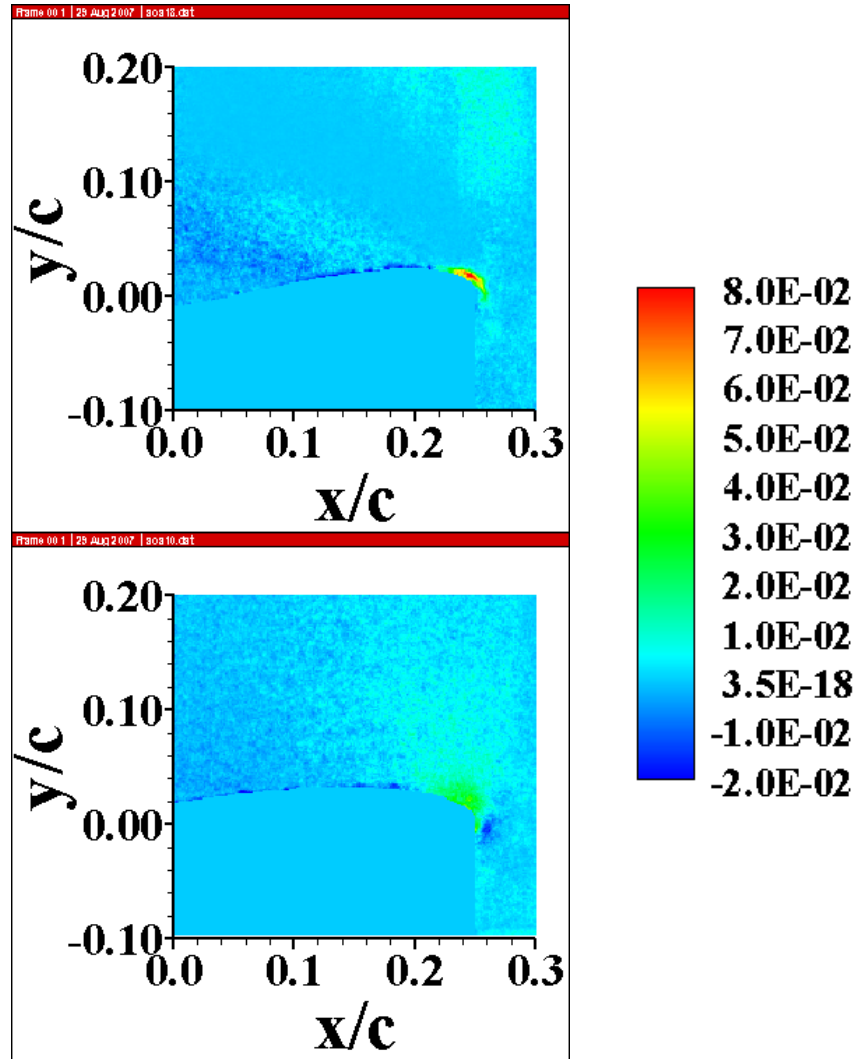**Figure 6.24** σ_v, Case 5 (M = 0.2, Static)

Figure 6.25 Reynolds Stress (τ_{xy}^T), Case 5 (M = 0.2, Static)